LQG/LTR, H-INFINITY AND MU ROBUST CONTROLLERS DESIGN FOR LINE OF SIGHT STABILIZATION

A THESIS SUBMITTED TO
THE GRADUATE SCHOOL OF NATURAL AND APPLIED SCIENCES
OF
MIDDLE EAST TECHNICAL UNIVERSITY

BY

MEHMET BASKIN

IN PARTIAL FULFILLMENT OF THE REQUIREMENTS
FOR
THE DEGREE OF MASTER OF SCIENCE
IN
ELECTRICAL AND ELECTRONICS ENGINEERING

DECEMBER 2015

Approval of the thesis:

LQG/LTR, H-INFINITY AND MU ROBUST CONTROLLERS DESIGN FOR LINE OF SIGHT STABILIZATION

submitted by **MEHMET BASKIN** in partial fulfillment of the requirements for the degree of **Master of Science in Electrical and Electronics Engineering Department, Middle East Technical University** by,

Prof. Dr. Gülbin Dural Ünver _____
Dean, Graduate School of **Natural and Applied Sciences**

Prof. Dr. Gönül Turhan Sayan _____
Head of Department, **Electrical and Electronics Engineering**

Prof. Dr. Kemal Leblebicioğlu _____
Supervisor, **Electrical and Electronics Engineering Dept., METU**

Examining Committee Members:

Prof. Dr. Mübeccel Demirekler _____
Electrical and Electronics Engineering Dept., METU

Prof. Dr. Kemal Leblebicioğlu _____
Electrical and Electronics Engineering Dept., METU

Prof. Dr. Mehmet Önder Efe _____
Computer Engineering Dept., Hacettepe University

Assoc. Prof. Dr. Umut Orguner _____
Electrical and Electronics Engineering Dept., METU

Assist. Prof. Dr. Yakup Özkazanç _____
Electrical and Electronics Eng. Dept., Hacettepe University

Date: 21/12/2015

I hereby declare that all information in this document has been obtained and presented in accordance with academic rules and ethical conduct. I also declare that, as required by these rules and conduct, I have fully cited and referenced all material and results that are not original to this work.

Name, Last Name : Mehmet BASKIN

Signature : _____

ABSTRACT

LQG/LTR, H-INFINITY AND MU ROBUST CONTROLLERS DESIGN FOR LINE OF SIGHT STABILIZATION

Baskın, Mehmet

M.S., Department of Electrical and Electronics Engineering

Supervisor: Prof. Dr. Kemal Leblebicioğlu

December 2015, 164 pages

Line of sight stabilization against various disturbances is an essential property of gimbaled vision systems mounted on mobile platforms. As the vision systems are designed to function at longer operating ranges with relatively narrow field of views, the expectations from stabilization loops have increased in recent years.

In order to design a good stabilization loop, high gain compensation is required. While satisfying high loop gains for disturbance attenuation, it is also required to satisfy sufficient loop stability. Structural resonances and model uncertainties put strict restrictions on achievable stabilization loop bandwidth for gimbaled vision systems. For that reason, satisfying high stabilization performance under modeling errors requires utilization of robust control methods.

In this thesis, robust controller design in LQG/LTR, H-infinity and Mu frameworks is described for a two-axis gimbal. First, the modeling errors are found by investigating the locally linearized models under different conditions. Next, the performance indices and weights are determined by considering the allowable stabilization error and possible platform disturbance profile. Then generalized plants are obtained by using the nominal model and corresponding weights for three different design methods. Using these generalized plants, LQG/LTR, H-infinity and Mu controllers are synthesized. Stabilities and performances of the three designs are investigated in detail. After that, comparison of the controllers is made by investigating the robustness of corresponding closed loops.

The thesis work is finished with the experimental studies and performances to validate the designed robust controllers.

Keywords: LQG/LTR, H-infinity, Mu-synthesis, robust control, line of sight stabilization

ÖZ

BAKIŞ HATTI STABİLİZASYONU İÇİN LQG/LTR, H-SONSUZ VE MU GÜRBÜZ DENETLEYİCİLERİNİN TASARIMI

Baskın, Mehmet
Yüksek Lisans, Elektrik ve Elektronik Mühendisliği Bölümü
Tez Yöneticisi: Prof. Dr. Kemal Leblebicioğlu
Aralık 2015, 164 sayfa

Bakış hattı stabilizasyonunun çeşitli bozucu etkilere karşı sağlanması hareketli platformlara yerleştirilen gimballi görüntüleme sistemleri için gerekli bir özelliktir. Son yıllarda görüntüleme sistemlerinin daha uzun mesafelerde daha dar bakış açıları ile çalışacak şekilde tasarlanmasıyla stabilizasyon döngülerinden beklentiler artmıştır.

İyi bir stabilizasyon döngüsü tasarlamak için yüksek kazançlı denetleyici gereklidir. Bozucu etkileri bastırmak için yüksek döngü kazançları sağlanırken aynı zamanda yeterli kararlılığı da sağlamak gereklidir. Gimballi görüntüleme sistemlerinde yapısal rezonanslar ve model belirsizlikleri ulaşılabilecek döngü bant genişliğine sıkı bir sınır koymaktadır. Bu nedenle modelleme hataları altında yüksek stabilizasyon performansı sağlamak için gürbüz denetim yöntemlerini kullanmak gereklidir.

Bu tezde iki eksenli gimbal için gürbüz denetleyicilerin tasarlanması, LQG/LTR, H-sonsuz ve Mu denetleyicileri çerçevesinde anlatılmıştır. İlk olarak modelleme hataları, değişik koşullar altında lokal olarak doğrusallaştırılmış modellerin incelenmesi ile bulunmuştur. Daha sonra performans göstergeleri ve ağırlıkları izin verilen stabilizasyon hatası ve olası bozucu etki profili düşünülerek belirlenmiştir. Üç farklı yöntem için genelleştirilmiş sistemler nominal model ve bulunan ağırlıklar kullanılarak elde edilmişlerdir. Bu genel sistemler kullanılarak LQG/LTR, H-sonsuz ve Mu denetleyicileri sentezlenmiştir. Üç tasarım için kararlılıklar ve performanslar detaylı olarak incelenmiştir. Daha sonra üç denetleyicinin karşılaştırılması kapalı çevrimlerin

gürbüzlükleri incelenerek yapılmıştır. Tez çalışması tasarlanan gürbüz denetleyicilerin geçerliliğini incelemek için deneysel çalışmalar ve performanslar ile bitirilmiştir.

Anahtar Kelimeler: LQG/LTR, H-sonsuz, Mu-sentezi, gürbüz kontrol, bakış hattı stabilizasyonu

To My Family

ACKNOWLEDGMENTS

I would like to express my appreciation to my supervisor Prof. Dr. Kemal Leblebicioğlu for his helpful criticism, guidance and patience in the progress and preparation of this thesis.

The support and facilities provided by ASELSAN Inc. to obtain the experimental results are gracefully appreciated.

I would like to thank The Scientific and Technological Research Council of Turkey for the financial support given by 2211 scholarship program (TÜBİTAK 2211 Yurt İçi Burs Programı).

I would like to thank METU EE Department and faculty members for the high quality education they give us.

I would like to thank all my friends and colleagues who contributed to my thesis with their criticism and encouragement.

Finally, I am very grateful to members of my family for their support and encouragement during my study and my life.

TABLE OF CONTENTS

LIST OF TABLES

TABLES

LIST OF FIGURES

FIGURES

LIST OF SYMBOLS

$\mathbb{R}$ and $\mathbb{C}$	fields of real and complex numbers
$\mathbb{F}$	field, either $\mathbb{R}$ or $\mathbb{C}$
$\mathbb{F}^n$	vector space over $\mathbb{F}$
$\mathbb{R}^{mxn}$	all *n x m* real matrices
$\mathbb{C}^{mxn}$	all *n x m* complex matrices
$j\mathbb{R}$	imaginary axis
$\in$	belongs to
$:=$	defined as
>> and <<	much greater and less than
$\lvert a \rvert$	absolute value of $a \in \mathbb{C}$
$\mathrm{Re}(a)$	real part of $a \in \mathbb{C}$
$x \sim (a,b)$	x is normal with mean a and variance b
I_n or I_{nxn}	a *n x n* identity matrix
0_n or 0_{mxn}	a entirely zero matrix of corresponding dimensions
$\mathrm{diag}(a_1,...,a_n)$	an *n x n* diagonal matrix with a_i as its i^{th} diagonal element
$\langle\ ,\ \rangle$	inner product
$\mathcal{L}_2(-\infty,\infty)$	time domain square integrable functions
$\mathcal{L}_2(j\mathbb{R})$	square integrable functions on $j\mathbb{R}$ including at ∞
$\mathcal{H}_2$	subspace of $\mathcal{L}_2(j\mathbb{R})$ with functions analytic in $\mathrm{Re}(s) > 0$
$\mathcal{L}_\infty(j\mathbb{R})$	functions bounded on $\mathrm{Re}(s) = 0$ including ∞
$\mathcal{H}_\infty$	the set of $\mathcal{L}_\infty(j\mathbb{R})$ functions analytic in $\mathrm{Re}(s) > 0$
prefix B	closed ball
prefix $\mathcal{R}$	real rational
$F^{\sim}(s)$	shorthand for $F^T(-s)$
$\left[\begin{array}{c\|c} A & B \\ \hline C & D \end{array}\right]$	shorthand for state space realization $C(sI-A)^{-1}B+D$
$\mathcal{F}_\ell(M,Q)$	lower LFT
$\mathcal{F}_u(M,Q)$	upper LFT

for $A \in \mathbb{C}^{mxn}$:

A^T and A^*	transpose and complex conjugate transpose of A
$\left[a_{ij}\right]$	a matrix with a_{ij} as its i^{th} row and j^{th} column element
$\bar{\sigma}(A)$ and $\underline{\sigma}(A)$	the largest and the smallest singular values of A
$\sigma_i(A)$	i^{th} singular value of A
$\|A\|_2$	$\mathcal{H}_2$ norm of a transfer matrix A
$\|A\|_\infty$	$\mathcal{H}_\infty$ norm of a transfer matrix A

for $A \in \mathbb{C}^{nxn}$:

A^{-1}	inverse of A
$\det(A)$	determinant of A
$\text{trace}(A)$	trace of A
$\lambda(A)$	eigenvalue of A
$\rho(A)$	spectral radius of A $\left(\rho(A) := \max_{1 \le i \le n} \lvert\lambda_i\rvert\right)$

LIST OF ABBREVIATIONS

ARE	algebraic Riccati equation
CD-EKF	continuous-discrete EKF
EKF	extended Kalman filter
KF	Kalman filter
LFT	linear fractional transformation
LQ	linear quadratic
LQG	linear quadratic Gaussian
LOS	line of sight
LTI	linear time invariant
LTR	loop transfer recovery
MIMO	multi-input multi-output
NP	nominal performance
NS	nominal stability
RHP	right half plane $\mathrm{Re}(s) > 0$
RP	robust performance
RS	robust stability
SISO	single-input single-output

CHAPTER 1

INTRODUCTION

1.1. Problem Definition

A vector drawn from an observer to an object being observed is defined as line of sight (LOS) in literature. LOS control on the other hand deals with the problem of maintaining a sensor's aim point along the line of sight. The LOS error between the aim point and the target results from the kinematics between the target and platform, as well as the platform motion disturbances. So, for any pointing and tracking systems mounted on mobile platforms, there is need of some mechanism to isolate the camera, laser or any other sensor from platform motions. The LOS control problem deals with this phenomenon.

The LOS control problem can be divided into two parts. The first part is called tracking and it is related with the sensor to target kinematics. The tracking problem is usually solved by using a servo loop around the sensor. The second problem is named as disturbance rejection and it is related with the isolation of the sensor from the disturbances created by platform motions. It is defined as LOS stabilization problem, and it is solved by closing a servo loop around an inertial sensor [1]. In this thesis, only the LOS stabilization problem is discussed.

Use of multi-axis gimbals in pointing and tracking system to direct the LOS is a common way. The camera or sensor is usually mounted on a multi-axis gimbal, which is an electromechanical structure that provides rotary motion of the sensor aim point. During the operation of the pointing and tracking system, the LOS is disturbed by the platform motions and vibrations. These movements are sensed by inertial rate sensors or gyros, and they are minimized by the designed feedback control loops.

The typical servo control structure for LOS control is shown in Fig. 1. The inner LOS stabilization loop uses gyro to sense the motions relative to inertial frame.

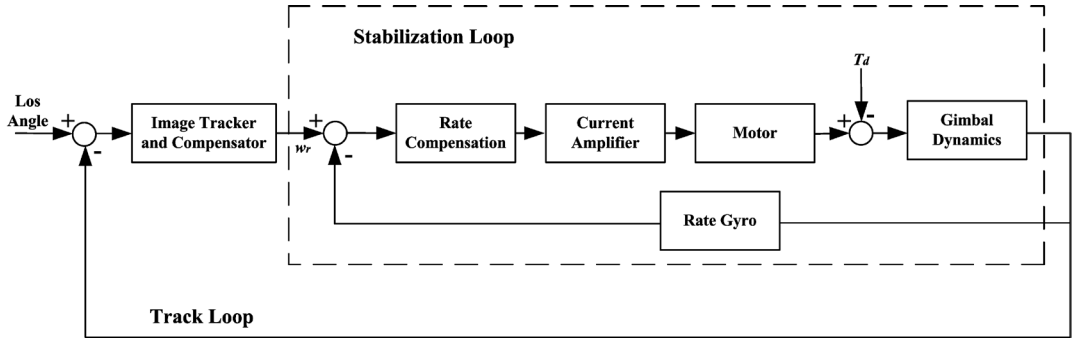

Figure 1: LOS control structure

The rate compensator uses this angular rate information as a feedback and creates torques with motors. By doing that, the angular jitter created by platform motions, noises and disturbance torques (frictions, imbalances and others) is minimized [1, 2].

In order to design a good stabilization loop, high gain compensation is required. While satisfying high loop gains for disturbance attenuation, it is also required to satisfy sufficient loop stability. Structural resonances and model uncertainties put strict restrictions on achievable stabilization loop bandwidth for gimbaled vision systems. For that reason, satisfying high stabilization performance under modeling errors requires utilization of robust control methods.

Since the tracking and pointing performances are directly related to inner stabilization loop, in this thesis designing a stabilization loop for a two-axis gimbal will be discussed.

1.2. Previous Research

Generally in the past, classical controller with PI and lead lag compensators is used in stabilization loops [1, 2]. However, these classical control techniques are iterative processes and they usually take very long time to find satisfactory results. Moreover, considering optimality point of view, these techniques are insufficient. Also, in recent years, different techniques are applied to improve the stabilization loop performance. The applications of linear quadratic methods can be found in [3-6]. Moreover, the $\mathcal{H}_\infty$ methods are discussed in [7, 8]. However, lots of control designs are made only for a nominal model. In most of the reported designs, there is no analysis done for the performance change under the model perturbations or modeling errors. In other words, the control design looking sufficient for nominal plant may be insufficient under some

model perturbations. In reality, all the models include some modeling errors due to unmodeled dynamics. In gimbal applications, the uncertainty of the actuators, some unmodeled dynamics in high frequencies, rate gyro sensor delay, structural resonances and nonlinear friction in the model are typical source of the model perturbations. Considering these facts, it requires utilization of robust control methods for good stabilization performance. There are also robust control methods used for the LOS stabilization [9, 10]. However, the designs that claim robustness are either insufficient to prove their claim or they lack of some experimental data to validate them.

1.3. Contributions of Research

In this thesis, design of robust line of sight controller in the LQG/LTR, $\mathcal{H}_\infty$ and μ frameworks is reported. All three designs use a similar loop shaping idea for the controller design.

In many LQG/LTR based designs, the desired loop shape is tried to be reached by adjusting the weighting matrices or changing the intensities of process and measurement noises. However, this method is iterative and usually takes time to reach the successful results. If the cost function of the loop transfer recovery (LTR) is considered, it is seen that there is a better way to obtain the desired loop shape [11]. When the original plant is augmented with transfer matrix which reflects the disturbance power spectrum, LTR tries to shape the sensitivity at the plant output. Since this method is uncommon, utilization of this technique is valuable.

On the other hand, $\mathcal{H}_\infty$ and μ-synthesis designs are treated in mixed sensitivity methodology [12, 13]. Even if these methods are mostly used by control designers, they differ from the other reported designs. In the previous research, the uncertainty modeling is made by using generic facts. For example, by accepting that the uncertainty is small at low frequency region and increases at high frequencies, one selects a corresponding transfer matrix. However, finding exact values of uncertainties by using experimental data is unusual. In this thesis, the uncertainties are determined by using experimental data.

Similarly, in the previous works the performance determination using experimental data is not common. In this aspect, performance weight determination is obtained by looking at the experimental disturbance profile. By considering the requirements on output error

due to measured disturbance profile, the corresponding performance weights are derived. In the same manner, the control weight selection is made by keeping the actuators away from saturation due to the known disturbance profile.

Moreover, in most designs the robustness is only examined by looking at only theoretical results. Considering this fact, the robustness of the controllers is evaluated by looking at both theoretical and experimental results.

Next, the comparison of the LQG/LTR, $\mathcal{H}_\infty$ and μ controllers is made both theoretically and experimentally. The comparison of these three techniques which shares the similar loop shaping idea is rare. In this aspect, it is a considerable contribution.

Please observe that the electromechanical systems are nonlinear in nature. However, local linearization of a nonlinear model at different input levels gives much information about the system. In this thesis, locally linearized models are assumed to be perturbations of actual nonlinear model, and the nonlinear model is represented by this linear model set. In other words, the robust control of these linear models corresponds to the robust control of the actual nonlinear model. In this aspect, this idea is valuable.

1.4. Outline of the Thesis

The remainder of the thesis can be outlined as below:

Chapter 2 explains the background of robust control theory. $\mathcal{H}_2$ and $\mathcal{H}_\infty$ spaces are discussed. Next, both the calculation of $\mathcal{H}_2$ and $\mathcal{H}_\infty$ norms and the importance of these norms are considered. After that, the performance indices of the feedback loops are introduced. The importance of the loop shaping in feedback design is illustrated. After that, the weighted performance for different norms is expressed. Weight selection for different performance indices and fundamental limitations in controller design are briefly discussed. Then internal stability of the feedback systems and their conditions are given. Different perturbation representations and their effects on Nyquist plots are examined. Nominal stability, nominal performance, robust stability and robust performance are defined. For different uncertainty modeling, robust stability and performance conditions are given. Next, the linear fractional transformation (LFT) structures are introduced. Finally, the motivations behind the μ-synthesis and its approximate solution *D-K* iteration are examined.

In Chapter 3, the design methods that are used for LOS stabilization are investigated. First, the properties of LQG/LTR design and its motivation are discussed. Then how LQG/LTR is modified such that it becomes a very powerful loop shaping design is examined. After that, $\mathcal{H}_2$ and $\mathcal{H}_\infty$ controller design methods and their solutions are discussed. After giving $\mathcal{H}_2$ equivalency of LQG design, the mixed sensitivity $\mathcal{H}_\infty$ controller synthesis and its motivation are given. Finally, Chapter 3 ends with the construction of LFT structures that will be used for μ-synthesis and analysis.

In Chapter 4, the experimental setup where the data is obtained and algorithms are validated is illustrated. The working principle of the system and how the data is obtained are illustrated briefly.

Chapter 5 is devoted to the modeling and identification of the two-axis gimbal system. First, the dynamic equations of the gimbal are derived. Then unknown parameters are identified using CD-EKF and experimental data. Then the constructed models with the estimated parameters are compared with experimental data obtained from system. Finally, the MIMO model of the two-axis gimbal is constructed.

In Chapter 6, the LOS control problem is further examined. The motivations and the requirements are explained. The disturbance profile of the platform where the gimbal will be used is obtained from experimental measurements. To satisfy the requirements, the performance weights are determined using the experimental measurement and the system information. Finally, the uncertainty upper bounds are derived from the experimental data obtained by exciting the system with different control input levels. In other words, the nonlinear gimbal model is linearized at different operating points, and the resulting linear models are used to construct the model set that will be used in robust control synthesis.

Chapter 7 includes the theoretical results of the design methods. The robustness of the closed loops created with LQG/LTR, $\mathcal{H}_\infty$ and μ controllers are investigated. First, the singular value tests are used for robustness analysis when the performance criterion depends only on weighted output sensitivity. Next, the robustness is investigated in μ framework by changing the performance criterion. Finally, the comparison of these three techniques is discussed.

In Chapter 8, firstly the implementation of the controllers is discussed. Next, the experimental closed loop responses are given. After that, stability and performance properties are investigated. Then the theoretical and experimental results are compared. Finally, the comparison of three controllers is discussed.

Chapter 9 summarizes the thesis. Then the important results derived throughout the thesis are explained. After that, advantages and disadvantages of these controllers are explained. Chapter 9 is concluded by discussing some future applications.

CHAPTER 2

ROBUST CONTROL THEORY

Main motivation of this chapter is to give a brief summary of robust control theory. While the chapter progress, it benefits from [12] as a guide. For further reading on robust control theory, one can investigate the references [12-15].

2.1. Linear Algebra Preliminary

In this section, some background material is reviewed that will be used in the following sections.

2.1.1. Linear Subspaces

Let $\mathbb{R}$ and $\mathbb{C}$ denote the real and complex scalar field respectively, and let $\mathbb{F}$ be either $\mathbb{R}$ or $\mathbb{C}$ and $\mathbb{F}^n$ be the vector space over $\mathbb{F}$. Let $x_1, x_2, x_3, ..., x_k \in \mathbb{F}^n$ and $a_i, \ldots, a_k \in \mathbb{F}$. Then the linear combinations of all these vectors is called the span of $x_1, x_2, x_3, ..., x_k \in \mathbb{F}^n$ and defined as Eq. (2.1).

$$\text{span}\{x_1, x_2, x_3, ..., x_k\} := \{x = a_1x_1 + ... + a_kx_k\} \tag{2.1}$$

A set of vectors $x_1, x_2, x_3, ..., x_k \in \mathbb{F}^n$ is said to be linearly dependent over $\mathbb{F}$ if there exists $a_i, \ldots, a_k \in \mathbb{F}$ not all zero such that $a_1x_1 + ... + a_kx_k = 0$ is satisfied; otherwise, the vectors are called linearly independent [12].

Let S be a subspace of $\mathbb{F}^n$, and the set $\{x_1, x_2, x_3, ..., x_k\} \in S$ is called a basis for S if $x_1, x_2, x_3, ..., x_k$ are linearly independent.

The set $\{x_1, x_2, x_3, ..., x_k\}$ is mutually orthogonal if $x_i^* x_j = 0$ for all $i \neq j$ and orthonormal if $x_i^* x_j = \delta_{ij}$ where $\delta_{ij} = 1$ if $i = j$, and $\delta_{ij} = 0$ if $i \neq j$. The subspaces $S_1, S_2, ..., S_k$ are mutually orthogonal if $x^* y = 0$ for $x \in S_i$ and $y \in S_j$ for $i \neq j$.

A square matrix $U \in \mathbb{F}^{n \times n}$ whose columns form an orthonormal basis for $\mathbb{F}^n$ is called a unitary matrix and it satisfies $U^*U = UU^*$.

Let $A = [a_{ij}] \in \mathbb{C}^{nxn}$, and then the trace of A is defined as Eq. (2.2).

$$\text{trace}(A) := \sum_{i=1}^{n} a_{ii} \tag{2.2}$$

2.1.2. Eigenvalues and Eigenvectors

Let $A \in \mathbb{C}^{nxn}$, and then the eigenvalues of A are the roots of the characteristic polynomial $p(\lambda) = \det(\lambda I - A)$. The spectral radius is said to be maximum modulus of the eigenvalues and denoted by Eq. (2.3) [12].

$$\rho(A) := \max_{1 \le i \le n} |\lambda_i| \tag{2.3}$$

A nonzero vector $x \in \mathbb{C}^n$ is called right eigenvector if it satisfies Eq. (2.4). Similarly, it is called left eigenvector if it satisfies Eq. (2.5).

$$Ax = \lambda x \tag{2.4}$$

$$x^* A = \lambda x^* \tag{2.5}$$

2.1.3. Vector and Matrix Norms

Let X be a vector space, and then a real valued function $\|.\|$ is said to be norm if the conditions (i-iv) are satisfied [12].

(i) $\|x\| \ge 0$ (positivity);

(ii) $\|x\| = 0$ iff $x = 0$ (positive definiteness);

(iii) $\|ax\| = |a|\|x\|$, for any schalar a (homogeneity);

(iv) $\|x + y\| \le \|x\| + \|y\|$ (triangle inequality);

Then for $x \in \mathbb{C}^n$ the vector p-norm is defined as Eq. (2.6).

$$\| x \|_p := \left(\sum_{i=1}^{n} | x_i |^p \right)^{1/p}, \text{ for } 1 \le p \le \infty \tag{2.6}$$

For $A = [a_{ij}] \in \mathbb{C}^{mxn}$ the induced matrix p-norm is defined as Eq. (2.7).

$$\| A \|_p := \sup_{x \ne 0} \frac{\| Ax \|_p}{\| x \|_p} \tag{2.7}$$

When one considers in terms of system theory, the induced norm can be viewed as input/output amplification gains [12].

2.1.4. Singular Value Decomposition

The singular values of a matrix give very good information about the size of the matrix [12].

Theorem: Let $A \in \mathbb{F}^{m\,x\,n}$. There exist unitary matrices U and V given by Eqs. (2.8) and (2.9) such that Eq. (2.10) is satisfied.

$$U = [u_1,\ u_2,\ \ldots,\ u_m] \in \mathbb{F}^{m x m} \tag{2.8}$$

$$V = [v_1,\ v_2,\ \ldots,\ v_n] \in \mathbb{F}^{n x n} \tag{2.9}$$

$$A = U \Sigma V^* \tag{2.10}$$

Σ, which is given in Eq. (2.10) has the form expressed in Eq. (2.11), and the diagonal elements satisfy Eq. (2.12).

$$\Sigma = \begin{bmatrix} \Sigma_1 & 0 \\ 0 & 0 \end{bmatrix},\ \Sigma_1 = \begin{bmatrix} \sigma_1 & 0 & \ldots & 0 \\ 0 & \sigma_2 & \ldots & 0 \\ \vdots & \vdots & \ddots & \vdots \\ 0 & 0 & \ldots & \sigma_p \end{bmatrix} \tag{2.11}$$

$$\sigma_1 \geq \sigma_2 \geq \cdots \geq \sigma_p \geq 0,\quad p = \min\{m, n\} \tag{2.12}$$

Let σ_i is the i^{th} singular value, and u_i and v_j are the i^{th} left singular vector and j^{th} right singular vector respectively. Then the identities (i-ii) can be derived [12].

(i) $Av_i = \sigma_i u_i$

(ii) $A^* u_i = \sigma_i v_i$

Next, (i-ii) can be rearranged as (iii-iv).

(iii) $A^* A v_i = \sigma_i^2 v_i$

(iv) $AA^* u_i = \sigma_i^2 u_i$

So, σ_i^2 is the eigenvalues of A^*A or AA^*, and u_i is the eigenvector of AA^*, and v_i is the eigenvector of A^*A, and singular value decomposition is found using these facts.

The following notations are usually used:

$$\bar{\sigma}(A) = \sigma_{\max}(A) = \sigma_1 = \text{the largest singular value of } A$$

$$\underline{\sigma}(A) = \sigma_{\min}(A) = \sigma_p = \text{the smallest singular value of } A$$

The singular values of matrix A are the lengths of the semi-axes of the hyperellipsoid E defined as Eq. (2.13) [12].

$$E = \left\{ y : y = Ax,\ x \in \mathbb{C}^n,\ \|x\| = 1 \right\} \tag{2.13}$$

In brief, v_1 can be viewed as the direction in which $\|y\|$ is largest for $\|x\| = 1$. Similarly, v_n can be thought as the direction in which $\|y\|$ is smallest for $\|x\| = 1$.

When one considers from input/output point of view, v_1 is the highest gain input direction, while u_1 is the highest gain output direction. In the same manner, v_n corresponds to the lowest gain input direction while u_n corresponds to the lowest gain output direction [12].

2.2. Performance Specification

In this section, first $\mathcal{H}_2$ and $\mathcal{H}_\infty$ spaces are discussed. Next, $\mathcal{H}_2$ and $\mathcal{H}_\infty$ norms, their importance and calculations are expressed. Then $\mathcal{H}_2$ and $\mathcal{H}_\infty$ control problems and their formulations are considered. After that, selection of weighting functions in optimal control problems is reviewed.

2.2.1. $\mathcal{H}_2$ and $\mathcal{H}_\infty$ Spaces

The aim of the control system is to obtain certain performance requirements and provide internal stability at the same time. Most of the time, the performance can be described by the size of certain signals. For example, one can measure the performance of a tracking system by the size of the tracking error signal. The designer may also want to minimize the size of control signals. So, in this part of the thesis, different ways of interpreting the size of the relevant signals will be discussed [12].

2.2.1.1. Hilbert Spaces

A Hilbert space is a complete inner product space with the norm induced by its inner product. A well known Hilbert space is $\mathcal{L}_2$, which consists of square integrable functions with the inner product defined as Eq. (2.14).

$$\langle f,g\rangle := \int_{-\infty}^{\infty} f(t)^* g(t)dt \ , \ f,g \in \mathcal{L}_2 \tag{2.14}$$

If functions are vector or matrix valued the inner product given in Eq. (2.15) is used.

$$\langle f,g\rangle := \int_{-\infty}^{\infty} \text{trace}\left[f(t)^* g(t) \right] dt \tag{2.15}$$

2.2.1.2. $\mathcal{H}_2$ and $\mathcal{H}_\infty$ Spaces

$\mathcal{L}_2(j\mathbb{R})$ Space:

In frequency domain $\mathcal{L}_2$ is a Hilbert space of matrix-valued functions on imaginary axis with the inner product and norm defined as Eq. (2.16) and Eq. (2.17) respectively.

$$\langle F,G\rangle := \frac{1}{2\pi} \int_{-\infty}^{\infty} \text{trace}\left[F(jw)^* G(jw) \right] dw \tag{2.16}$$

$$\|F\|_{\mathcal{L}2} := \sqrt{\langle F,F\rangle} \tag{2.17}$$

The real rational strictly proper transfer matrices with no poles on the imaginary axis form a closed subspace of $\mathcal{L}_2$, and denoted by $\mathcal{RL}_2$. (By real rational transfer matrices, the transfer matrices which are composed of rational functions of s with real coefficients in numerator and denominator are meant. For example, the transfer matrix which includes delay could not be represented by transfer functions having finite number of poles and zeros, so they are not real rational.)

$\mathcal{H}_2$ Space:

$\mathcal{H}_2$ is a closed subspace of $\mathcal{L}_2$ with F is analytic in RHP. Norm for $\mathcal{H}_2$ is calculated in the same way as $\mathcal{L}_2$ as given by Eq. (2.18). The real rational subspace of $\mathcal{H}_2$, which includes strictly proper and real rational stable transfer matrices, is denoted by $\mathcal{RH}_2$.

$$\|F\|_{\mathcal{L}2}^2 = \|F\|_2^2 = \frac{1}{2\pi} \int_{-\infty}^{\infty} \text{trace}\left[F(jw)^* F(jw) \right] dw \tag{2.18}$$

$\mathcal{L}_\infty(j\mathbb{R})$ Space:

$\mathcal{L}_\infty$ is a Banach space of matrix valued functions that are (essentially) bounded on imaginary axis with the norm defined as Eq. (2.19).

$$\|F\|_\infty := \operatorname{ess\,sup}_{w \in \mathbb{R}} \bar{\sigma}\left[F(jw) \right] \tag{2.19}$$

The real rational proper transfer matrices with no poles on the imaginary axis form a closed subspace of $\mathcal{L}_\infty$, and it is denoted by $\mathcal{RL}_\infty$.

$\mathcal{H}_\infty$ Space:

$\mathcal{H}_\infty$ is a closed subspace of $\mathcal{L}_\infty$ with functions analytic in RHP, and $\mathcal{H}_\infty$ norm is defined as Eq. (2.20).

$$\|F\|_\infty := \sup_{\mathrm{Re}(s)>0} \bar{\sigma}\left[F(jw)\right] = \sup_{w\in\mathbb{R}} \bar{\sigma}\left[F(jw)\right] \tag{2.20}$$

The real rational subspace of $\mathcal{H}_\infty$ which includes proper and real rational stable transfer matrices is denoted by $\mathcal{RH}_\infty$.

2.2.1.3. Computation of $\mathcal{L}_2$ and $\mathcal{H}_2$ Norms

$$\|F\|_2^2 := \frac{1}{2\pi}\int_{-\infty}^{\infty} \mathrm{trace}\left[F(jw)^* F(jw)\right] dw \tag{2.21}$$

$\mathcal{L}_2$ norm defined as Eq. (2.21) is finite if the transfer matrix F is strictly proper. Assuming F to be strictly proper, $\mathcal{L}_2$ norm is obtained by using contour integral along imaginary axis and infinite semicircle in the LHP [12].

$$\|F\|_2^2 = \frac{1}{2\pi j}\oint \mathrm{trace}\left[F(jw)^{\sim} F(jw)\right] dw \tag{2.22}$$

Utilization of state space methods for computation of $\|F\|_2$ is generally preferred over contour integral given in Eq. (2.22). To determine the norm of a transfer matrix in $\mathcal{RH}_2$ the rule given by Eq. (2.24) is used, where Q and P matrices represent the observability and controllability Grammians [12], and A, B, C are the corresponding matrices of the state space representation expressed in Eq. (2.23) of strictly proper transfer matrix F.

$$F(s) = \left[\begin{array}{c|c} A & B \\ \hline C & 0 \end{array}\right] \tag{2.23}$$

$$\|F\|_2^2 = \mathrm{trace}(B^* Q B) = \mathrm{trace}(C P C^*) \tag{2.24}$$

2.2.1.4. Computation of $\mathcal{L}_\infty$ and $\mathcal{H}_\infty$ Norms

$\mathcal{H}_\infty$ norm of a transfer matrix can be obtained by evaluating the transfer matrices over a grid of frequencies, and then taking the maximum singular value of those frequencies.

There is also a state space method available. Let $\gamma > 0$ and F be proper transfer matrix, and let A, B, C, D be the matrices of its state space representation given in Eq. (2.25).

$$F(\mathrm{s}) = \left[\begin{array}{c|c} A & B \\ \hline C & D \end{array}\right] \in \mathcal{RH}_\infty \tag{2.25}$$

Then $\|F\|_\infty < \gamma$ is satisfied if and only if $\bar{\sigma}(D) < \gamma$ and the Hamiltonian matrix H defined as Eq. (2.26) has no eigenvalues on the imaginary axis [12] where $R = \gamma^2 I - D^* D$.

$$H := \begin{bmatrix} A + BR^{-1}D^*C & BR^{-1}B^* \\ -C^*(I + DR^{-1}D^*)C & -(A + BR^{-1}D^*C)^* \end{bmatrix} \tag{2.26}$$

Bisection algorithm uses this fact and iteratively changes the upper and lower bounds. It makes the interval ($\gamma_l < \|F\|_\infty < \gamma_u$) smaller at each iteration and finds $\|F\|_\infty$ numerically within the specified tolerances [12].

2.2.2. Importance of $\mathcal{H}_2$ and $\mathcal{H}_\infty$ Norms

Most of the time, the performance can be described by the size of certain signals. For example, consider the system given in Fig. 2 where P is the augmented plant with different performance weights. Let e be the output of augmented system and it can be actuator signals, or tracking errors of the closed loop system. In other words, in the system e represents the signals that are desired to be small. Further assume that w is input to the augmented plant and it can include exogenous references or disturbance signals. For simplicity let w be scalar (it is easily generalized for spatial domain by changing absolute values with norms), and it belongs to some special sets given by Eqs. (2.27)-(2.29) where B denotes the unit closed ball. Then one desires to find out the relations between e and w.

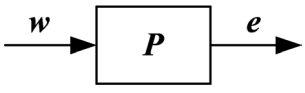

Figure 2: Augmented closed loop system

$$\text{Power: } BP = \left\{ w \mid \lim_{T\to\infty} \frac{1}{2T} \int_{-T}^{T} \left| w(t) \right|^2 dt \le 1 \right\} \tag{2.27}$$

$$\text{Energy: } B\mathcal{L}_2 = \left\{ w \mid \left\| w \right\|_2^2 = \int_{-\infty}^{\infty} \left| w(t) \right|^2 dt \le 1 \right\} \tag{2.28}$$

$$\text{Magnitude: } B\mathcal{L}_\infty = \left\{ w \mid \left\| w \right\|_\infty = \operatorname{ess\,sup}_t \left| w(t) \right| \le 1 \right\} \tag{2.29}$$

Equations (2.27)-(2.29) contain the signals having power, energy and magnitude in unit closed ball respectively. By considering different cases, Table 1 can be constructed which shows the relations between different input and output signals [16, 17]. In other words, table entries show the induced norm performance indices for different conditions by assuming P is stable. For example, if output energy due to bounded energy input is interested, one needs to consider $\mathcal{H}_\infty$ norm of the system.

Table 1: Induced norm performance theorems

	Power $w \in BP$	Energy $w \in B\mathcal{L}_2$	Magnitude $w \in B\mathcal{L}_\infty$	Sinusoids $w(t) = \sin wt$	Impulses $w(t) = \delta(t)$
Power: $\left\| e \right\|_P$	$\left\| P(s) \right\|_\infty$	0	$\le \left\| P(s) \right\|_\infty$	$\frac{1}{\sqrt{2}} \left\| P(s) \right\|_\infty$	0
Energy: $\left\| e \right\|_2$	∞	$\left\| P(s) \right\|_\infty$	∞	∞	$\left\| P(s) \right\|_2$
Magnitude: $\left\| e \right\|_\infty$	∞	$\left\| P(s) \right\|_2$	$\left\| p(t) \right\|_1$	$\left\| P(s) \right\|_\infty$	$\left\| p(t) \right\|_\infty$

Consider the case where $w \in B\mathcal{L}_2$, $\left\| w \right\|_2 \le 1$, and one investigates the energy of the error signal e. So, when unit energy signal enters the system, $\left\| e \right\|_2$ remains small, if $\mathcal{H}_\infty$ norm of the system is minimized as expressed in Eq. (2.30).

$$\begin{aligned} \left\| e \right\|_2^2 &= \frac{1}{2\pi} \int_{-\infty}^{\infty} w(jw)^* P(jw)^* P(jw) w(jw) dw \le \left\| P(s) \right\|_\infty^2 \frac{1}{2\pi} \int_{-\infty}^{\infty} \left| w(jw) \right|^2 dw \\ \Rightarrow \left\| e \right\|_2 &= \left\| P(s) \right\|_\infty \left\| w \right\|_2 \end{aligned} \tag{2.30}$$

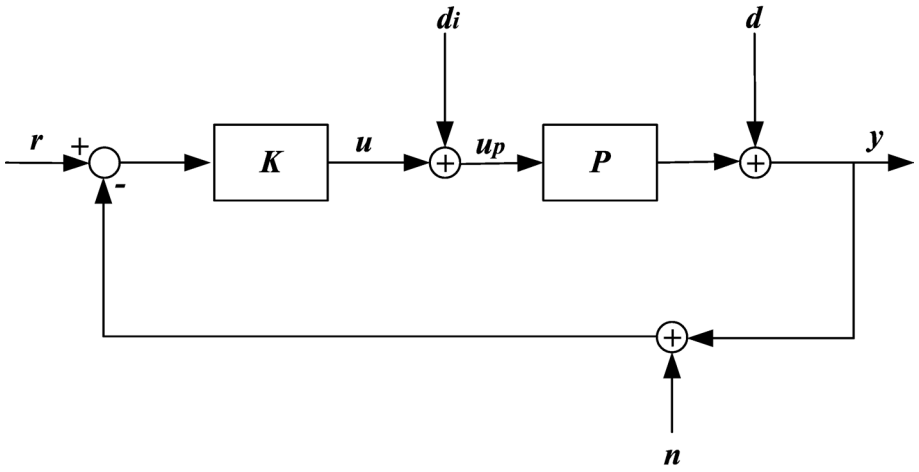

Figure 3: Standard feedback loop

The underlying reason behind the popularity of $\mathcal{H}_2$ and $\mathcal{H}_\infty$ control lies in Table 1. Since $\mathcal{H}_2$ and $\mathcal{H}_\infty$ are most common norms in the Table 1, $\mathcal{H}_2$ and $\mathcal{H}_\infty$ control methods has gained popularity in last few decades.

2.2.3. Measure of Performance in Feedback System

In this section, the properties of feedback are discussed. The standard equations of a feedback loop are examined. The benefits of feedback and design tradeoffs while designing control loop are also investigated [12].

Consider the standard feedback configuration given in Fig. 3, and define the following transfer matrices:

Input open loop transfer matrix (when the loop is broken at *u*) is $L_i = KP$.

Output open loop transfer matrix (when the loop is broken at *y*) is $L_o = PK$.

The input sensitivity matrix (transfer matrix from d_i to u_p) is $S_i = \left(I + L_i\right)^{-1}$.

The output sensitivity matrix (transfer matrix from *d* to *y*) is $S_o = \left(I + L_o\right)^{-1}$.

The input and output complementary sensitivity matrices are $T_i = I - S_i = L_i\left(I + L_i\right)^{-1}$ and $T_o = I - S_o = L_o\left(I + L_o\right)^{-1}$ respectively. The input and output return difference matrices $I + L_i$ and $I + L_o$ respectively. If the closed loop is internally stable, it satisfies Eqs. (2.31)-(2.34).

$$y = T_o(r-n) + S_o P d_i + S_o d \tag{2.31}$$

$$r - y = S_o(r-d) + T_o n - S_o P d_i \tag{2.32}$$

$$u = KS_o(r-n) - KS_o d - T_i d_i \tag{2.33}$$

$$u_p = KS_o(r-n) - KS_o d + S_i d_i \tag{2.34}$$

These equations show not only the fundamental benefits but also the design objectives in a feedback system. As an example, making output sensitivity S_o small reduces the effect of the output disturbance d on the output y as seen in Eq. (2.31). Similarly, Eq. (2.34) shows that small input sensitivity S_i leads to small effect of input disturbance d_i on the plant input u_p. Generally, use of frequency dependent singular values is preferred while analyzing the smallness of the transfer matrices. For example, making $\bar{\sigma}(S_o) < 1$ at some frequencies means that disturbance d is suppressed at those frequencies. Therefore, to reduce the disturbance effects on the output y, the transfer matrices given in Eqs. (2.35) and (2.36) need to be small over the specified interval.

$$\bar{\sigma}(S_o) = \bar{\sigma}\left((I+PK)^{-1}\right) = \frac{1}{\underline{\sigma}(I+PK)} \left(\text{for disturbance at plant output}, d\right) \tag{2.35}$$

$$\bar{\sigma}(S_o P) = \bar{\sigma}\left((I+PK)^{-1} P\right) = \bar{\sigma}(PS_i) \ \left(\text{for disturbance at plant input}, d_i\right) \tag{2.36}$$

In a similar fashion, good disturbance rejection at the plant input u_p requires small transfer matrices expressed in Eqs. (2.37) and (2.38) where the disturbances are dominant.

$$\bar{\sigma}(S_i) = \bar{\sigma}\left((I+KP)^{-1}\right) = \frac{1}{\underline{\sigma}(I+KP)} \left(\text{for disturbance at plant input}, d_i\right) \tag{2.37}$$

$$\bar{\sigma}(S_i K) = \bar{\sigma}\left(K(I+PK)^{-1}\right) = \bar{\sigma}(KS_o) \ \left(\text{for disturbance at plant output, } d\right) \tag{2.38}$$

Please observe that Eqs. (2.39) and (2.40) result in Eqs. (2.41) and (2.42).

$$\underline{\sigma}(PK) - 1 \le \underline{\sigma}(I+PK) \le \underline{\sigma}(PK) + 1 \tag{2.39}$$

$$\underline{\sigma}(KP) - 1 \le \underline{\sigma}(I+KP) \le \underline{\sigma}(KP) + 1 \tag{2.40}$$

$$\frac{1}{\underline{\sigma}(PK)+1} \le \bar{\sigma}(S_o) \le \frac{1}{\underline{\sigma}(PK)-1}, \text{ if } \underline{\sigma}(PK) > 1 \tag{2.41}$$

$$\frac{1}{\underline{\sigma}(KP)+1} \le \bar{\sigma}(S_i) \le \frac{1}{\underline{\sigma}(KP)-1}, \text{ if } \underline{\sigma}(KP) > 1 \tag{2.42}$$

So, the results shown in Eqs. (2.43) and (2.44) can be derived easily.

$$\bar{\sigma}(S_o) \ll 1 \Leftrightarrow \underline{\sigma}(PK) \gg 1 \tag{2.43}$$

$$\bar{\sigma}(S_i) \ll 1 \Leftrightarrow \underline{\sigma}(KP) \gg 1 \tag{2.44}$$

Considering the equations above, and assuming invertible P and K, the approximations illustrated in Eqs. (2.45) and (2.46) can be made.

$$\underline{\sigma}(PK) \gg 1 \text{ or } \underline{\sigma}(KP) \gg 1 \Leftrightarrow \bar{\sigma}(S_o P) = \bar{\sigma}\left((I+KP)^{-1} P\right) \approx \bar{\sigma}\left(K^{-1}\right) = \frac{1}{\underline{\sigma}(K)} \tag{2.45}$$

$$\underline{\sigma}(PK) \gg 1 \text{ or } \underline{\sigma}(KP) \gg 1 \Leftrightarrow \bar{\sigma}(KS_o) = \bar{\sigma}\left(K(I+KP)^{-1}\right) \approx \bar{\sigma}\left(P^{-1}\right) = \frac{1}{\underline{\sigma}(P)} \tag{2.46}$$

The meaning of Eqs. (2.31)-(2.46) can be solidified as follows. Good disturbance rejection at the plant output y requires large loop gain $\underline{\sigma}(L_o) = \underline{\sigma}(PK) \gg 1$ where d is significant. Moreover, large controller gain $\underline{\sigma}(K) \gg 1$ is essential where d_i is significant to reduce the effect of d_i.

In the same manner, good disturbance rejection at the plant input requires large loop gain $\underline{\sigma}(L_i) = \underline{\sigma}(KP) \gg 1$ where d_i is significant to minimize the effect of d_i. In addition, big plant gain $\underline{\sigma}(P) \gg 1$ is crucial where d is significant to reduce the effect of d. However, this fact cannot be changed by controller design and should be considered at the stage of plant construction.

In brief, good multivariable feedback design is accompanied with high loop gains in the desired frequency ranges. Even if the comment looks very simple, there are lots to consider while designing feedback loops. For example, the loop gain should not be large at high frequencies. It is not odd to think that there are tradeoffs between disturbance rejection and stability under model uncertainties. Consider the perturbed plant $P = (I+\Delta)P$ where Δ and nominal closed loop are stable. The perturbed system is stable if the determinant given by Eq. (2.47) has no right half plane zeros [12].

$$\det\left(I + (I+\Delta)PK\right) = \det(I+PK)\det(I+\Delta T_o) \tag{2.47}$$

So, when Δ is significant $\bar{\sigma}(T_o)$ has to be small which relates small loop gain $\bar{\sigma}(L_o)$.

Equation (2.31) can be approximated as Eq. (2.48) at low frequencies, and it shows that when high loop gain reduces disturbances, it cannot reduce the effect of noises which are dominant at high frequencies.

$$y = T_o(r-n) + S_o P d_i + S_o d \approx r - n \tag{2.48}$$

Also, under the assumptions of high loop gain $\underline{\sigma}\left(L_o\left(jw\right)\right) \gg 1$ or $\underline{\sigma}\left(L_i\left(jw\right)\right) \gg 1$ and small plant gain $\bar{\sigma}\left(P\left(jw\right)\right) \ll 1$, Eq. (2.33) is approximated as Eq. (2.49). Under the assumption of invertibility of *P*, Eq. (2.49) shows that disturbances and noises are amplified at *u*, and this causes unacceptably large *u* which saturates the actuators. For that reason, high loop gain frequency range is limited for feedback design.

$$u = KS_o\left(r - n - d\right) - T_i d_i \approx P^{-1}\left(r - n - d\right) - d_i \tag{2.49}$$

In a similar way, under small loop gain $\underline{\sigma}\left(L_o\left(jw\right)\right) \ll 1$ or $\underline{\sigma}\left(L_i\left(jw\right)\right) \ll 1$ and high controller gain $\bar{\sigma}\left(K\left(jw\right)\right)$, Eq. (2.33) is approximated as Eq. (2.50). This fact shows that the controller gain should not be large when loop gain is small.

$$u = KS_o\left(r - n - d\right) - T_i d_i \approx K\left(r - n - d\right) \tag{2.50}$$

Under the results gathered throughout this section, good design must have following properties [12]. First, at low frequencies $(0, w_l)$ good performance requires large loop and controller gains $\underline{\sigma}\left(PK\right) \gg 1$, $\underline{\sigma}\left(KP\right) \gg 1$, $\underline{\sigma}\left(K\right) \gg 1$. Next, at high frequencies (w_h, ∞) good robustness and sensor noise reduction requires small loop and controller gains $\bar{\sigma}\left(PK\right) \ll 1$, $\bar{\sigma}\left(KP\right) \ll 1$, $\bar{\sigma}\left(K\right) \le M$. In Fig. 4, all these requirements are shown graphically.

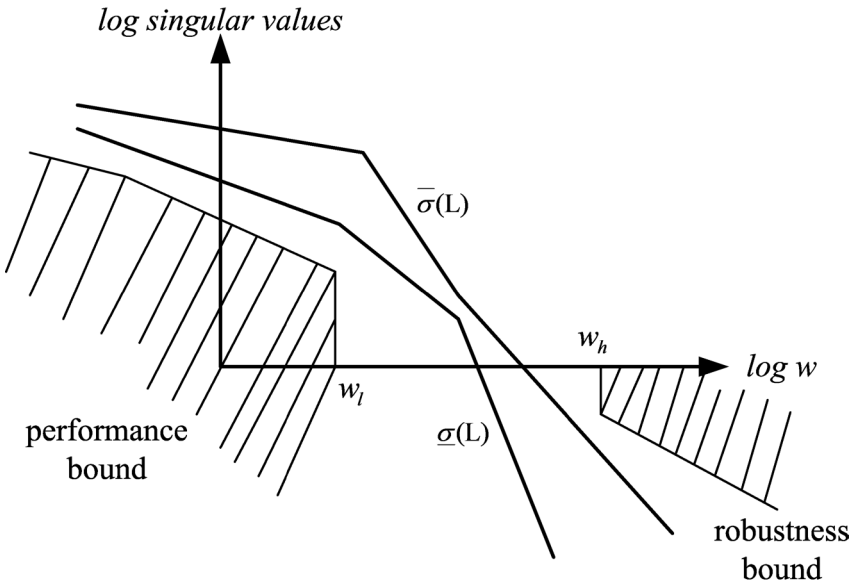

Figure 4: Desired loop gains

2.2.3.1. Weighted $\mathcal{H}_2$ and $\mathcal{H}_\infty$ Performance

As introduced in the previous section, the performance objectives of a feedback system are usually specified by the closed loop transfer matrices such as sensitivity and complementary sensitivity. As an example, for a desired performance, it is required that at low frequencies $\forall w \le w_0,\ \bar{\sigma}(S) \le \varepsilon$ and at high frequencies $\forall w > w_0,\ \bar{\sigma}(S) \le M$ are satisfied.

However, representing these performances as $\bar{\sigma}(W_e S) \le 1,\ \forall w$ is much more efficient where weighting function is given by Eqs. (2.51) and (2.52).

$$\underline{\sigma}(W_e) = 1/\varepsilon,\ \forall w \le w_0 \tag{2.51}$$

$$\underline{\sigma}(W_e) = 1/M,\ \forall w > w_0 \tag{2.52}$$

In MIMO control design, weighted performance usage is essential. For example in MIMO systems, some signals may be more important than others. Similarly, there is a need to compare signals having different units. In these aspects, weighting functions can be used to scale the signals having different units or to emphasize the important signals. More importantly, frequency-dependent weights are used when the error signals are tried to be minimized in the specific frequency ranges.

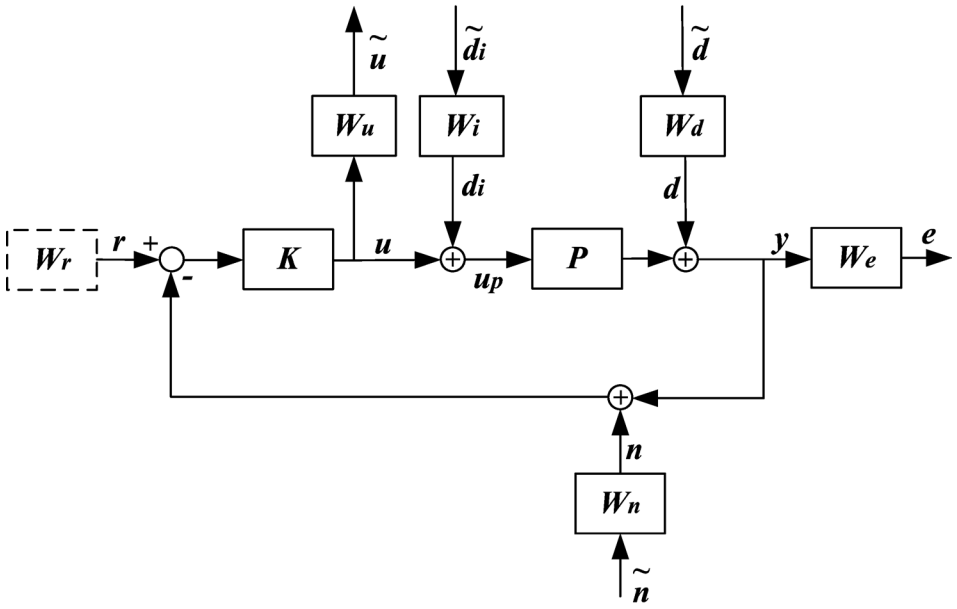

Figure 5: Standard feedback loop with weights

The standard feedback loop discussed previously is now augmented with weighting matrices, and it is shown in Fig. 5.

The weighting matrices in Fig. 5 may be chosen to illustrate design aim, disturbance and noise information. W_d and W_i are usually selected to illustrate frequency content or power spectrum of the signals $\tilde{d}$ and $\tilde{d}_i$. Moreover, W_e is generally used to denote some desired loop shape, and W_n shows frequency content of noise. Usually, W_u is required to limit the actuator signals, and W_r is used to shape the reference command. These weighting matrices play an important role in $\mathcal{H}_2$ and $\mathcal{H}_\infty$ control synthesis. So, the control problem reduces to design a controller K to make the weighted signals as small as possible. According to norm of a signal choice, different controller synthesis can be used. Now different performances are discussed and for simplicity $\tilde{d}_i$ and $\tilde{n}$ are assumed to be zero in Fig. 5.

2.2.3.1.1. $\mathcal{H}_2$ Performance

Consider again Fig. 5 and let disturbance $\tilde{d}$ be illustrated as an impulse with random input direction defined as in Eqs. (2.53) and (2.54) [12].

$$\tilde{d} = \eta\delta(t) \tag{2.53}$$

$$E\left(\eta\eta^*\right) = I \tag{2.54}$$

It desired to minimize the expected energy of e and $\tilde{u}$ due to $\tilde{d}$.

$$E\left\{\int_0^\infty \|e\|_2^2 + \left\|\tilde{u}\right\|_2^2 dt\right\} = \left\|\begin{bmatrix} W_e S_o W_d \\ W_u K S_o W_d \end{bmatrix}\right\|_2^2 \tag{2.55}$$

The cost given by Eq. (2.55) can be considered as a total energy expended by the system to reject disturbance $\tilde{d}$. This problem is named as linear quadratic Gaussian control and became popular in 1960s and 1970s.

2.2.3.1.2. $\mathcal{H}_\infty$ Performance

The use of $\mathcal{H}_2$ norm as a cost leads to a controller having high gain at high frequencies. So, having high gains at high frequencies where the plant is not known exactly creates a serious problem, and the plant perturbations can destabilize the closed loop system. In this case, $\mathcal{H}_\infty$ norm may be helpful. For $\mathcal{H}_\infty$ case, the cost function given by Eq. (2.56)

can be used. In this case, the total energy expended by the system due to $\tilde{d}$ which has bounded energy is minimized.

$$\sup_{\|\tilde{d}\|_2 \le 1} \left\{ \|e\|_2^2 + \|\tilde{u}\|_2^2 \right\} = \left\| \begin{bmatrix} W_e S_o W_d \\ W_u K S_o W_d \end{bmatrix} \right\|_\infty^2 \tag{2.56}$$

When one cares about robustness, the cost in Eq. (2.57) can be preferred,

$$\left\| \begin{bmatrix} W_e S_o W_d \\ W_1 T_o W_2 \end{bmatrix} \right\|_\infty \tag{2.57}$$

where W_1 and W_2 denote frequency dependent uncertainty scaling matrices [12].

2.2.3.2. Weight Selection

Even if every problem posses unique properties, it is possible to discuss general rules applicable to weight selection. For example, some time domain performance criteria like percent overshot and settling time can be given for SISO closed loops. These properties can be interpreted in the frequency domain as bandwidth and peak sensitivity [18]. Therefore, sensitivity function having bandwidth w_b and peak sensitivity M_s is a good performance measure for closed loop systems. So, it is desired that the sensitivity function satisfies Eq. (2.58).

$$\left|S(s)\right| \le \left| \frac{s}{1/M_s + w_b} \right|, \; s = jw, \; \forall w \tag{2.58}$$

$$W_e = \frac{s/M_s + w_b}{s} \tag{2.59}$$

When the weight given by Eq. (2.59) is considered, the objective is satisfied if the inequality $\left|W_e S\right| \le 1$ is satisfied at every frequency. However, to have a solution of $\mathcal{H}_2$ and $\mathcal{H}_\infty$ control, performance and weight functions need to be stabilizable by the control and detectable from the measurements [12]. Clearly, there must be no integrator outside the loop. A small modification is needed such that instead of zero steady state error, very small error is allowed. For small steady state error, the inequalities $\left|S(0)\right| \le \varepsilon$ and $\left|W_e(0)\right| > 1/\varepsilon$ need to be satisfied. Thus, performance is satisfied if inequality $\left\|W_e S\right\|_\infty \le 1$ is achieved where the weight is now modified to one given in Eq. (2.60).

$$W_e = \frac{s/M_s + w_b}{s + w_b \varepsilon} \tag{2.60}$$

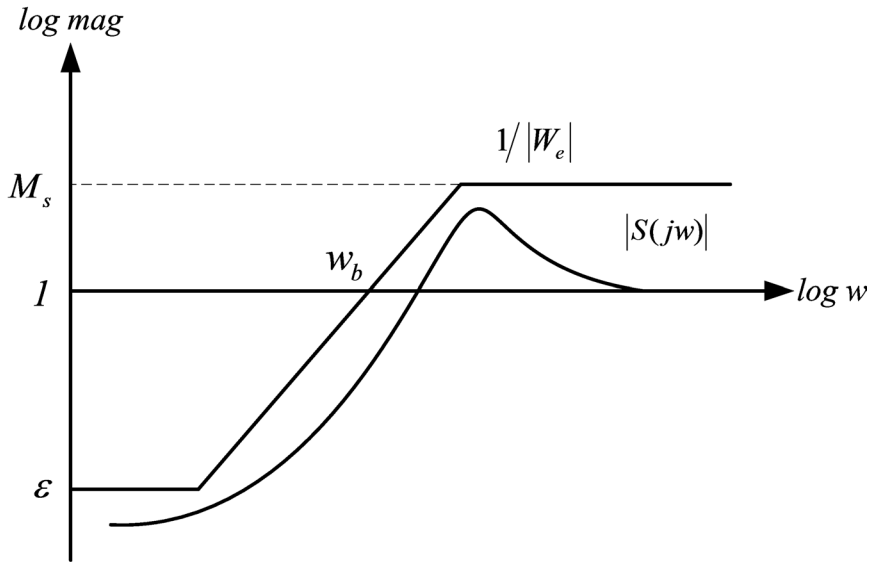

Figure 6: Weight selection for sensitivity

If a steeper transition is desired around crossover, one can choose weighting function in Eq. (2.61) where k denotes a positive integer bigger than one.

$$W_e = \left(\frac{s/\sqrt[k]{M_s} + w_b}{s + w_b \sqrt[k]{\varepsilon}} \right)^k \tag{2.61}$$

Typical weight W_e and sensitivity S are illustrated in Fig. 6. $\|W_e S\|_\infty \le 1$ is satisfied if the sensitivity remains below $1/|W_e|$ at all frequencies as shown in Fig. 6.

Selection of W_u is made considering Eq. (2.62).

$$u = KS_o(r - n - d) - T_i d_i \tag{2.62}$$

The magnitude of $|KS_o|$ in the low frequency region is limited by allowable control effort and actuator saturation. Not to amplify the noises and disturbances at control signals in high frequency region, it is desired to roll off as fast as possible beyond the desired control bandwidth. Possible choice for control weight is given by Eq. (2.63).

$$W_u = \frac{s + w_{bc}/M_u}{\varepsilon_1 s + w_{bc}} \tag{2.63}$$

If faster roll off desired at high frequencies, one can choose weight given in Eq. (2.64).

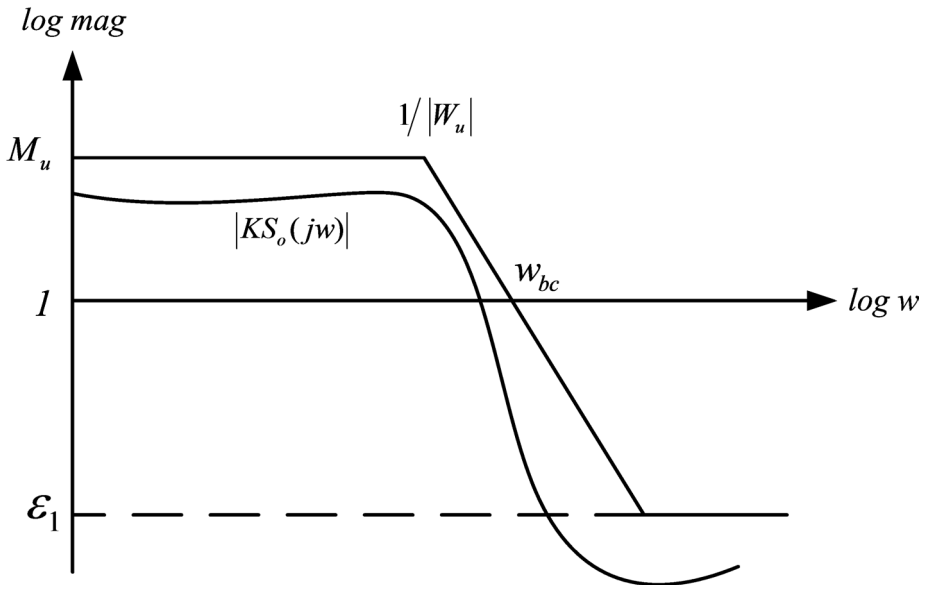

Figure 7: Weight selection for control

$$W_u = \left(\frac{s + w_{bc} / \sqrt[k]{M_u}}{\sqrt[k]{\varepsilon_1}\, s + w_{bc}} \right)^k \tag{2.64}$$

The typical weight W_u and KS_o are illustrated in Fig. 7.

Even if these weights are expressed for SISO system, it can be generalized for MIMO system easily. For example, one can chose the weight as a diagonal matrix whose diagonal elements are in discussed forms above.

2.2.3.2.1. Fundamental Limitations in Feedback Loops

The good control loop design is a tradeoff between performances as discussed earlier. Moreover, stability and robustness also puts restriction to the achievable performance which could not be changed with controller design methods. Existence of RHP zeros and poles also put strict limitation to achievable performance. These limitations need to be considered with care while designing feedback loops and determining performance indices and weighting functions. The details are outside of this thesis; however, interested reader can consult [12-14, 18] to learn much about these fundamental limitations.

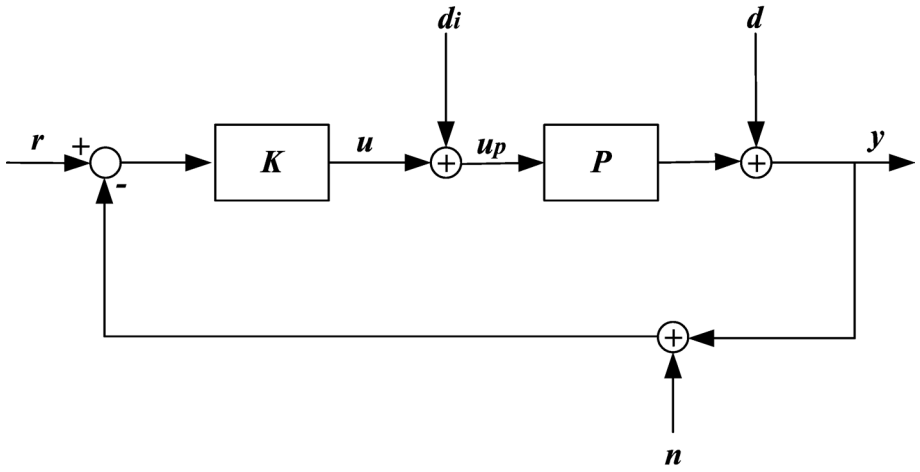

Figure 8: Standard closed loop system

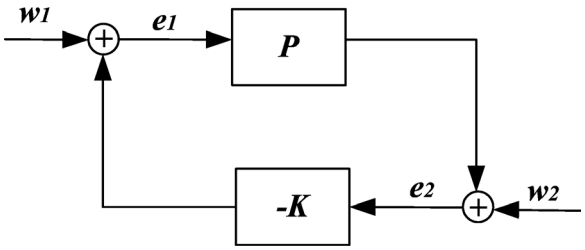

Figure 9: Stability analysis structure

2.3. Internal Stability of Feedback System

In this section, the feedback structure and its stability analysis are discussed. The results obtained here, will be used in the next section to investigate the stability of the feedback systems in the existence of uncertainty.

The standard closed loop given in Fig. 8 can be rearranged such that the structure given in Fig. 9 is obtained, where $w_1 = d_i$, $w_2 = d$, $e_1 = u_p$, $e_2 = y$ are satisfied. (Since the transfer matrix from *d*, *n* and *–r* to *u* are same, in stability analysis *r* and *n* are neglected.) Then the closed loop system is internally stable if the transfer matrix from (w_1, w_2) to (e_1, e_2) given in Eq. (2.65) is in $\mathcal{RH}_\infty$ [12].

$$\begin{bmatrix} I & K \\ -P & I \end{bmatrix}^{-1} = \begin{bmatrix} (I+KP)^{-1} & -K(I+PK)^{-1} \\ P(I+KP)^{-1} & (I+PK)^{-1} \end{bmatrix} \tag{2.65}$$

In brief, to guarantee internal stability, all the four transfer matrices must be in $\mathcal{RH}_\infty$. If there is no pole zero cancellations between P and K in RHP, the closed loop system is internally stable if and only if one of the transfer function in transfer matrix expressed in Eq. (2.65) is in $\mathcal{RH}_\infty$. In other words, one can check only stability of $\left(I+PK\right)^{-1}$ for the internal stability of closed loop system [12].

2.4. Uncertainty and Robustness

In this section, the unstructured uncertainties are discussed to represent the modeling errors of the actual systems. Moreover, the robust stability and robust performance conditions are expressed.

2.4.1. Model Uncertainty

Most control designs are done using a model of the system. However, it is impossible to represent a true plant in terms of a single mathematical model. Therefore, it is customary to represent a plant in terms of a set of models. The uncertainty is the difference between the mathematical model and the actual plant and various representations are available for uncertainty. For example, additive noise having bounded power spectrum in LQG control is one type of uncertainty representation. This type of uncertainty assumes the deviation of the output is independent of the input. However, this representation is not sufficient, because the deviations at the plant output usually depend on input in physical systems [12]. There are two ways of uncertainty representations, namely structured and unstructured. Defining sets for the system parameters are the structured uncertainty example. However, instead of one parameterized system, it is preferable to represent the system as a model set. Simple way to do that is using a frequency domain bounds for model sets. This type of representation does not usually seek to find the error source; therefore, it is called unstructured uncertainty. Since the model error gets bigger as the frequency increases, it is convenient representation for physical system's errors.

In this thesis, unstructured uncertainties are examined. For example, Eq. (2.66) is the representation of this type of error where $P(s)$ is the nominal plant and W_1 is stable transfer functions that illustrate the uncertainty upper bound.

$$P_\Delta\left(s\right)=P\left(s\right)+\Delta\left(s\right)W_1\left(s\right),\ \bar{\sigma}\left[\Delta\left(jw\right)\right]<1,\forall w\geq 0 \tag{2.66}$$

Usually, one chooses $W_1 = w(s)I$ and then the model set P_Δ describes a disc centered at P with radius $w(jw)$ at each frequency as given in Fig. 10.

Apart from this additive form, there is also a multiplicative form given by Eq. (2.67).

$$P_\Delta(s) = \left(I + \Delta(s)W_1(s)\right)P(s),\ \bar{\sigma}\left[\Delta(jw)\right] < 1, \forall w \geq 0 \qquad (2.67)$$

The advantage of multiplicative form over additive form is that, the uncertainty affects both the nominal plant and open loop transfer function $L = PK$ at the same time as illustrated in Fig. 11.

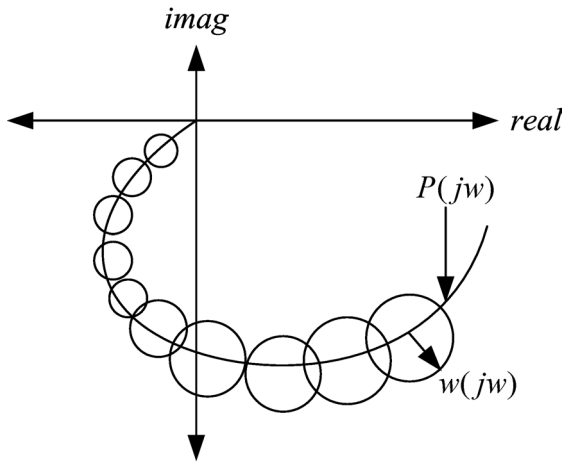

Figure 10: Nyquist diagram of additive uncertainty

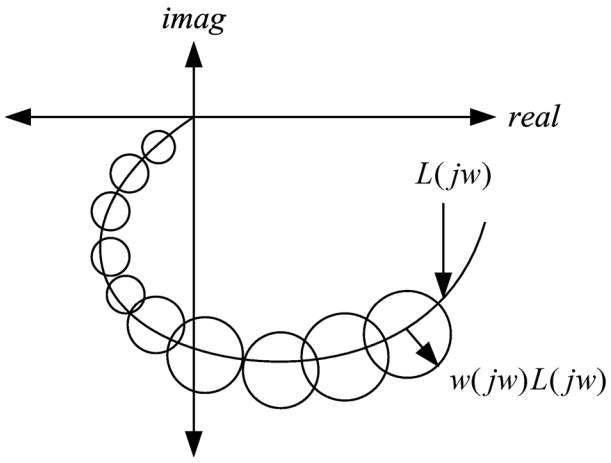

Figure 11: Nyquist diagram of multiplicative uncertainty

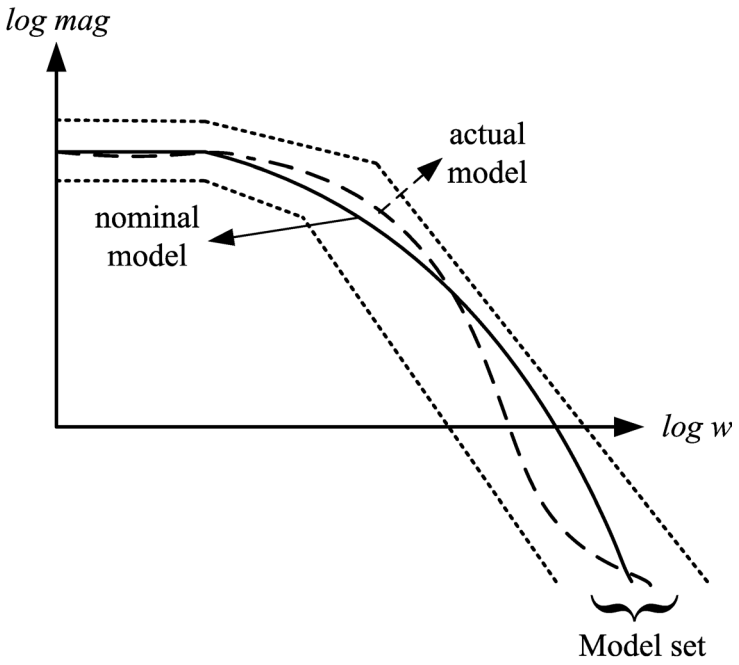

Figure 12: Multiplicative uncertainty effect

Generally the low frequency dynamics of the plant is known well and at this region the uncertainty is low. As frequency increases, the uncertainty also increases. In Fig. 12, representation of this effect is given. This error type is very suitable for any physical system representation, so in this thesis, output multiplicative uncertainty is discussed.

One can denote the uncertainty model set by **Π**, and nominal model by $P \in \mathbf{\Pi}$. Also, some performance specification is considered while designing controller K. Then the closed loop system is said to have [12, 13]:

Nominal Stability (NS): if K internally stabilizes the nominal plant P.

Robust Stability (RS): if K internally stabilizes every plant in set **Π**.

Nominal Performance (NP): if the performance objectives are satisfied for the nominal plant P.

Robust Performance (RP): if the performance objectives are satisfied for every plant in set **Π**.

One can easily check the nominal stability and nominal performance criteria; however, robust stability and robust performance require more analysis.

2.4.2. Small Gain Theorem

This section is devoted to check the robust stability of a nominally stable system. When the closed loop system has unstructured perturbations, the closed loop system can be modified to $M\Delta$ loop as given in Fig. 13 where M is stable transfer matrix.

Small Gain Theorem: Suppose $M \in \mathcal{RH}_\infty$, $\gamma > 0$. Then the system in Fig. 13 is internally stable for all $\Delta(s) \in \mathcal{RH}_\infty$ if one of the below conditions (i-ii) hold [12].

(i) $\|\Delta\|_\infty \le \frac{1}{\gamma}$ if and only if $\|M(s)\|_\infty < \gamma$

(ii) $\|\Delta\|_\infty < \frac{1}{\gamma}$ if and only if $\|M(s)\|_\infty \le \gamma$

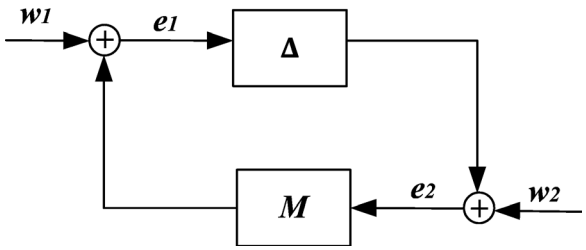

Figure 13: $M\Delta$ loop for stability analysis

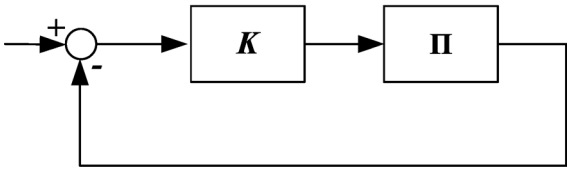

Figure 14: Robust stability analysis with unstructured uncertainties

2.4.3. Stability under Unstructured Uncertainties

Small gain theorem defined in previous section, assumes stable modeling error Δ and stable nominally stable system. Δ is weighted by matrices and uncertainty is represented as $\Delta(s)W_1(s)$.

The structure given in Fig. 14 is internally stable if the transfer matrix expressed with Eq. (2.68) is in $\mathcal{RH}_\infty$ for all $\forall \Pi \in \mathbf{\Pi}$.

$$\begin{bmatrix} I & K \\ -\Pi & I \end{bmatrix}^{-1} = \begin{bmatrix} (I+K\Pi)^{-1} & -K(I+\Pi K)^{-1} \\ \Pi(I+K\Pi)^{-1} & (I+\Pi K)^{-1} \end{bmatrix} \tag{2.68}$$

2.4.3.1. Additive Uncertainty Case

Additive uncertainty set can be represented as Eq. (2.69) where $\|\Delta\|_\infty < 1$ and Δ and $W_1 \in \mathcal{RH}_\infty$ are satisfied.

$$\mathbf{\Pi} = P + \Delta W_1 \tag{2.69}$$

If the nominal stability is available, robust stability is satisfied if Eq. (2.70) is satisfied [12].

$$\|W_1 K S_o\|_\infty < 1 \tag{2.70}$$

2.4.3.2. Output Multiplicative Uncertainty Case

Output multiplicative uncertainty set can be represented as Eq. (2.71) where $\|\Delta\|_\infty < 1$ and Δ and $W_1 \in \mathcal{RH}_\infty$ are satisfied.

$$\mathbf{\Pi} = (I + \Delta W_1) P \tag{2.71}$$

If the nominal stability is available, robust stability is satisfied if Eq. (2.72) is satisfied [12].

$$\|W_1 T_o\|_\infty < 1 \tag{2.72}$$

In this thesis, the perturbation is given as output multiplicative uncertainty as depicted in Fig. 15.

2.4.4. Robust Performance

Consider the feedback structure given in Fig. 15. The performance criterion can be modeled as to keep the worst case energy of the error *e* as small as possible in the existence of disturbance $\tilde{d}$ of unit energy. In a similar way, one would like to minimize the magnitude error under sinusoidal disturbance $\tilde{d}$.

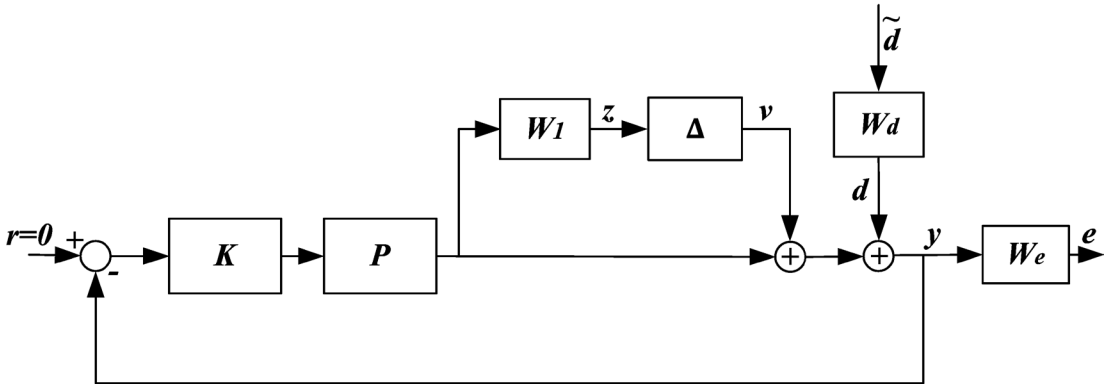

Figure 15: Output multiplicative perturbed system

So, in either case as given in Table 1, it is desired that the transfer function from $\tilde{d}$ to e $\left\|T_{e\tilde{d}}\right\|_\infty$ is small.

Assuming the system in Fig. 15 is robustly stable, the robust performance is obtained if Eq. (2.73) is satisfied, where $T_{e\tilde{d}} = W_e\left(I + P_\Delta K\right)^{-1} W_d$, $\forall P_\Delta \in \mathbf{\Pi}$.

$$\left\|T_{e\tilde{d}}\right\|_\infty \le 1 \tag{2.73}$$

More specifically, for each frequency w if Eq. (2.74) is satisfied, the robust performance is guaranteed [12].

$$\bar{\sigma}\left(W_d\right)\bar{\sigma}\left(W_e S_o\right) + \bar{\sigma}\left(W_1 T_o\right) \le 1, \forall w \tag{2.74}$$

2.5. Linear Fractional Transformation

In linear robust control theory, $\mathcal{H}_2$ and $\mathcal{H}_\infty$ control problems are treated in linear fractional transformation (LFT) structure. Moreover, when applying μ-analysis and synthesis, the use of LFT structure is essential.

In LQG/LTR control LFT usage is not a must; however, the equivalent representation of this problem in LFT framework is also discussed in Chapter 3.

There are two types of LFT, namely upper and lower. Assume M is complex matrix and it is partitioned as Eq. (2.75). Similarly, assume $\Delta_\ell \in \mathbb{C}^{q_2 x p_2}$ and $\Delta_u \in \mathbb{C}^{q_1 x p_1}$ are the complex matrices.

$$M = \begin{bmatrix} M_{11} & M_{12} \\ M_{21} & M_{22} \end{bmatrix} \in \mathbb{C}^{(p_1+p_2)x(q_1+q_2)} \tag{2.75}$$

Then the lower LFT is defined as in Eq. (2.76), and it is the transformation obtained by closing the lower loop in Fig. 16.

$$\mathcal{F}_\ell\left(M,\Delta_\ell\right) := M_{11} + M_{12}\Delta_\ell\left(I - M_{22}\Delta_\ell\right)^{-1} M_{21} \tag{2.76}$$

$\mathcal{F}_\ell\left(M,\Delta_\ell\right)$ is simply the closed loop transfer function from w_1 to e_1. It is the addition of nominal mappings M_{11} of the system and its perturbation due to some Δ.

On the other hand, the upper LFT is defined as Eq. (2.77), and it is the transformation obtained by closing the upper loop in Fig. 17.

$$\mathcal{F}_u\left(M,\Delta_u\right) := M_{22} + M_{21}\Delta_u\left(I - M_{11}\Delta_u\right)^{-1} M_{12} \tag{2.77}$$

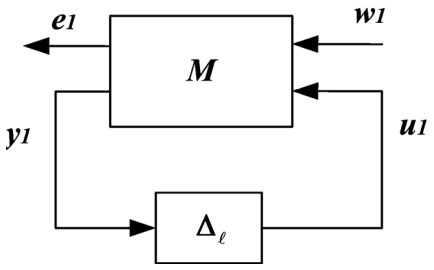

Figure 16: Lower LFT

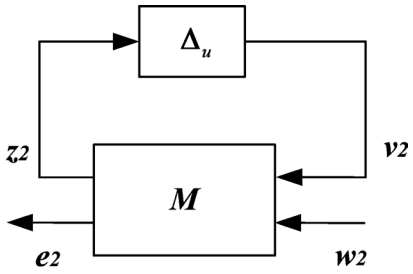

Figure 17: Upper LFT

$\mathcal{F}_u\left(M,\Delta_u\right)$ is the closed loop transfer function from w_2 to e_2. Generally, this transform is used for analysis of robust stability and performance [12].

2.6. μ and μ-synthesis

Robust stability and performance derived in Section 2.4, depend on the uncertainty descriptions and performance. In other words, according to selection of uncertainty description, the robust stability and robust performance conditions change. For example, Eqs. (2.72) and (2.74) are the conditions of robust stability and robust performance for output multiplicative perturbation and for the structure given in Fig. 15. Moreover, the results of the Section 2.4 are applicable only if there is a single uncertainty in the loop. When there is more than one uncertainty in the loop, all the perturbations must be reflected to the same point in the loop in order to use the singular value tests discussed earlier. However, this is usually a complicated procedure and it is not preferred. So, in this section, robust stability and robust performance tests are explained in μ framework using the LFT structure given in Fig. 18.

2.6.1. General Framework for System Robustness

It is usually possible to represent any system in the general framework given in Fig. 18 by making required modifications.

In Fig. 18, P is the interconnection matrix, K is the controller and Δ is all possible perturbations. The signal w is a vector which may include references, disturbances, and noises and e is a vector which includes error signals to be minimized. Finally, u and y are the control and measurement signals, respectively.

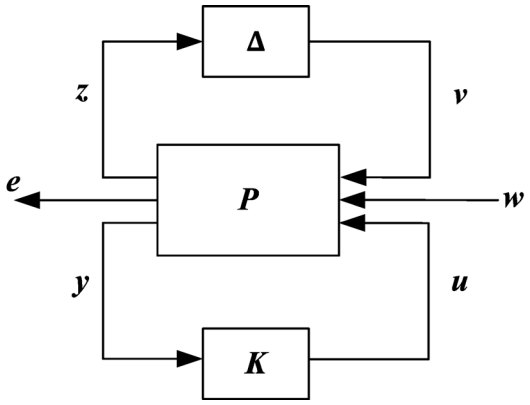

Figure 18: General framework

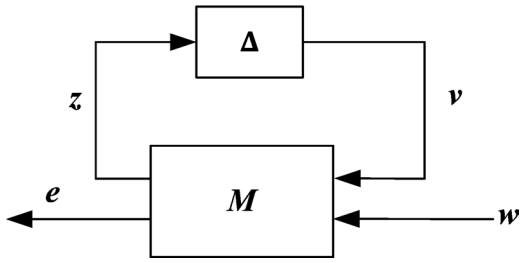

Figure 19: $M\Delta$ analysis framework

The robustness analysis is done in $M\Delta$ structure as given in Fig. 19 by closing the lower loop in Fig. 18. The lower LFT M is partitioned as Eq. (2.78).

$$M(s) = \mathcal{F}_\ell\left(P(s), K(s)\right) = \begin{bmatrix} M_{11}(s) & M_{12}(s) \\ M_{21}(s) & M_{22}(s) \end{bmatrix} \tag{2.78}$$

Then the upper LFT of $M\Delta$ gives a transfer matrix from w to e as given by Eq. (2.79).

$$e = \mathcal{F}_u\left(M, \Delta_\ell\right) w = \left[M_{22} + M_{21}\Delta_u \left(I - M_{11}\Delta_u\right)^{-1} M_{12} \right] w \tag{2.79}$$

2.6.2. Structured Singular Value

2.6.2.1. Definition of μ

The definition of the structural singular value (μ) results from the need to answer the following question. Given a matrix $M \in \mathbb{C}^{p x q}$ what is the smallest perturbation matrix $\Delta \in \mathbb{C}^{q x p}$ $\left(\text{in terms of maximum singular value } \bar{\sigma}(\Delta)\right)$ such that $\det\left(I - M\Delta\right) = 0$ is satisfied? In other words, one is interested in finding the smallest maximum singular value of the perturbation block that makes the corresponding determinant zero as given by Eq. (2.80).

$$a_{min} := \inf\left\{ \bar{\sigma}(\Delta) : \det\left(I - M\Delta\right) = 0,\ \Delta \in \mathbb{C}^{q x p} \right\} \tag{2.80}$$

The solution is given in [19] as the reciprocal of the maximum spectral radius of the matrix $M\Delta$ as shown in Eq. (2.81) for norm bounded perturbation.

$$a_{min} = \frac{1}{\max\limits_{\bar{\sigma}(\Delta) \le 1} \rho\left(M\Delta\right)} \tag{2.81}$$

For a complex perturbation $\Delta \in \mathbb{C}^{qxp}$, Eq. (2.82) is satisfied.

$$\max_{\bar{\sigma}(\Delta)\le 1} \rho(M\Delta) = \bar{\sigma}(M) \tag{2.82}$$

It is customary to define the maximum singular value of the matrix as in Eq. (2.83) which shows that the maximum singular value of a matrix is a measure of the smallest destabilizing perturbation matrix.

$$\bar{\sigma}(M) := \frac{1}{\inf\left\{\bar{\sigma}(\Delta) : \det(I - M\Delta) = 0,\ \Delta \in \mathbb{C}^{qxp}\right\}} \tag{2.83}$$

The uncertainty $\Delta \in \mathbb{C}^{qxp}$ is not restricted in any sense. Now, the same question with different uncertainty is considered. Consider a structurally restricted perturbation block having repeated scalars and full blocks. Let S is the number of scalar blocks and r_i is the dimension of them. Also, let F is the number of the full blocks and m_j is the dimensions of them. Perturbation $\boldsymbol{\Delta} \in \mathbb{C}^{nxn}$ is defined as in Eq. (2.84), and it satisfies Eq. (2.85).

$$\boldsymbol{\Delta} = \left\{\text{diag}\left[\delta_1 I_{r1}, \ldots, \delta_S I_{rS}, \Delta_1, \ldots, \Delta_F\right] : \delta_i \in \mathbb{C},\ \Delta \in \mathbb{C}^{m_j x m_j}\right\} \tag{2.84}$$

$$\sum_{i=1}^{S} r_i + \sum_{j=1}^{F} m_j = n \tag{2.85}$$

Often, norm bounded subset of $\boldsymbol{\Delta}$ is needed. For that reason, new set as in Eq. (2.86) is introduced which covers the uncertainties in the unit closed ball.

$$\boldsymbol{B\Delta} = \left\{\Delta \in \boldsymbol{\Delta} : \bar{\sigma}(\Delta) \le 1\right\} \tag{2.86}$$

Now the previous question is asked for this new structure. Given a matrix $M \in \mathbb{C}^{pxq}$ what is the smallest perturbation matrix $\Delta \in \boldsymbol{\Delta}$ such that $\det(I - M\Delta) = 0$ is satisfied? That is, the variable can be expressed in Eq. (2.87).

$$a_{min} := \inf\left\{\bar{\sigma}(\Delta) : \det(I - M\Delta) = 0,\ \Delta \in \boldsymbol{\Delta}\right\} \tag{2.87}$$

Again, Eq. (2.88) is valid for norm bounded perturbations [12, 19].

$$a_{min} = \inf\left\{a : \det(I - aM\Delta) = 0,\ \Delta \in \boldsymbol{B\Delta}\right\} = \frac{1}{\max_{\Delta \in \boldsymbol{B\Delta}} \rho(M\Delta)} \tag{2.88}$$

Definition of the structured singular value comes from the definition shown in Eq. (2.87). Instead of dealing with the smallest perturbation, it is very helpful to deal with its reciprocal. So, $1/a_{min}$ is called a structured singular value and it is denoted by $\mu_{\boldsymbol{\Delta}}(M)$.

Definition: For $M \in \mathbb{C}^{nxn}$, $\mu_{\Delta}(M)$ is defined as Eq. (2.89).

$$\mu_{\Delta}(M) := \frac{1}{\inf\{\bar{\sigma}(\Delta) : \Delta \in \mathbf{\Delta}, \det(I - M\Delta) = 0\}} \tag{2.89}$$

If no $\Delta \in \mathbf{\Delta}$ can make $I - M\Delta$ singular, $\mu_{\Delta}(M)$ is accepted to be zero.

2.6.2.2. Upper and Lower Bounds for μ

It can be shown that when perturbation has one scalar full block $\mathbf{\Delta} = \{\delta I,\ \delta \in \mathbb{C}\}$ satisfying ($S = 1, F = 0, r_1 = n$), $\mu_{\mathbf{\Delta}}(M) = \rho(M)$ is satisfied.

Similarly, when perturbation has one complex full block $\mathbf{\Delta} = \mathbb{C}^{nxn}$ satisfying ($S = 0$, $F = 1, m_1 = n$), $\mu_{\mathbf{\Delta}}(M) = \bar{\sigma}(M)$ is satisfied.

One can drive the result given in Eq. (2.91), by considering the perturbation relations shown in Eq. (2.90) [19].

$$\{\delta I,\ \delta \in \mathbb{C}\} \le \mathbf{\Delta} \le \mathbb{C}^{nxn} \tag{2.90}$$

$$\rho(M) \le \mu_{\mathbf{\Delta}}(M) \le \bar{\sigma}(M) \tag{2.91}$$

Generally, the difference between the bounds is large, so this relation gives very little information for most of the cases.

2.6.2.3. Better Bounds for μ

While keeping structured singular value constant, it is possible to change the bounds. Consider any unitary matrix U with the same structure as Δ, and any matrix D which commutes with Δ. In other words, U and D have forms in Eqs. (2.92) and (2.93).

$$\boldsymbol{U} = \{U \in \mathbf{\Delta} : UU^* = I_n\} \tag{2.92}$$

$$\boldsymbol{D} = \{\mathrm{diag}[D_1, \ldots, D_S, d_1 I_{m1}, \ldots, d_{F-1} I_{m_{F-1}}, I_{m_F}] : D_i \in \mathbb{C}^{r_i x r_i}, D_i = D_i^* > 0,\ d_j \in \mathbb{R}, d_j > 0\} \tag{2.93}$$

So, for any matrix $\Delta \in \mathbf{\Delta}$, $U \in \boldsymbol{U}$, *and* $D \in \boldsymbol{D}$ the relations given in Eq. (2.94) are satisfied [19].

$$U^* \in \boldsymbol{U}\ ,\ U\Delta \in \mathbf{\Delta}\ ,\ D\Delta = \Delta D\ ,\ \Delta U \in \mathbf{\Delta}\ ,\ \bar{\sigma}(U\Delta) = \bar{\sigma}(\Delta U) = \bar{\sigma}(\Delta) \tag{2.94}$$

For all $D \in \boldsymbol{D}$ and $U \in \boldsymbol{U}$ Eq. (2.95) are satisfied [19]. In other words, the stability of the structures given in Figs. 20 and 21 are equivalent.

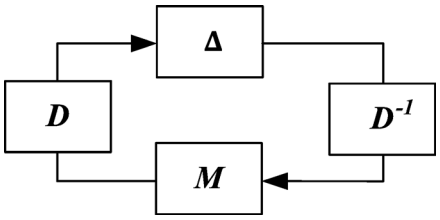

Figure 20: DMD^{-1} structure

$$\mu_{\Delta}(MU) = \mu_{\Delta}(UM) = \mu_{\Delta}(M) = \mu_{\Delta}\left(DMD^{-1}\right) \tag{2.95}$$

For that reason, the bounds discussed in Eq. (2.91) can be written as in Eq. (2.96) [19].

$$\max_{U \in \boldsymbol{U}} \rho(UM) \le \max_{\Delta \in \boldsymbol{B\Delta}} \rho(\Delta M) = \mu_{\Delta}(M) \le \inf_{D \in \boldsymbol{D}} \bar{\sigma}\left(DMD^{-1}\right) \tag{2.96}$$

The lower bound is not a convex problem. However, the upper bound can be formulated as a convex optimization problem, so the global minimum can be found [13, 15].

The convex optimization is not discussed in this thesis to keep the readers' attention to control methods applications instead of their solutions. In this aspect, the algorithms which are available in MATLAB are utilized [15].

The upper bound is not usually equal to μ. It is reported in [19] that equality is valid only for special cases as given in Eq. (2.97).

$$\mu_{\Delta}(M) = \inf_{D \in \boldsymbol{D}} \bar{\sigma}\left(DMD^{-1}\right) \text{ if } 2S + F \le 3 \tag{2.97}$$

In other words, the upper bound equality is satisfied if there are 3 or fewer blocks in $\boldsymbol{\Delta}$. For higher number of blocks, the upper bound and μ are close [13].

The upper bound can be thought as $\mathcal{H}_{\infty}$ norm of the scaled transfer function DMD^{-1}. And this idea leads to iterative μ-synthesis method known as *D-K* iteration.

2.6.3. Robust Stability

$M\Delta$ structure given in Fig. 21 is considered where $\Delta \in \boldsymbol{B\Delta}$ is a set of norm bounded block diagonal perturbations discussed in previous section. The interconnection is stable for all perturbations if and only if the condition given in Eq. (2.98) is satisfied for all frequencies.

$$\mu_{\Delta}\left(M(jw)\right) < 1, \forall w \tag{2.98}$$

2.6.4. Robust Performance

The robust performance can be tested by adding fictitious full block perturbation and constructing the new representation given in Fig. 22 where *M* is internally stable.

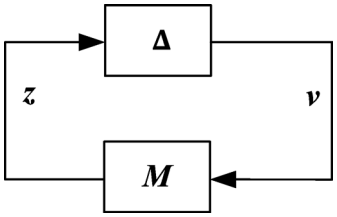

Figure 21: *M*Δ structure for stability

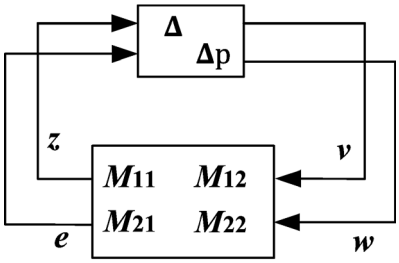

Figure 22: *M*Δ structure for performance

Robust performance is satisfied if and only if the μ of this new structure satisfies Eq. (2.99),

$$\mu_{\tilde{\Delta}}\left(M\right) < 1, \ \forall w \tag{2.99}$$

where $\tilde{\Delta} = \begin{bmatrix} \Delta & 0 \\ 0 & \Delta_p \end{bmatrix}$, $\Delta_p \in \mathbb{C}^{\dim(w)x\,dim(e)}$ is the new norm bounded perturbation block. This idea is the result of main loop theorem discussed in [19].

2.6.5. Summary of the μ-analysis

In the μ framework following stabilities and performances are valid if and only if the conditions given in Eqs. (2.100)-(2.103) are satisfied. *NS*, *NP*, *RS* and *RP* denote nominal stability, nominal performance, robust stability and robust performance, respectively [13].

$$NS \Leftrightarrow M \text{ is internally stable} \tag{2.100}$$

$$NP \Leftrightarrow \bar{\sigma}\left(M_{22}\right) = \mu_{\Delta_p} < 1, \ \forall w, \text{ and } NS \tag{2.101}$$

$$RS \Leftrightarrow \mu_{\Delta}\left(M_{11}\right) < 1, \forall w, \text{ and } NS \tag{2.102}$$

$$RP \Leftrightarrow \mu_{\tilde{\Delta}}\left(M\right) < 1, \forall w, \text{ and } NS \tag{2.103}$$

2.6.6. μ-synthesis and *D-K* iteration

The structured singular value μ is a very powerful tool when analyzing robust performance with given controller. However, the controller that minimizes a given μ condition is desired. The problem related with this condition is called as μ-synthesis problem [13].

2.6.6.1. *D-K* iteration

The direct solution of μ-synthesis problem is not available. However, for complex perturbations a method known as *D-K* iteration is available. It is a combination of $\mathcal{H}_\infty$ synthesis and μ-analysis. The aim is to find a controller that will minimize the peak value of μ by alternating between minimizing $\left\|DM(K)D^{-1}\right\|_\infty$ with respect to either *K* or *D*.

The objective of *D-K* iteration is given in Eq. (2.104) [13].

$$\min_{K}\left(\min_{D\in \boldsymbol{D}}\left\|DM(K)D^{-1}\right\|_\infty\right) \tag{2.104}$$

To start the iteration an initial stable $D(s)$ must be chosen. The identity matrix is often a good choice for starting point. Then the *D-K* iteration follows the steps 1 to 3.

Step 1: *K*-step: Synthesize a $\mathcal{H}_\infty$ controller for the scaled problem as shown in Fig. 23 with fixed $D(s)$.

Step 2: *D*-step: Find $D(jw)$ to minimize the $\bar{\sigma}(DMD^{-1})$ at each frequency with fixed *M* for the structure shown in Fig. 20 previously.

Step 3: Fit the magnitude of each element $D(jw)$ to a stable and minimum phase transfer function $D(s)$ and go step 1.

The iterations can continue until the μ bound becomes smaller than one or the bound is no longer decreases.

The controller obtained with *D-K* iteration has number of states equal to the total of nominal model, weights and twice the state number of $D(s)$.

2.7. Summary

In Chapter 2, the robust control theory is summarized. In the next chapters, the results derived in this chapter will be used. When analyzing the robustness of the designed controller, both the singular value tests and μ tests are used. The singular value tests are used by assuming the structure given in Fig. 15 is used. In other words, there is only one full uncertainty block in the system and performance is measured only by weighted output sensitivity. When different performance indices are added, the μ-analysis is used to investigate the robustness of the designed controller. The details are explained in the next chapters.

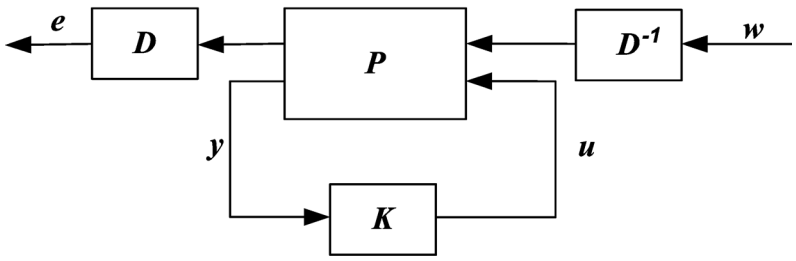

Figure 23: Scaled problem

CHAPTER 3

LQG/LTR, $\mathcal{H}_\infty$ AND μ CONTROLLERS DESIGN METHODS

In this part of the thesis, the control techniques that will be designed for LOS stabilization are examined. Firstly, linear quadratic Gaussian (LQG) problem is discussed. After discussing the LQG problem, the motivation behind loop transfer recovery (LTR) is examined. Loop transfer recovery is done using the loop shaping technique reported in [20]. Then $\mathcal{H}_2$ and $\mathcal{H}_\infty$ control problems are formulated and their state space solutions are discussed. Next, $\mathcal{H}_\infty$ mixed sensitivity control framework is examined. Finally, this chapter ends with the introduction of structures that will be used for μ-analysis and synthesis in Chapter 7.

3.1. LQG/LTR Control

In this section, the motivation behind the LQG/LTR method is explained. The mathematical background of the problem is given, and throughout the section [11] is used as a guide.

3.1.1. Traditional LQG Problem

In traditional LQG control, the plant is assumed to be LTI, and measurement noises and disturbance signals or model uncertainties (process noises) are stochastic with known statistical properties [11].

The state space model of the plant has the form given in Eq. (3.1),

$$\begin{aligned} \dot{x} &= Ax + Bu + \Gamma w_d \\ y &= Cx + w_n \end{aligned} \tag{3.1}$$

where w_d and w_n are uncorrelated zero mean white noise processes having constant power spectral densities W, V as shown in Eq. (3.2).

$$E\left\{w_d(t)w_d^T(\tau)\right\} = W\delta(t-\tau),\quad E\left\{w_n(t)w_n^T(\tau)\right\} = V\delta(t-\tau)$$
$$E\left\{w_d(t)w_n^T(\tau)\right\} = 0 \tag{3.2}$$

Then the problem boils down to finding a feedback law which minimizes the cost function illustrated in Eq. (3.3),

$$J = \lim_{T\to\infty} E\left\{\int_0^T \left(x^T Qx + u^T Ru\right)dt\right\} \tag{3.3}$$

where $Q = Q^T \geq 0$ and $R = R^T > 0$ are weighting matrices. The solution of this problem comes from separation principle as shown in Fig. 24. The procedure is as follows:

(1) Obtain an optimal estimate $\hat{x}$ of states x such that $E\left\{\left(x-\hat{x}\right)^T\left(x-\hat{x}\right)\right\}$ is minimized.

(2) Use estimate as if it were true state measurement and solve LQ regulator problem.

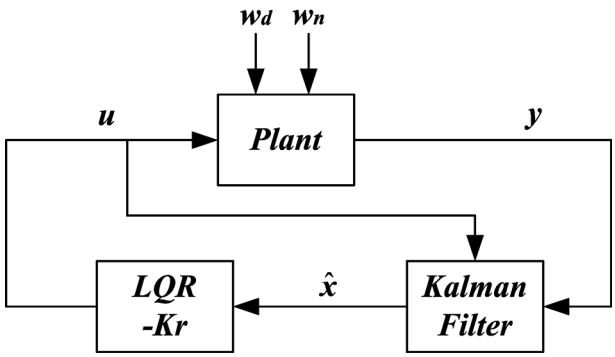

Figure 24: The separation theorem

Problem 1 is solved by estimating the states with a Kalman filter which has an observer structure in Eq. (3.4) with a special gain matrix K_f given by Eq. (3.5) [21].

$$\dot{\hat{x}} = A\hat{x} + Bu + K_f\left(y - C\hat{x}\right) \tag{3.4}$$

$$K_f = YC^T V^{-1} \tag{3.5}$$

In Eq. (3.5), Y is the positive definite symmetric matrix and it satisfies the algebraic Riccati equation (ARE) (3.6).

$$YA^T + AY - YC^T V^{-1} CY + \Gamma W \Gamma^T = 0 \tag{3.6}$$

Problem 2 is solved by finding an optimal control law for the deterministic LQ problem which minimizes the cost in Eq. (3.7).

$$J = \lim_{T\to\infty} E\left\{\int_0^T \left(x^T Qx + u^T Ru\right) dt\right\} \tag{3.7}$$

The solution of this problem turns out to be the linear function of the states as shown in Eq. (3.8) where K_r is given in Eq. (3.9).

$$u = -K_r x \tag{3.8}$$

$$K_r = R^{-1} B^T X \tag{3.9}$$

In Eq. (3.9), X is the positive definite symmetric matrix and satisfies the ARE (3.10).

$$A^T X + XA - XBR^{-1}B^T X + Q = 0 \tag{3.10}$$

3.1.2. LQG: Combined Optimal State Estimation and Optimal State Feedback

The transfer function from y to u as given in Fig. 25 is the LQG compensator transfer function, and its state space form is given in Eq. (3.11). The order of the compensator is the same as the order of the plant.

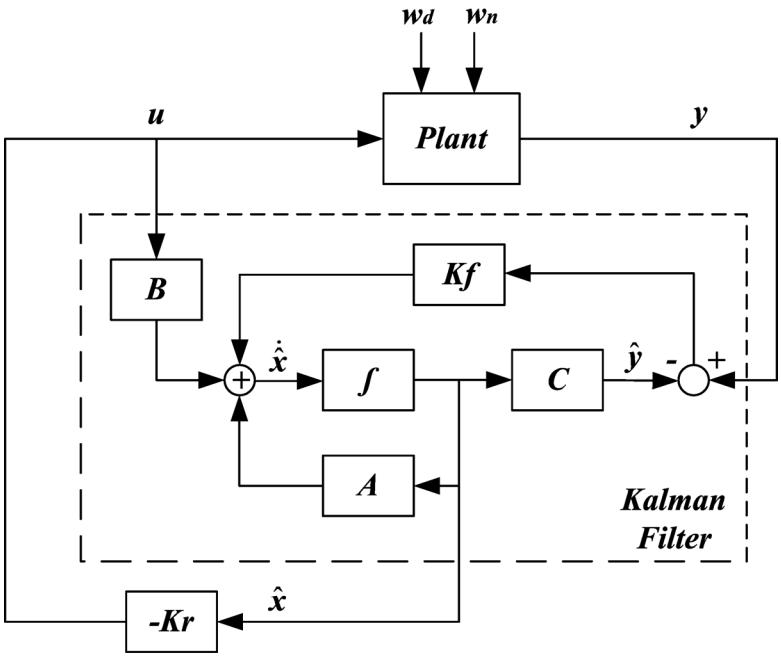

Figure 25: LQG control structure

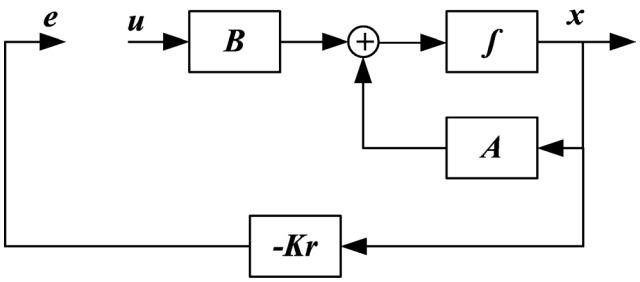

Figure 26: Full state feedback

$$K_{LQG}(\mathrm{s}) = \left[\begin{array}{c|c} A - BK_r - K_f C & K_f \\ \hline -K_r & 0 \end{array}\right] \tag{3.11}$$

In traditional LQG problem, K_r and K_f are exists if $(A, B, Q^{1/2})$ are stabilizable and $(A, \Gamma W^{1/2}, C)$ are detectable [11].

3.1.3. Performance and Robustness Properties of Optimal State Feedback

When all states of the plant are available or measurable, Kalman Filter is not required. To investigate the robustness, one can break the loop as shown in Fig. 26 so that the open loop transfer function can be obtained.

The open loop transfer matrix at the plant input is $-\frac{e}{u} = L_r(s) = K_r(sI - A)^{-1} B$.

Return difference at the plant input is $F_r(s) = I + K_r(sI - A)^{-1} B$.

After manipulating the ARE (3.10), Eq. (3.12) is satisfied [11].

$$F_r^T(-jw) R F_r(jw) \geq R \tag{3.12}$$

Taking $R = \rho I$, [11, 14, 22, 23] show that when the loop is perturbed by $W_\Delta(jw)$ the closed loop remains stable as long as $W_\Delta^T(-jw) + W_\Delta(jw) > I$ is satisfied. This leads to following results in classical control sense. When there is a pure gain perturbation in the loop, the closed loop system is stable as long as $W_\Delta(jw) > 1/2$ is satisfied. When only phase perturbation $W_\Delta(jw) = e^{j\theta}$ exists, the closed loop system remains stable when phase perturbation θ is less than 60°.

In brief, one can conclude that when R is diagonal the closed loop can tolerate gain variation between $(1/2, \infty)$ and phase variation less than 60° in each channel.

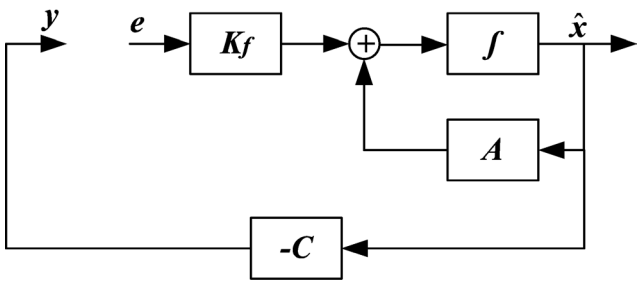

Figure 27: Kalman filter

3.1.4. Performance and Robustness Properties of Kalman Filter

To investigate the open loop transfer matrix of the Kalman filter it is convenient to assume control input to be zero since it affects both plant and Kalman filter in the same way. Then consider Fig. 27 for transfer matrix derivation.

The open loop transfer matrix at the plant output is $-\frac{y}{e} = L_f(s) = C(sI - A)^{-1} K_f$.

Return difference at the plant output is $F_f(s) = I + C(sI - A)^{-1} K_f$.

Similarly, after manipulating the ARE (3.6), $F_f(s) V F_f^T(-s) \geq V$ is obtained [11, 14, 22, 23]. So, Kalman filter loop is also stable under gain variation between $(1/2, \infty)$ and phase variation less than 60° in each channel.

3.1.5. Loop Transfer Recovery

Considering the fact that Kalman filter and state feedback have good robustness and performance properties, one may consider that LQG compensator has generally yield good robustness and performance properties. However, in [24] it is reported that there is no guaranteed stability conditions for the loops with LQG regulators, and if the designers do not pay attention, they can obtain arbitrary poor stability margins.

The method introduced in [25] overcomes this drawback of LQG regulators. The method is a way of designing an optimal state feedback such that the Kalman filter properties are recovered at the plant output.

For the dual problem, special Kalman filter is designed such that the full state properties are obtained at the plant input. For these problems some of the full state feedback poles (or Kalman filter poles for dual case) are attracted by the zeros of the plant and the

remaining ones become arbitrary fast. So, this procedure works well for the minimum-phase plants [11].

Define G and Φ which satisfy Eqs. (3.13) and (3.14).

$$G = C\left(sI - A\right)^{-1} B \tag{3.13}$$

$$\Phi = \left(sI - A\right)^{-1} \tag{3.14}$$

There are two methods for the application of the loop recovery in a feedback loop.

Method 1: Recovery at plant output

Fact1: The open loop transfer matrix obtained by breaking the LQG loop at point 4 of Fig. 28 is the KF open loop transfer matrix $C\Phi K_f$. Since u acts the same way to system and KF, it is convenient to assume $u = 0$, $y = 0$.

Fact2: The open loop transfer matrix obtained by breaking the LQG loop at point 2 of Fig. 28 is GK_{LQG}. It can be made to approach $C\Phi K_f$ by using LTR procedure.

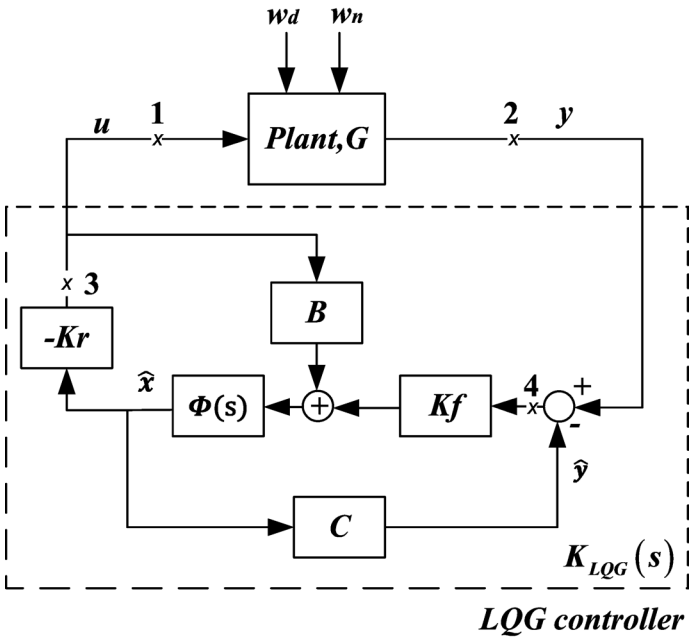

Figure 28: Loop recovery

Method 2: Recovery at plant input

Fact3: The open loop transfer matrix obtained by breaking the LQG loop at point 3 of Fig. 28 is the LQR open loop transfer matrix $K_r\Phi B$. In this analysis, it is convenient to assume state estimation error is zero.

Fact4: The open loop transfer matrix obtained by breaking the LQG loop at point 1 of Fig. 28 is $K_{LQG}G$. It can be made to approach $K_r\Phi B$ by using LTR procedure.

In this thesis the first method will be used.

LTR procedure at the plant output can be summarized in two steps [11, 25].

Step 1: Design a Kalman filter by adjusting the covariance matrices W and V such that a desired open loop transfer matrix $C\Phi K_f$ is obtained.

Step 2: Design an optimal state feedback regulator by setting $Q = I$ and $R = \rho I$ and reduce ρ until the open loop transfer matrix at the output of the plant has converged sufficiently to $C\Phi K_f$ over frequency range of interest.

Now how to obtain a good $C\Phi K_f$ will be discussed [11].

3.1.6. Shaping Singular Values

To design a satisfactory open loop transfer matrix, one needs to modify W and V in the first LTR method. Moreover, one can also use frequency dependent weighting matrices $W(s)$ and $V(s)$ to obtain a good properties of $C\Phi K_f$.

Now assume that instead of state disturbances the plant has a disturbance d having power spectral density $D(s)$ and measurement noise v having power spectral density $V(s)$ as shown in Fig. 29. Further assume that disturbance d and measurement noise v are created from the processes given in Eqs. (3.15) and (3.16), respectively,

$$\begin{aligned} \dot{\xi} &= A_d\xi + B_d\tilde{d} \\ d &= C_d\xi \end{aligned} \tag{3.15}$$

$$\begin{aligned} \dot{\eta} &= A_v\eta + B_v\tilde{v} \\ v &= C_v\eta + \theta \end{aligned} \tag{3.16}$$

where $\tilde{d}$, $\tilde{v}$ and θ are white noise processes. Combining these with original plant representation in Eq. (3.1), one can obtain the augmented system shown in Eq. (3.17).

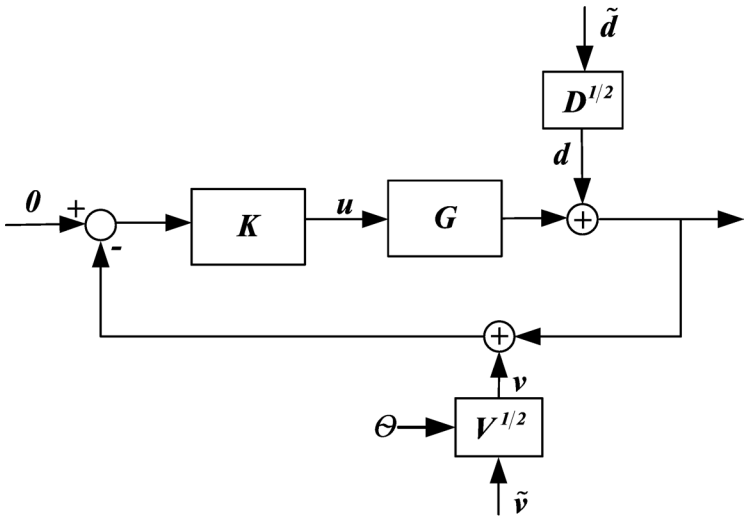

Figure 29: Augmentation of plant

$$\begin{bmatrix}\dot{x}\\ \dot{\xi}\\ \dot{\eta}\end{bmatrix}=\begin{bmatrix}A & 0 & 0\\ 0 & A_d & 0\\ 0 & 0 & A_v\end{bmatrix}\begin{bmatrix}x\\ \xi\\ \eta\end{bmatrix}+\begin{bmatrix}B\\ 0\\ 0\end{bmatrix}u+\begin{bmatrix}0 & 0\\ B_d & 0\\ 0 & B_v\end{bmatrix}\begin{bmatrix}\tilde{d}\\ \tilde{v}\end{bmatrix}$$

$$y=\begin{bmatrix}C & C_d & C_v\end{bmatrix}\begin{bmatrix}x\\ \xi\\ \eta\end{bmatrix}+\theta \tag{3.17}$$

$$z=\begin{bmatrix}C & C_d & C_v\end{bmatrix}\begin{bmatrix}x\\ \xi\\ \eta\end{bmatrix}$$

After augmenting the plant, the problem is still solvable by LQG framework by assuming Eq. (3.18) is satisfied.

$$E\left\{\theta\theta^T\right\}>0,\ E\left\{\theta\tilde{v}^T\right\}=0,\ E\left\{\theta\tilde{d}^T\right\}=0 \tag{3.18}$$

Define $Z(w)$, $U(w)$ to denote the power spectral densities of the signals z and u respectively. Then the cost function can be written as in Eq. (3.19) as discussed in [11],

$$J=E\left\{\left(z^TQz+u^TRu\right)\right\}=\frac{1}{2\pi}\int_{-\infty}^{\infty}\left\{\text{trace}\left[QZ(w)\right]+\text{trace}\left[RU(w)\right]\right\}dw \tag{3.19}$$

where the signals z and u are given in Eqs. (3.20) and (3.21).

$$z = S_o d - T_o v \tag{3.20}$$

$$u = -KS_o d - KS_o v \tag{3.21}$$

The cost function in Eq. (3.19) can be written as Eq. (3.22) [11].

$$J = \frac{1}{2\pi}\int_{-\infty}^{\infty}\left\{\begin{array}{l}\sum_i \sigma^2\left[Q^{1/2}S_o(jw)D^{1/2}(jw)\right]+\sum_i \sigma^2\left[Q^{1/2}T_o(jw)V^{1/2}(jw)\right] \\ +\sum_i \sigma^2\left[R^{1/2}K(jw)S_o(jw)D^{1/2}(jw)\right]+\sum_i \sigma^2\left[R^{1/2}K(jw)S_o(jw)V^{1/2}(jw)\right]\end{array}\right\}dw \tag{3.22}$$

So, LQG problem minimizes the output sensitivity S_o, output complementary sensitivity T_o, and KS_o weighted by corresponding transfer matrices. It is reported in [20] that the cost of the LTR procedure approaches Eq. (3.23) by taking $Q = I$, $R = \rho I$ and reducing ρ.

$$\lim_{\rho\to 0} J_{LTR} = \frac{1}{2\pi}\int_{-\infty}^{\infty}\left\{\sum_i \sigma^2\left[S_o D^{1/2}(jw)\right]+\sum_i \sigma^2\left[T_o V^{1/2}(jw)\right]\right\}dw \tag{3.23}$$

One can see that LTR procedure applied at plant output trades off the output sensitivity $S_o(jw)$ against the output complementary sensitivity $T_o(jw)$ with a factor $W_e(jw) = D^{1/2}(jw)V^{-1/2}(jw)$. Assuming $V = I$ and choosing $D^{1/2}(jw)$ appropriately, it is possible to shape the sensitivity function over a required frequency range.

3.2. $\mathcal{H}_2$ and $\mathcal{H}_\infty$ Control

In this section, $\mathcal{H}_2$ and $\mathcal{H}_\infty$ control problems and their solutions are examined. In this section, the results and solutions discussed in [13] are followed.

The LFT structure for $\mathcal{H}_2$ and $\mathcal{H}_\infty$ control synthesis is given in Fig. 30 where P is the interconnection matrix and K is the controller. Signal w is a vector which may include references, disturbances, and noises and e is a vector which includes error signals to be minimized. Finally, u and y are the control and measurement signals respectively. The corresponding transfer matrix from (w, u) to (e, y) is given in Eq. (3.24).

$$\begin{bmatrix} e \\ y \end{bmatrix} = \begin{bmatrix} P_{11} & P_{12} \\ P_{21} & P_{22} \end{bmatrix}\begin{bmatrix} w \\ u \end{bmatrix} \tag{3.24}$$

The interconnection transfer matrix has a state space representation depicted in Eq. (3.25), and the lower LFT gives a transfer matrix from w to e ($e = \mathcal{F}_\ell(P, K)w$).

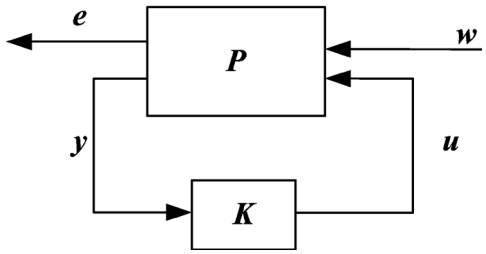

Figure 30: LFT for $\mathcal{H}_2$ and $\mathcal{H}_\infty$ control

$$P = \left[\begin{array}{c|cc} A & B_1 & B_2 \\ \hline C_1 & D_{11} & D_{12} \\ C_2 & D_{21} & D_{22} \end{array}\right] \tag{3.25}$$

$\mathcal{H}_2$ and $\mathcal{H}_\infty$ control minimizes the $\mathcal{H}_2$ and $\mathcal{H}_\infty$ norm of the $e = \mathcal{F}_\ell(P, K)w$ respectively.

$\mathcal{H}_2$ and $\mathcal{H}_\infty$ control problems are usually solved by state space techniques introduced in [26]. Both $\mathcal{H}_2$ and $\mathcal{H}_\infty$ control methods give a controller having same state dimension as augmented plant *P*. Both solutions are found by solving ARE equations and they both have separation principle as in the case of LQG control discussed in Section 3.1. The assumptions (A1) to (A5) are usually made for these problems [13].

$(\mathrm{A1})(A, B_2, C_2)$ is stabilizable and detectable.

$(\mathrm{A2})\, D_{12}$ and D_{21} have full rank.

$(\mathrm{A3})\begin{bmatrix} A - jwI & B_2 \\ C_1 & D_{12} \end{bmatrix}$ has full column rank for all *w*.

$(\mathrm{A4})\begin{bmatrix} A - jwI & B_1 \\ C_2 & D_{21} \end{bmatrix}$ has full row rank for all *w*.

$(\mathrm{A5})\, D_{11} = 0$ and $D_{22} = 0$.

(A1) is required for the existence of stabilizing controller *K*, and (A2) is required for *K* to be proper. (A3) and (A4) ensure that the controller does not try to cancel the poles or zeros on the imaginary axis which leads to instability. (A5) is required for $\mathcal{H}_2$ control. Making $D_{11} = 0$ leads to strictly proper P_{11} which is required, because $\mathcal{H}_2$ is the set where there are proper transfer matrices. $D_{22} = 0$ makes P_{22} strictly proper and simplifies the $\mathcal{H}_2$ problem. In $\mathcal{H}_\infty$ control, none of them is required but if they are available they simplify

the problem. Sometimes additional assumptions can be made to simplify the solutions greatly [13].

(A6) $D_{12}{}^{T}C_1 = 0$ and $B_1 D_{21}{}^{T} = 0$.

$(\text{A7})\, D_{12} = \begin{bmatrix} 0 \\ I \end{bmatrix}$ and $D_{21} = \begin{bmatrix} 0 & I \end{bmatrix}$.

$(\text{A8})(A, B_1)$ is stabilizable and (A, C_1) is detectable.

(A6) is required for $\mathcal{H}_2$ problem and it means that there is no cross term in cost function. As an example in LQG framework, it is equal to uncorrelated measurement and process noise.

3.2.1. $\mathcal{H}_2$ Optimal Control

The standard $\mathcal{H}_2$ optimal control results in a controller which minimizes the norm $\left\| \mathcal{F}_\ell (P, K) \right\|_2$. In this thesis, $\mathcal{H}_2$ optimal control will be discussed in LQG framework.

LQG: A Special $\mathcal{H}_2$ Optimal Control:

The traditional LQG problem is discussed in Section 3.1. For completeness, it is reconsidered in $\mathcal{H}_2$ framework. The plant has the state space representation in Eq. (3.26),

$$\begin{aligned} \dot{x} &= Ax + Bu + \Gamma w_d \\ y &= Cx + w_n \end{aligned} \tag{3.26}$$

where w_d and w_n are uncorrelated zero mean white noise processes having constant power spectral densities W, V satisfying Eq. (3.27).

$$E\left\{ \begin{bmatrix} w_d(t) \\ w_n(t) \end{bmatrix} \begin{bmatrix} w_d^T(\tau) & w_n^T(\tau) \end{bmatrix} \right\} = \begin{bmatrix} W & 0 \\ 0 & V \end{bmatrix} \tag{3.27}$$

The aim of the LQG problem is to find a controller K such that the cost in Eq. (3.28) is minimized. Moreover, the error signals and disturbance signals are obtained in Eqs. (3.29) and (3.30), where w is a vector of zero mean unit intensity white noise.

$$J = \lim_{T \to \infty} E\left\{ \int_0^T \left(x^T Q x + u^T R u \right) dt \right\} \tag{3.28}$$

$$e = \begin{bmatrix} Q^{1/2} & 0 \\ 0 & R^{1/2} \end{bmatrix} \begin{bmatrix} x \\ u \end{bmatrix} \tag{3.29}$$

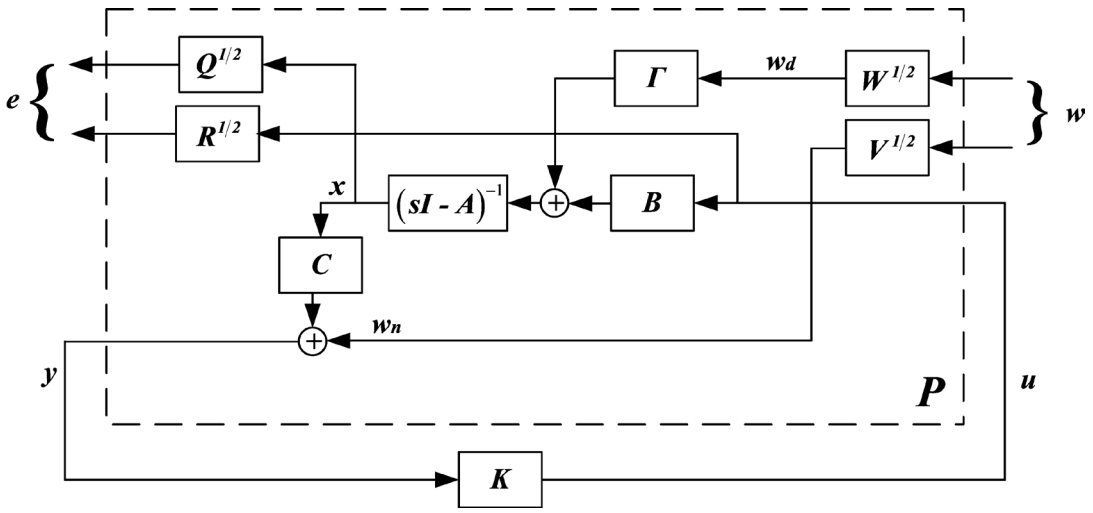

Figure 31: LQG problem in LFT structure

$$\begin{bmatrix} w_d \\ w_n \end{bmatrix} = \begin{bmatrix} W^{1/2} & 0 \\ 0 & V^{1/2} \end{bmatrix} w \tag{3.30}$$

After all this reformulations, the LQG cost given in Eq. (3.28) is equated to $\left\| F_l(P,K) \right\|_2^2$ where $F_l(P,K)$ is the transfer matrix from *w* to *e*. Then the state space representation of generalized plant for this problem is given in Eq. (3.31).

$$P = \left[\begin{array}{c|cc:c} A & \Gamma W^{1/2} & 0 & B \\ \hline Q^{1/2} & 0 & 0 & 0 \\ 0 & 0 & 0 & R^{1/2} \\ \hdashline C & 0 & V^{1/2} & 0 \end{array}\right] \tag{3.31}$$

The traditional LQG problem can be given in LFT framework as in Fig. 31. Therefore, the LQG problem is a special type of $\mathcal{H}_2$ problem, and in this thesis $\mathcal{H}_2$ design will be made in LQG framework while designing controller in Chapter 7.

3.2.2. $\mathcal{H}_\infty$ Optimal Control

The standard $\mathcal{H}_\infty$ problem seeks a controller *K* that will minimize the transfer matrix from *w* to *e*. The cost for this problem is given in Eq. (3.32).

$$\left\| F_l(P,K) \right\|_\infty = \max_w \bar{\sigma}\left(F_l(P,K)(jw) \right) \tag{3.32}$$

In practice it is usually not necessary to obtain optimal solution, for easiness it is desired to obtain suboptimal controller which is very close to optimal solution. Let the optimal solution of the $\mathcal{H}_\infty$ problem be γ_{min}.

$\mathcal{H}_\infty$ Suboptimal Control:

Finding a controller K satisfying $\left\|\mathcal{F}_\ell\left(P,K\right)\right\|_\infty < \gamma$ where $\gamma > \gamma_{min}$ is the formulation of suboptimal controller.

The solution of this problem can be found by using the technique discussed in [26]. It is an iterative algorithm that finds the suboptimal controller that makes γ and γ_{min} close within specified tolerances.

General $\mathcal{H}_\infty$ Algorithm:

If assumptions (A1) to (A8) are hold, there exist a stabilizing controller $K(s)$ such that $\left\|\mathcal{F}_\ell\left(P,K\right)\right\|_\infty < \gamma$ if and only if conditions (i-iii) are satisfied [13].

(i) $X_\infty \geq 0$ is a solution to the algebraic Riccati equation depicted in Eq. (3.33) such that $Re\,\lambda_i\left[A + \left(\gamma^{-2}B_1B_1^T - B_2B_2^T\right)X_\infty\right] < 0,\ \forall i$ and;

$$A^T X_\infty + X_\infty A + C_1^T C_1 + X_\infty\left(\gamma^{-2}B_1B_1^T - B_2B_2^T\right)X_\infty = 0 \tag{3.33}$$

(ii) $Y_\infty \geq 0$ is a solution to the algebraic Riccati equation shown in Eq. (3.34) such that $Re\,\lambda_i\left[A + Y_\infty\left(\gamma^{-2}C_1^T C_1 - C_2^T C_2\right)\right] < 0, \forall i$ and;

$$AY_\infty + Y_\infty A^T + B_1B_1^T + Y_\infty\left(\gamma^{-2}C_1^T C_1 - C_2^T C_2\right)Y_\infty = 0 \tag{3.34}$$

(iii) $\rho(X_\infty Y_\infty) < \gamma^2$

Then the controller is obtained using the results of Eq. (3.35), and controller transfer matrix is given in Eq. (3.36).

$$\begin{gathered} F_\infty = -B_2^T X_\infty\ ,\ L_\infty = -Y_\infty C_2^T\ ,\ Z_\infty = \left(I - \gamma^2 Y_\infty X_\infty\right)^{-1} \\ A_\infty = A + \gamma^{-2}B_1B_1^T X_\infty + B_2F_\infty + Z_\infty L_\infty C_2 \end{gathered} \tag{3.35}$$

$$K\left(s\right) = -Z_\infty L_\infty\left(sI - A_\infty\right)^{-1}F_\infty \tag{3.36}$$

The controller can be written as combination of observer and state feedback as seen in Eq. (3.37),

$$\dot{\hat{x}} = A\hat{x} + B_1\gamma^{-2}B_1^T X_\infty\hat{x} + B_2u + Z_\infty L_\infty\left(C_2\hat{x} - y\right) \tag{3.37}$$

where $u = F_\infty \hat{x}$. Moreover, the term $\gamma^{-2} B_1^T X_\infty \hat{x}$ can be viewed as a worst case disturbance $\hat{w}_{worst}$. Then the structure of observer differs from Kalman filter by worst case disturbance estimation [13, 26]. In brief, like $\mathcal{H}_2$ control, for $\mathcal{H}_\infty$ control, there is also separation principle idea.

As discussed previously the solution of the $\mathcal{H}_\infty$ control problem is obtained by iterative process by solving Eqs. (3.33) and (3.34), testing conditions (i)-(iii) and changing γ at the same time [13, 26].

In conclusion, solution of $\mathcal{H}_\infty$ control problem requires complex and iterative method. On the other hand, $\mathcal{H}_2$ problem is fairly easy and the controller can be found from the solution of just two Riccati equations [13].

3.2.3. Mixed Sensitivity $\mathcal{H}_\infty$ Control

Mixed sensitivity is the name of the problem where sensitivity $S_o = \left(I + GK\right)^{-1}$ is shaped with one or two of the other transfer matrices $T_o = I - S_o$ and KS_o. As explained in Chapter 2, the disturbance rejection typically requires low sensitivity in low frequencies. Moreover, the effect of *d* to *u* is given by transfer matrix KS_o, and usually it is desired to limit the controller bandwidth so that disturbances are not amplified at control signals. Also, robust stability under additive perturbation puts limit to KS_o. In addition, T_o shaping is required for noise attenuation and robust stability under output multiplicative perturbations. In these aspects, $\mathcal{H}_\infty$ control design is made in mixed sensitivity framework. For this problem the cost function given by Eq. (3.38) can be used. The corresponding augmented plant and LFT structure is given in Fig. 32.

$$\left\| \begin{bmatrix} W_e S_o \\ W_u K S_o \\ W_t T_o \end{bmatrix} \right\|_\infty \tag{3.38}$$

Please observe that the aim of $\mathcal{H}_\infty$ control is to minimize Eq. (3.38) to satisfy the nominal performance. For this structure it is possible to give generalized plant *P* as in Eq. (3.39).

$$P = \left[\begin{array}{c|c} W_e & W_e G \\ 0 & -W_u \\ 0 & -W_t G \\ \hline -I & -G \end{array}\right] \tag{3.39}$$

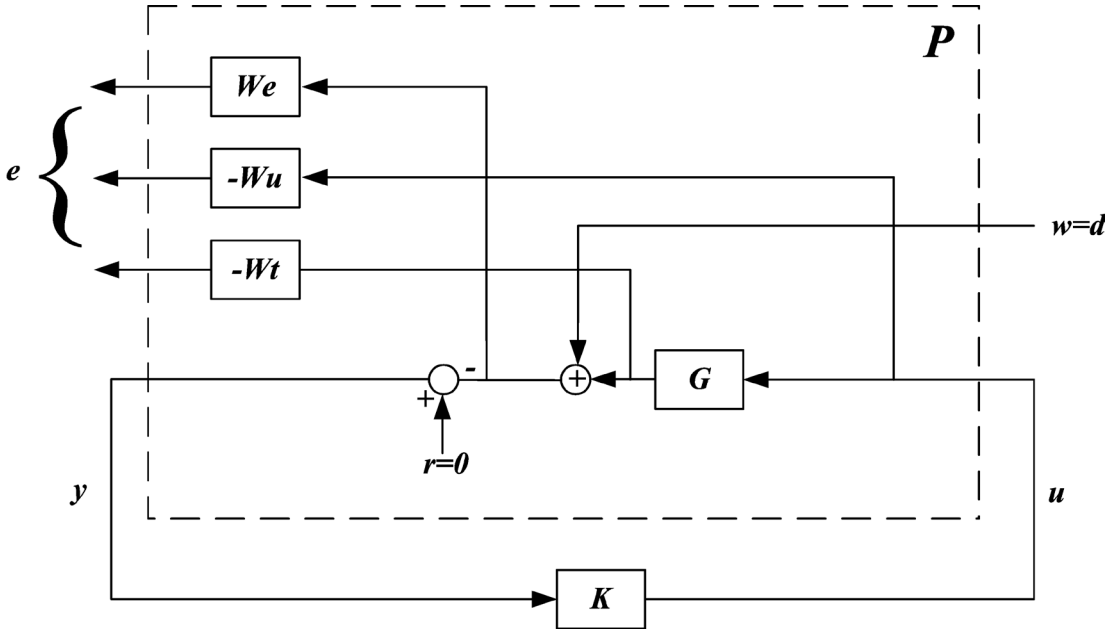

Figure 32: *S*/*KS*/*T* mixed sensitivity in regulation mode

3.3. μ-synthesis

For μ-synthesis design the robustness is gained by *D*-*K* iteration as discussed previously. In this aspect, there is no performance index related with the complementary sensitivity *T* required in the cost given by Eq. (3.40).

$$\left\| \begin{bmatrix} W_e S_o \\ W_u K S_o \end{bmatrix} \right\|_\infty \tag{3.40}$$

The aim of the μ-synthesis is to minimize Eq. (3.40) for all models in the set Δ to satisfy robust performance, which is not present in the $\mathcal{H}_\infty$ design. However, in $\mathcal{H}_\infty$ design careful selection of weight W_t may also lead to a robust controller which minimizes the performance index given by Eq. (3.40) for all models.

For this problem, the closed loop interconnection structure is given in Fig. 33. The generalized plant for this structure can be given as Eq. (3.41).

$$P = \left[\begin{array}{c|c|c} 0 & 0 & W_p G \\ \hline W_e & W_e & W_e G \\ \hline 0 & 0 & -W_u \\ \hline -I & -I & -G \end{array}\right] \tag{3.41}$$

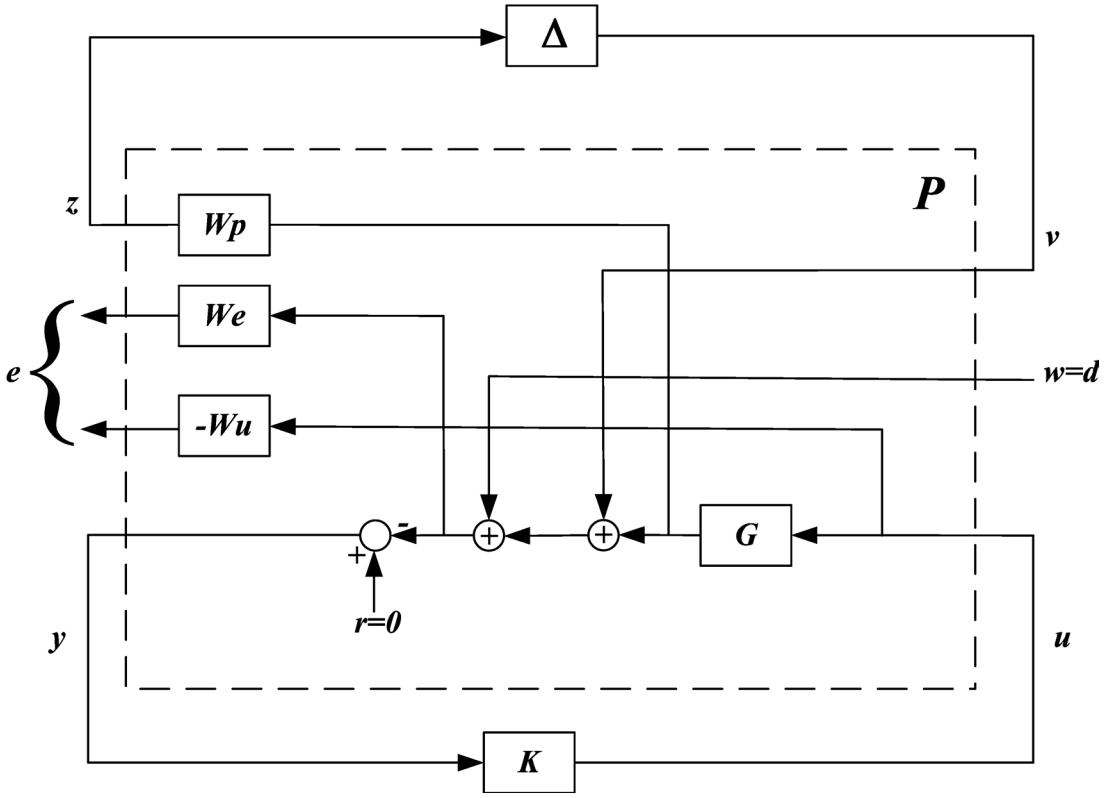

Figure 33: Closed loop interconnection

As discussed in Chapter 2, the structure given in Fig. 33 needs to be modified to analyze the robust performance of the closed loop system. Therefore, when making *D-K* iterations, the LFT structures given in Figs. 34 and 35 are used.

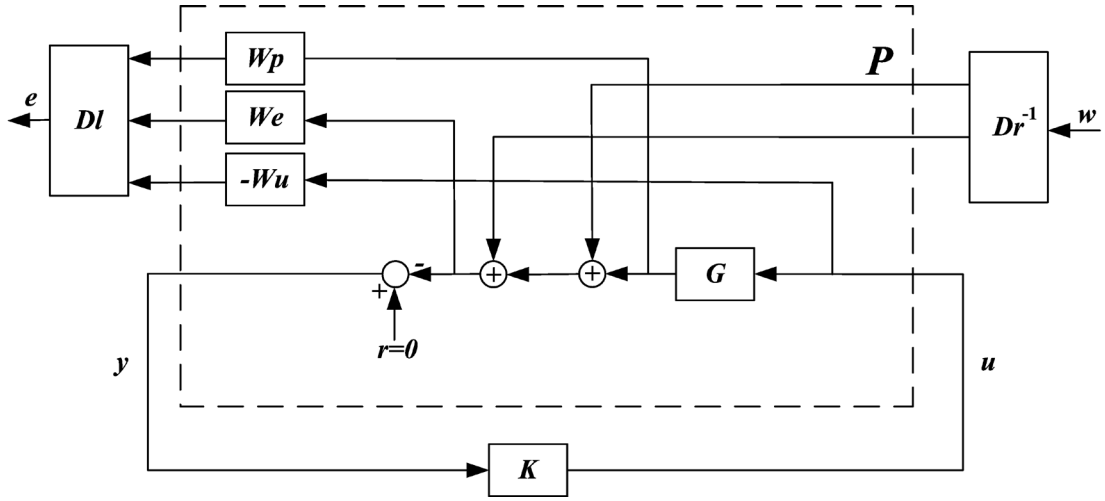

Figure 34: LFT structure for scaled problem (*K*-step)

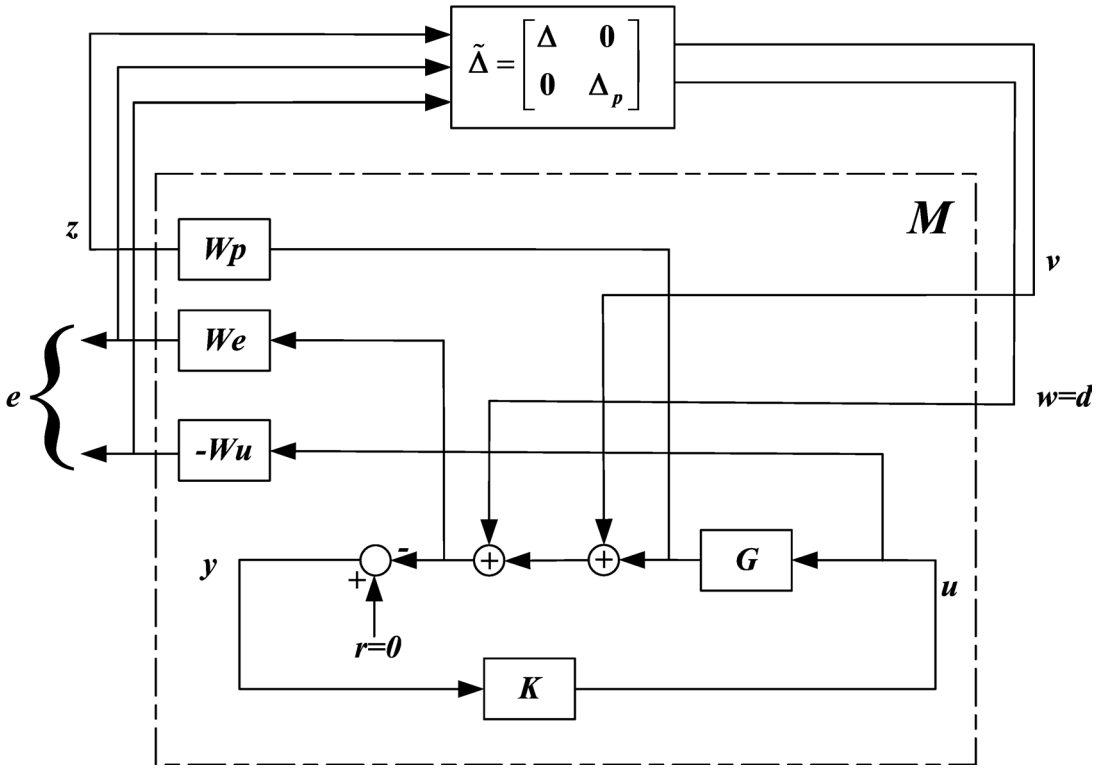

Figure 35: LFT structure for μ-analysis (*D*-step)

3.4. Summary

In Chapter 3, the LQG/LTR, $\mathcal{H}_2$ and $\mathcal{H}_\infty$ control problems and their solution methods are discussed. In this thesis, the solutions of these problems are found using the build in functions available in MATLAB. Moreover, the control methods that will be used in Chapter 7 for LOS controller design are expressed in detail.

In Section 3.1, the LQG/LTR design that uses the loop shaping idea is given. In Section 3.2, the $\mathcal{H}_\infty$ mixed sensitivity design is explained. In Section 3.3, the structures that are used for μ-analysis and synthesis are illustrated. In short, these three techniques and structures will be used at controllers design stage in Chapter 7.

CHAPTER 4

EXPERIMENTAL SETUP

The stabilization servo loop includes gimbal, motor, current amplifier, controller and gyro as discussed previously. In this chapter, these components are briefly introduced and the experimental setup that is used in algorithm evaluations is illustrated.

4.1. Overall System

The block diagram of the overall system is depicted in Fig. 36.

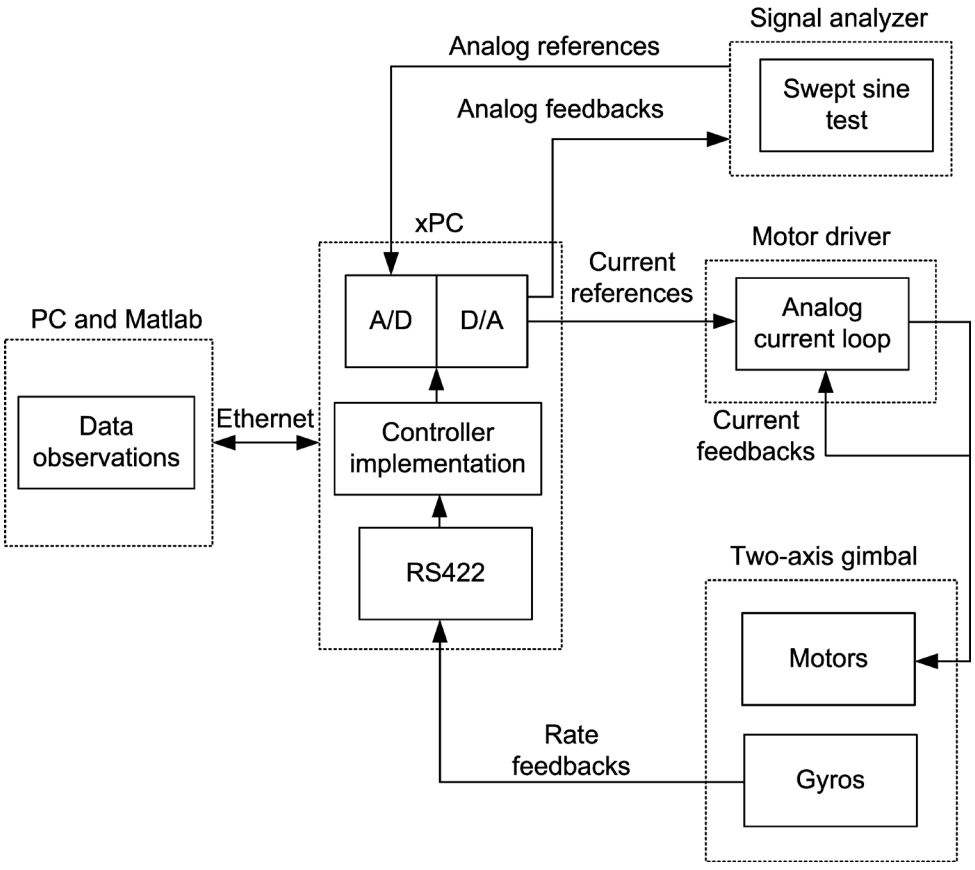

Figure 36: Block diagram of overall system

The main part of the system is xPC target which includes the control algorithms, communication channels, A/D and D/A conversion channels. Digital stabilization loop is evaluated at 3 kHz frequency. Firstly, the rate feedbacks are obtained via RS422 channel of xPC target. Secondly, corresponding current references which are the output of controllers are sent by D/A channels to motor driver. Then the driver card evaluates the analog current loop, and it supplies the required currents to gimbal motors. The experimental setup where the controllers are tested is illustrated in Fig. 37 below.

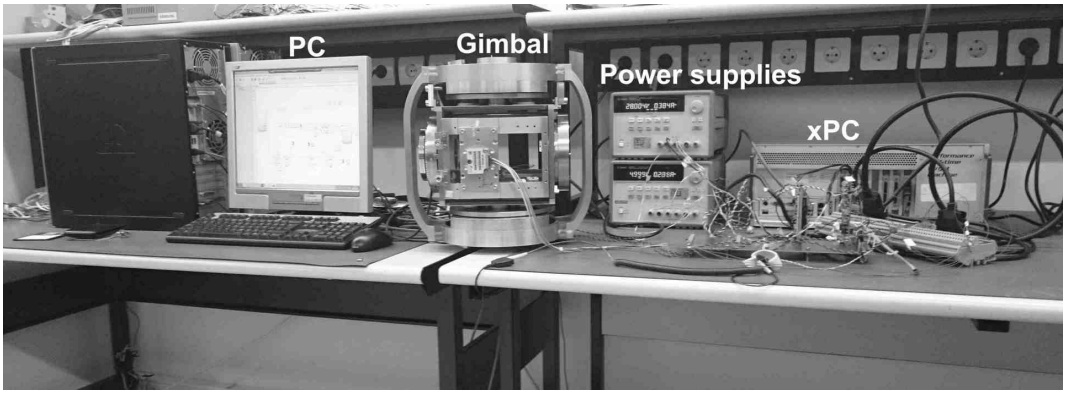

Figure 37: Experimental setup

4.1.1. Motor Driver

The main aim of the motor driver is to supply required currents to gimbal motors. The analog current loop operates such that the analog current reference which is come from xPC target is followed. Generally, the current controller is tuned such that it gives around 1 kHz bandwidth. Since this is very high compared to gimbal mechanical bandwidth, the current loop transfer function is usually approximated by constant in model construction stage.

The working principle of the analog current loop is illustrated in Fig. 38. The analog current reference is compared with the actual current and the error enters to analog pi controller. The result of the pi controller is compared with triangle signal and corresponding PWM signals that drives the mosfets of power converter are generated. The clamping diodes in the structure serve as an anti-windup structure in analog current

loop. At the end, the required current is supplied to the motor. The motor driver in the experimental setup which supplies currents to both elevation and azimuth axes is shown in Fig. 39 with motor and analog signal connections.

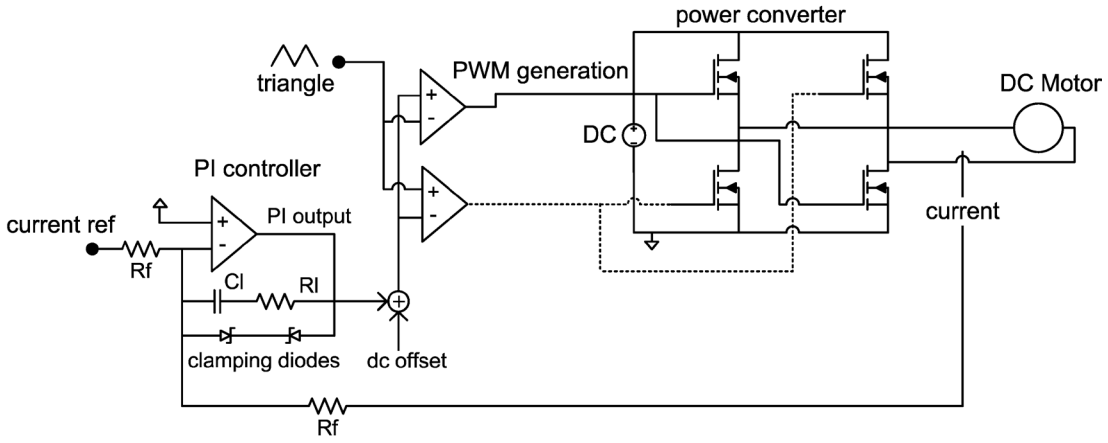

Figure 38: Analog current loop

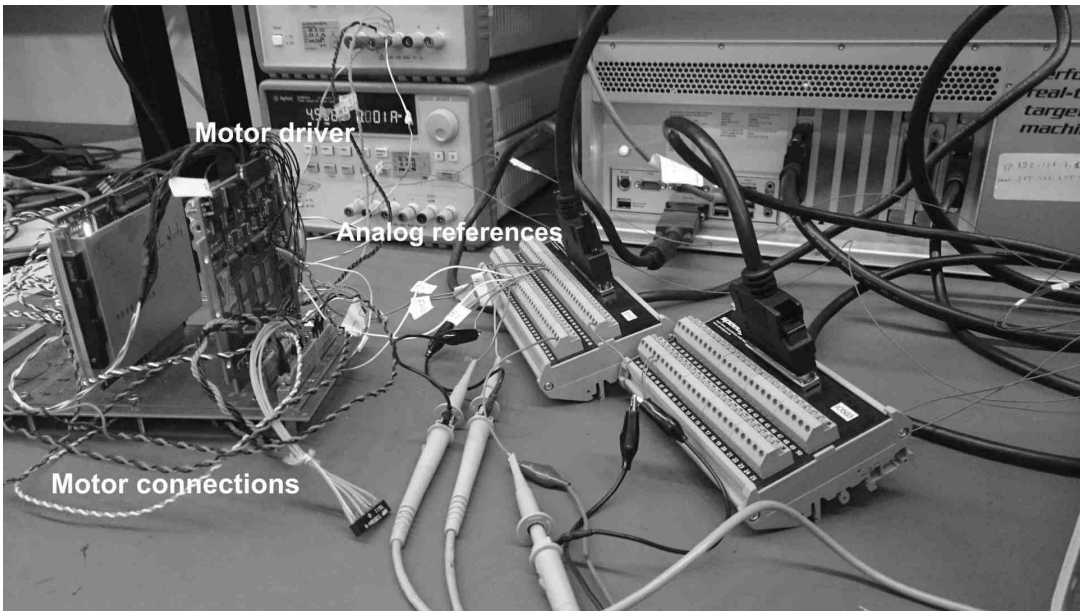

Figure 39: Motor driver in experimental setup

4.1.2. Two-axis Gimbal

The two-axis gimbal that is used for stabilization of LOS is illustrated in Fig. 40. On the gimbal three-axis gyro can be seen. Moreover, MATLAB environment where the algorithms are prepared is also seen in Fig. 40.

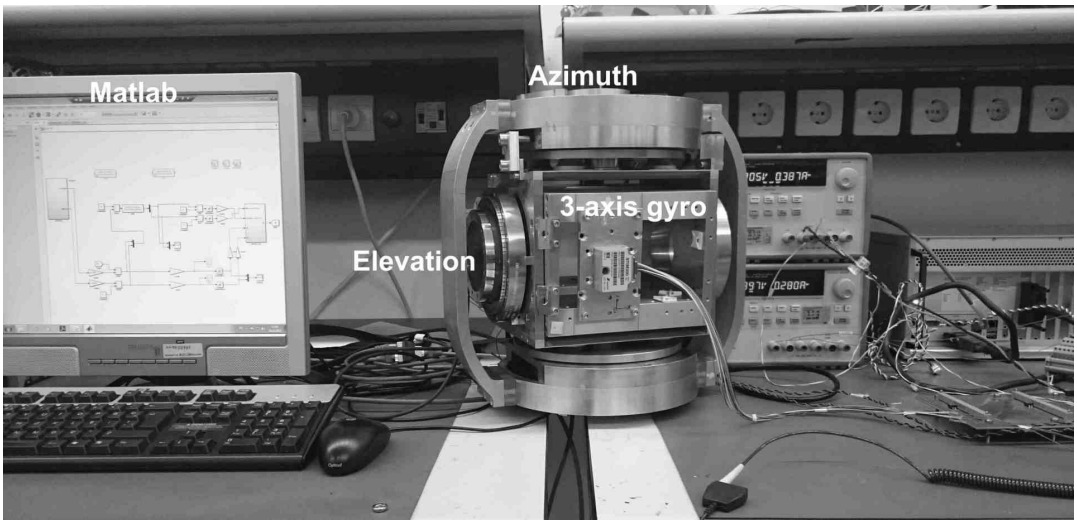

Figure 40: Two-axis gimbal in experimental setup

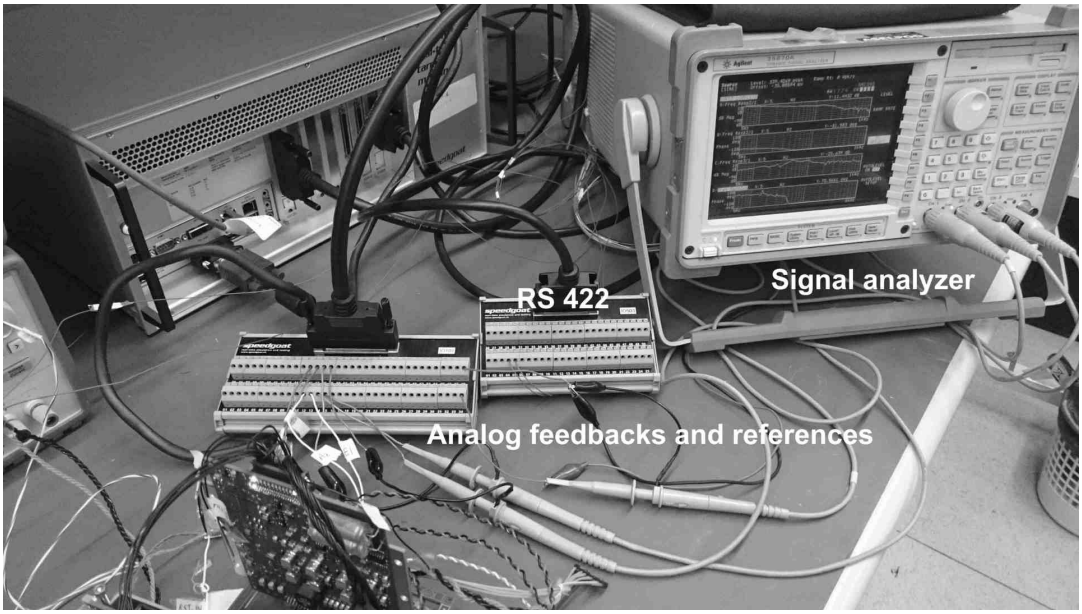

Figure 41: Signal analyzer in experimental setup

4.1.3. Signal Analyzer

Signal analyzer is a device that is used for obtaining a frequency response of a system by looking at the analog input and output signals of a system.

In this thesis, the local linearizations of the gimbal system are obtained using swept sine tests with different input excitations levels. By obtaining frequency responses of these models, the signal analyzer is used which is depicted in Fig. 41 above. Moreover, it is also used while evaluating the closed loop experimental responses.

4.2. Summary

In this chapter, a brief introduction of the experimental setup is made. In the remaining part of the thesis, all identification, evaluation and data collection are made using this system and the devices introduced in this chapter.

CHAPTER 5

SYSTEM MODELING AND IDENTIFICATION

The main motivation of this chapter is to find a nominal model for the two-axis gimbal system that will be used in robust controller design in the following chapters. Firstly, the dynamic equations of the two-axis gimbal are obtained. Then making reasonable assumptions about the structure of the gimbal simpler dynamic equations that will be used for stabilization are derived. Next, the theoretical model of the gimbal is explained. It turns out that the gimbal model is nonlinear due to the friction in the system. However, by exciting the system with sufficiently large input, the nonlinear effect can be assumed to be small. Under this condition, the gimbal model can be approximated with a LTI model. Next, parameter identification is performed using continuous-discrete extended Kalman filter using this model. Finally, the nominal model of the two-axis gimbal is obtained that will be used for controller design.

5.1. Dynamic Model of a Two-Axis Gimbal

The common structure of a two-axis gimbaled sensor is given in Fig. 42. An outer gimbal can rotate about yaw axis, and yaw axis carries inner pitch axis. The sensor or camera is mounted on inner pitch axis. The rate gyros that measure pitch and yaw rates are also placed on pitch axis. Gimbals are assumed to be rigid bodies, and three frames are introduced. Body fixed frame (B), a frame fixed to the outer yaw (azimuth) gimbal (A), and the frame fixed to pitch (elevation) gimbal (E) [10, 27].

Let x_{az}, y_{az}, z_{az} show azimuth frame axes and x_{el}, y_{el}, z_{el} show elevation frame axes. The sensor's axes x_h, y_h, z_h are given such that x_{el}, x_h and z_{az}, z_h coincide. Moreover, let ψ denote the angular rate for azimuth axis, and θ denote the angular rate for elevation axis. Using Euler angles, the rotation matrices are introduced in Eq. (5.1) and Eq. (5.2) about *z* and *y* axis respectively.

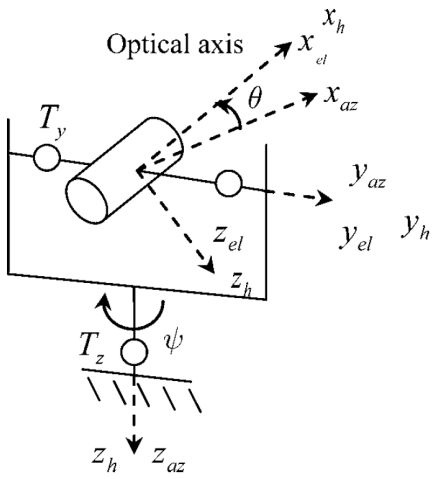

Figure 42: Two-axis yaw-pitch gimbal

$$R_{z\psi} = \begin{bmatrix} cos\psi & sin\psi & 0 \\ -sin\psi & cos\psi & 0 \\ 0 & 0 & 1 \end{bmatrix} \tag{5.1}$$

$$R_{y\theta} = \begin{bmatrix} cos\theta & 0 & -sin\theta \\ 0 & 1 & 0 \\ sin\theta & 0 & cos\theta \end{bmatrix} \tag{5.2}$$

$$w_B = \begin{bmatrix} p \\ q \\ r \end{bmatrix},\ w_A = \begin{bmatrix} w_{ax} \\ w_{ay} \\ w_{az} \end{bmatrix},\ w_E = \begin{bmatrix} w_{ex} \\ w_{ey} \\ w_{ez} \end{bmatrix} \tag{5.3}$$

In Eq. (5.3) p, q, r denote the inertial angular velocities of roll, pitch and yaw of B frame, and w_A and w_E are the velocities of the azimuth and elevation (A and E frame) respectively. Then using transformations given in Eq. (5.4), the angular rates of the azimuth and elevation axes due to p, q, r are obtained and they are given in Eqs. (5.5) and (5.6), respectively.

$$w_A = R_{z\psi} w_B\ ,\ w_E = R_{y\theta} w_A \tag{5.4}$$

$$\begin{aligned} w_{ax} &= \rho cos\psi + q sin\psi \\ w_{ay} &= -\rho sin\psi + q cos\psi \\ w_{az} &= r + \dot{\psi} \end{aligned} \tag{5.5}$$

$$
\begin{aligned}
w_{ex} &= w_{ax}cos\theta - w_{az}sin\theta \\
w_{ey} &= w_{ay} + \dot{\theta} \\
w_{ez} &= w_{ax}sin\theta + w_{az}cos\theta
\end{aligned}
\tag{5.6}
$$

The inertia matrices of gimbals are given in Eqs. (5.7) and (5.8).

$$
azimuth\ gimbal = \begin{bmatrix} J_{axx} & J_{axy} & J_{axz} \\ J_{axy} & J_{ayy} & J_{ayz} \\ J_{axz} & J_{ayz} & J_{azz} \end{bmatrix} \tag{5.7}
$$

$$
elevation\ gimbal = \begin{bmatrix} J_{exx} & J_{exy} & J_{exz} \\ J_{exy} & J_{eyy} & J_{eyz} \\ J_{exz} & J_{eyz} & J_{ezz} \end{bmatrix} \tag{5.8}
$$

The dynamic equations of a two-axis gimbal can be derived using Euler angular relations and conservation of momentum as given in Eq. (5.9). The detailed derivation of this problem is made in [27], and the results are briefly summarized here.

$$
T = \frac{dH}{dt} + w\,x\,H \tag{5.9}
$$

In Eq. (5.9), $H = Jw$ is the angular momentum of rigid body and T is the total of external torques. Then the equation of elevation gimbal is given as Eq. (5.10),

$$
J_{eyy}\dot{w}_{ey} = T_y + TQ_{el} \tag{5.10}
$$

where $T_y = T_{elmotor} - T_d$ is the net torque applied to the elevation gimbal. The total disturbance torque is composed of external frictions and other unmodeled torques $\left(T_d = T_{elviscous} + T_{elfriction} + T_{elext}\right)$. Moreover, the torque component due to inertial angular rates exerted on elevation gimbal TQ_{el} is given as Eq. (5.11) [27].

$$
\begin{aligned}
TQ_{el} = &\left(J_{ezz} - J_{exx}\right)w_{ex}w_{ez} + J_{exz}\left(w_{ex}{}^2 - w_{ez}{}^2\right) \\
&- J_{eyz}\left(\dot{w}_{ez} - w_{ex}w_{ey}\right) - J_{exy}\left(\dot{w}_{ex} - w_{ey}w_{ez}\right)
\end{aligned}
\tag{5.11}
$$

In the same manner, the equation of azimuth gimbal is given as Eq. (5.12),

$$
RJ_{azz}\dot{w}_{az} = T_z + TQ_{az} \tag{5.12}
$$

where $T_z = T_{azmotor} - T_d$ is the net torque given to azimuth gimbal. The instantaneous inertia about azimuth axis due to pitch rotation θ is given in Eq. (5.13).

$$RJ_{azz} = J_{azz} + J_{exx}\sin^2\theta + J_{ezz}\cos^2\theta - J_{exz}\sin 2\theta \tag{5.13}$$

The torque due to inertial angular rates TQ_{az} can be expressed in Eq. (5.14) [27],

$$TQ_{az} = T_1 + T_2 + T_3 \tag{5.14}$$

where T_1, T_2 and T_3 satisfy Eqs. (5.15)-(5.17) respectively.

$$T_1 = \left[J_{axx} + J_{exx}\cos^2\theta + J_{ezz}\sin^2\theta + J_{exz}\sin 2\theta - \left(J_{ayy} + J_{eyy}\right)\right] w_{ax} w_{ay} \tag{5.15}$$

$$T_2 = -\left[J_{axz} + (J_{ezz} - J_{exx})\sin\theta\cos\theta + J_{exz}\cos 2\theta\right]\left(\dot{w}_{ax} - w_{ay} w_{az}\right) \tag{5.16}$$

$$-\left(J_{ayz} + J_{eyz}\cos\theta - J_{exy}\sin\theta\right)\left(\dot{w}_{ay} + w_{ax} w_{az}\right) - \left(J_{axy} + J_{exy}\cos\theta + J_{eyz}\sin\theta\right)\left({w_{ax}}^2 - {w_{ay}}^2\right)$$

$$T_3 = \ddot{\theta}\left(J_{exy}\sin\theta - J_{eyz}\cos\theta\right) + \dot{\theta}\left[\left(J_{exx} - J_{ezz}\right)\left(w_{ax}\cos 2\theta - w_{az}\sin 2\theta\right)\right. \tag{5.17}$$

$$\left. + 2J_{exz}\left(w_{ax}\sin 2\theta + w_{az}\cos 2\theta\right) + \left(J_{eyz}\sin\theta + J_{exy}\cos\theta\right)\left(w_{ey} + w_{ay}\right) - J_{eyy} w_{ax}\right]$$

5.2. Dynamic Model Used For Stabilization

Most of the time, the products of inertias J_{exy}, J_{exz}, J_{eyz}, J_{axy}, J_{axz}, J_{ayz} are very small such that they can be neglected. Moreover, the gimbal is designed in such a way that it is mass balanced. In other words, $J_{exx} = J_{ezz}$, $J_{axx} = J_{ayy}$ are satisfied. After making these assumptions, TQ_{el} becomes zero and Eq. (5.10) reduces to Eq. (5.18).

$$J_{eyy}\dot{w}_{ey} = T_y \tag{5.18}$$

Equation (5.18) suggests that the elevation angular velocity $\dot{w}_{ey}$ is independent of any body and azimuth motion and it only depends on the net external torque applied to elevation gimbal [27].

Similarly, for the azimuth axis Eqs. (5.19)-(5.23) are obtained.

$$RJ_{azz} = J_{azz} + J_{ezz} \tag{5.19}$$

$$T_1 = [J_{axx} + J_{exx} - \left(J_{ayy} + J_{eyy}\right)] w_{ax} w_{ay} \tag{5.20}$$

$$T_2 = 0 \tag{5.21}$$

$$T_3 = -J_{eyy}\dot{\theta} w_{ax} \tag{5.22}$$

$$TQ_{az} = \left[J_{axx} + J_{exx} - \left(J_{ayy} + J_{eyy}\right)\right] w_{ax} w_{ay} - J_{eyy}\dot{\theta} w_{ax} \tag{5.23}$$

Shortly, TQ_{az} term is not totally eliminated as in the case of elevation gimbal. However, due to the higher order terms TQ_{az} is usually small, and its effect can be neglected. For that reason, Eq. (5.12) can be approximated by Eq. (5.24).

$$RJ_{azz}\dot{w}_{az} = T_z \tag{5.24}$$

Equation (5.24) implies that the azimuth angular velocity $\dot{w}_{az}$ is independent of any body and elevation movement, and it only depends on net external torque applied to azimuth gimbal.

In short, when the gimbal is mass balanced and the products of inertias are negligible the dynamic equations are simplified greatly.

In Fig. 43, typical two-axis gimbal system is shown. It includes current servo loop, motor, gimbal dynamics and gyro model.

The current loop includes a PI current controller, PWM generator, H-Bridge, motor inductance and resistance. Usually, the electrical time constant of the motor is much smaller than the mechanical time constant of the system. With the help of this property, the current closed loop bandwidth can be made sufficiently larger than the rate closed loop. Under this assumption, it is possible to represent the current loop with a constant to simplify the model. Moreover, it is also possible to represent rate gyro as a combination of second order low pass filter and some delay. The gyro delay can be approximated with a second order Pade approximation as in Eq. (5.25) at low frequency region.

$$e^{-ds} \approx \frac{\left(d^2/12\right)s^2 - \left(d/2\right)s + 1}{\left(d^2/12\right)s^2 + \left(d/2\right)s + 1} \tag{5.25}$$

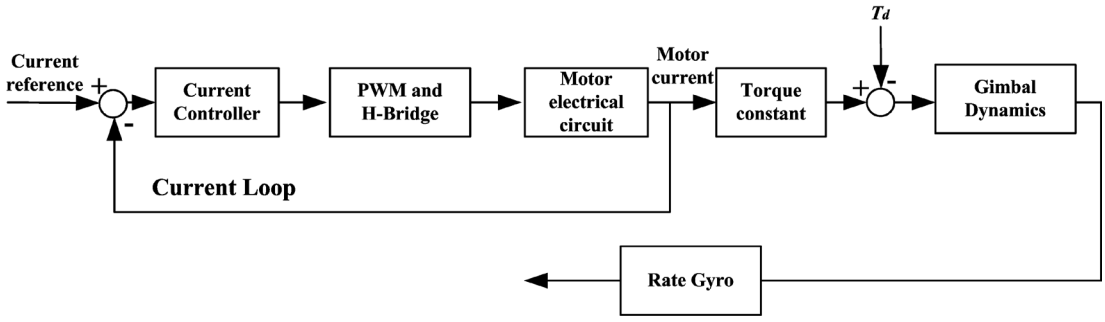

Figure 43: Typical gimbal system

Finally, by adding dynamic (viscous) friction and static friction model (coulomb + stiction) [28, 29], the overall model shown in Fig. 44 is obtained. Since the frictions depend on relative angular speeds $\dot{\psi}$ and $\dot{\theta}$, w_h and w_b are introduced in Fig. 44. For elevation gimbal, w_h and w_b denote w_{ey} and w_{ay} respectively. Similarly, for azimuth gimbal, w_h and w_b correspond w_{az} and r. This small modification leads to the friction models depend only on $\dot{\psi}$ and $\dot{\theta}$ for azimuth and elevation axes respectively.

Note that, due to existence of friction the gimbal model is nonlinear and nonlinear design methods need to be considered. However, last two decades show that although several nonlinear identification and control techniques are introduced, these still appear to be disadvantageous compared to linear counterparts [30]. In this aspect, multiple model approaches are developed to model and control the nonlinear models [30, 31]. In these methods, the nonlinear models are decomposed into simple linear models which have limited operating regions. Then one wishes to design a controller that not only stabilizes these locally linearized models but also satisfies certain performances. If the single robust controller satisfies the required performances for all models, the designer may stop there. If the uncertainty is so large that the single controller gives very poor results, the designer needs to consider some robust adaptive methods [32] or gain scheduled control methods [33].

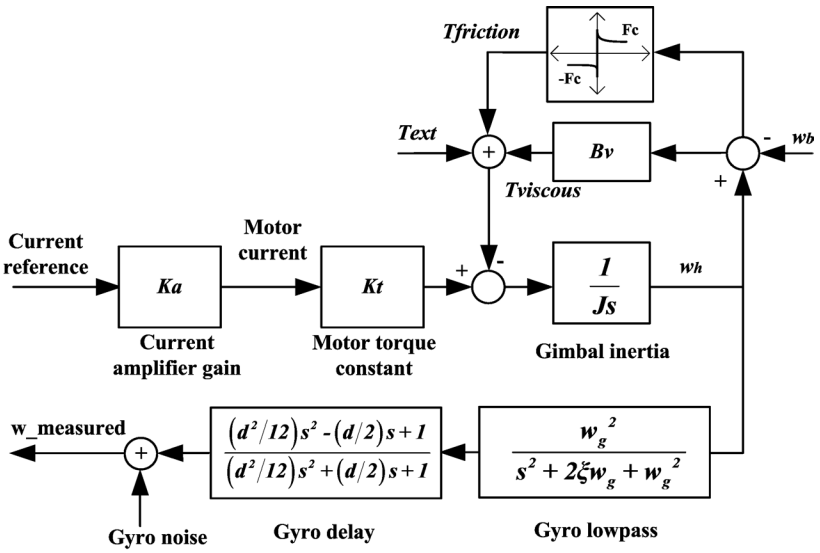

Figure 44: Gimbal model

In this thesis, similar idea is utilized. In other words, the locally linearized models are considered to be the perturbations of the actual nonlinear system, and the nonlinear model is represented by this linear model set. In short, robust control of these linear models corresponds to robust control of actual nonlinear model. In this aspect, controllers which satisfy the performance and stability properties for all these linear models are searched. Since the uncertainty in the structure is small, single robust controller satisfies the required performances as discussed in the next chapters.

It is reasonable assumption to take the nominal model of the system as in Eq. (5.26) by neglecting the nonlinear friction and w_b.

$$G(s) = \frac{w_{measured}}{i_{reference}} = \frac{K_a K_t}{Js + B_v} x \frac{w_g^2}{s^2 + 2\xi w_g + w_g^2} x \frac{\left(d^2/12\right)s^2 - \left(d/2\right)s + 1}{\left(d^2/12\right)s^2 + \left(d/2\right)s + 1} \quad (5.26)$$

Under this assumption the nonlinear disturbance coming from the model itself can be added to other external disturbances, and total disturbance can be expressed as Eq. (5.27).

$$T_d = T_{friction} + T_{ext} - B_v w_b \quad (5.27)$$

5.3. Experimental Parameter Measurement

In this section, the input is accepted to be large enough so that the model given in (5.26) is a good approximation of the true model. In the gimbal structure, the current controller is tuned such that the current loop has more than 1 kHz bandwidth. Under this condition, the current loop transfer function is assumed to be 2 where the gain results from the analog current loop circuitry in the motor driver. Moreover, the torque constant is directly obtained from the datasheet of motor. The gyro bandwidth is 262 Hz with a sufficient damping as given in the datasheet [34]. However, determination of inertia J and viscous constant B_v requires more complicated analysis.

Table 2: Parameters of the system

Parameters	Values
Current amplifier gain, K_a	2 A/A
Motor torque constant, K_t	2.18 Nm/A
Natural frequency of rate gyro, w_g	1646 rad/s
Damping of gyro, ξ	0.8
Gyro delay, d	4.5 ms

5.3.1. Extended Kalman Filter for Parameter Estimation

Parameter estimation and system identification are essential to form a mathematical model of the system by using measured data. This problem can be solved by two techniques, namely offline and online techniques. Offline techniques are iterative processes and they use all the data set available. However, online techniques are recursive and they use data when it becomes available. Since the sensor usually contains noise, and there may be unobservable states and biases in the model, the filtering techniques are preferred [35]. Kalman filter (KF), that uses mean and variance of Gaussian process and measurement noises in its time and measurement update states, is a recursive optimal filter in least square sense [36-38]. Since the method of parameter estimation through state augmentation is nonlinear, the nonlinear filtering technique must be utilized.

The most common nonlinear filtering technique is extended Kalman filter (EKF). In this thesis, the parameters (inertia J and viscous constant B_v) are found by using EKF.

5.3.1.1. Problem Simplification

While using continuous-discrete extended Kalman filter (CD-EKF), at the stage of time update, the states and entries of covariance matrices are found solving differential equations. In this aspect, to solve the parameter identification problem, it is necessary to keep the model as simple as possible. To get rid of the singularity problems in numerical solution of differential equations, the delay is approximated with a first order low pass filter as in Eq. (5.28). This assumption is only valid when the system is excited with a low frequency signal where the magnitude and phase responses of these two transfer functions are very close.

$$\frac{\left(d^2/12\right)s^2-\left(d/2\right)s+1}{\left(d^2/12\right)s^2+\left(d/2\right)s+1}\approx\frac{1}{ds+1} \tag{5.28}$$

Figure 45 illustrates that approximation of second order Pade with a first order transfer function gives very small errors at 4 Hz. Since the gimbal excitation is made with 4 Hz sinusoidal signal, using first order low pass instead of second order Pade gives very accurate result and saves a lot of computation effort that is given in the next section.

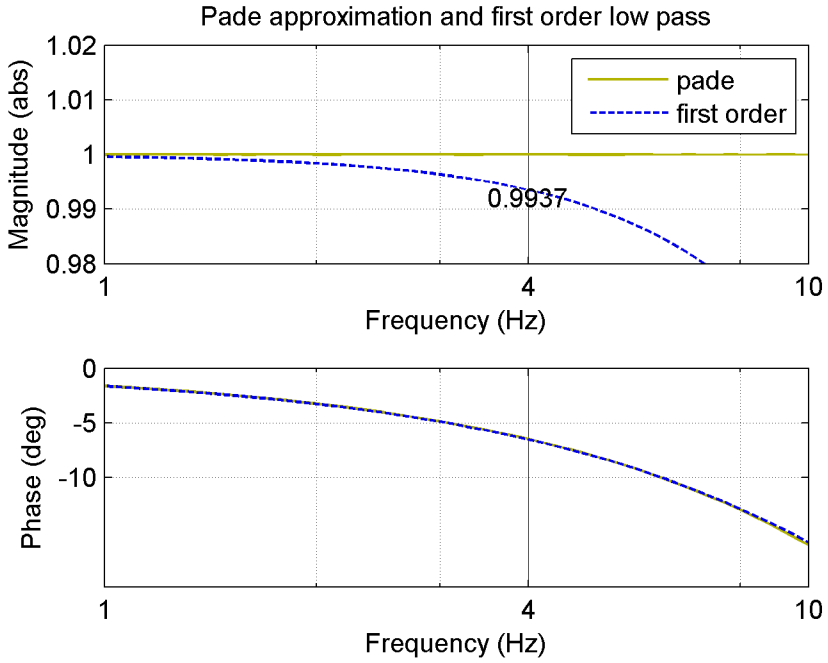

Figure 45: Pade approximation and first order low pass

So, the approximated transfer function and state space representation of the gimbal at 4 Hz are given in Eqs. (5.29) and (5.30), respectively.

$$G(s) \approx \frac{K_a K_t}{Js + B_v} x \frac{w_g^2}{s^2 + 2\xi w_g + w_g^2} x \frac{1}{ds + 1} \tag{5.29}$$

$$\dot{x} = \begin{bmatrix} 0 & 1 & 0 & 0 \\ -w_g^2 & -2\xi w_g & w_g^2 & 0 \\ 0 & 0 & -\frac{B_v}{J} & \frac{K_t}{J} \\ 0 & 0 & 0 & \frac{-1}{d} \end{bmatrix} x + \begin{bmatrix} 0 \\ 0 \\ 0 \\ \frac{1}{d} \end{bmatrix} u \ , \ y = \begin{bmatrix} 1 & 0 & 0 & 0 \end{bmatrix} x \tag{5.30}$$

Since J and B_v are unknown, they can be considered as a fifth and sixth state. This state augmentation leads to new nonlinear model as depicted in Eq. (5.31).

$$\dot{x}=\begin{bmatrix} x_2 \\ -w_g^2 x_1 - 2\xi w_g x_2 + w_g^2 x_3 \\ \dfrac{-x_6 x_3 + K_t x_4}{x_5} \\ \dfrac{-x_4 + u}{d} \\ 0 \\ 0 \end{bmatrix},\ y = x_1\ ,\ x_5 = J\ ,\ x_6 = B_v \tag{5.31}$$

5.3.1.2. Continuous-Discrete Extended Kalman Filter

Note that the gimbal model is continuous and the measurements are discrete. In this aspect continuous-discrete EKF need to be considered. For a nonlinear model given as Eq. (5.32), the equations of continuous discrete EKF are summarized below [35].

$$\begin{aligned} \dot{x} &= a(x,u,t) + \Gamma(t)w(t) \\ y &= h\left(x(t_k),k\right) + v_k \end{aligned} \tag{5.32}$$

In Eq. (5.32), $w(t)$ and $v(t)$ are white noise processes uncorrelated with $x(0)$ and each other.

$$x(0) \sim (x_0, P_o)\ ,\ w(t) \sim (0,Q)\ ,\ v(k) \sim (0,R)$$

Initialization: $P(0) = P_0,\ \hat{x} = x_o$

Time update:

Estimate: $\dot{\hat{x}} = a(\hat{x},u,t)$

Error covariance: $\dot{P} = A(\hat{x},t)P + PA^T(\hat{x},t) + \Gamma Q \Gamma^{\mathrm{T}}$

Measurement update:

Kalman gain: $K = P^- H^T \left[HP^- H^T + R\right]^{-1}$

Error covariance: $P(t_k) = \left[I - KH\right]P^{-1}$

Estimate: $\hat{x} = \hat{x}^- + K\left(y_k - h(\hat{x},k)\right)$

Jacobians: $A(x,t)=\dfrac{da(x,u,t)}{dx}$, $H(x,t)=\dfrac{dh(x,t)}{dx}$

5.3.2. Implementation

The process noise is selected such that it only affects the states to be estimated, and Γ, Q and R matrices are chosen such that they have the form shown in Eq. (5.33).

$$\Gamma=\begin{bmatrix}0&0\\0&0\\0&0\\0&0\\1&0\\0&1\end{bmatrix},\ Q=\begin{bmatrix}q_1&0\\0&q_2\end{bmatrix},\ R=r\ ,\ P=\begin{bmatrix}p_{11}&p_{12}&p_{13}&p_{14}&p_{15}&p_{16}\\p_{12}&p_{22}&p_{23}&p_{24}&p_{25}&p_{26}\\p_{13}&p_{23}&p_{33}&p_{34}&p_{35}&p_{36}\\p_{14}&p_{24}&p_{34}&p_{44}&p_{45}&p_{46}\\p_{15}&p_{25}&p_{35}&p_{45}&p_{55}&p_{56}\\p_{16}&p_{26}&p_{36}&p_{46}&p_{56}&p_{66}\end{bmatrix} \tag{5.33}$$

Step 1: Solve the state and covariance differentials Eqs. (5.34) and (5.35) during one sample time, and make time updates.

$$\begin{bmatrix}\dot{\hat{x}}_1\\\dot{\hat{x}}_2\\\dot{\hat{x}}_3\\\dot{\hat{x}}_4\\\dot{\hat{x}}_5\\\dot{\hat{x}}_6\end{bmatrix}=\begin{bmatrix}\hat{x}_2\\-w_g^2\hat{x}_1-2\xi w_g\hat{x}_2+w_g^2\hat{x}_3\\\dfrac{-\hat{x}_6\hat{x}_3+K_t\hat{x}_4}{\hat{x}_5}\\\dfrac{-\hat{x}_4+u}{d}\\0\\0\end{bmatrix} \tag{5.34}$$

$$\begin{aligned}
\dot{p}_{11}&=2p_{12}\\
\dot{p}_{12}&=p_{22}-p_{11}w_g^2+p_{13}w_g^2-2\xi p_{12}w_g\\
\dot{p}_{13}&=p_{23}-\frac{p_{13}\hat{x}_6+p_{16}\hat{x}_3}{\hat{x}_5}-\frac{p_{15}\left(K_t\hat{x}_4-\hat{x}_3\hat{x}_6\right)}{\hat{x}_5^{\,2}}+\frac{p_{14}K_t}{\hat{x}_5}\\
\dot{p}_{14}&=p_{24}-\frac{p_{14}}{d}\\
\dot{p}_{15}&=p_{25}\\
\dot{p}_{16}&=p_{26}\\
\dot{p}_{22}&=2w_g^2\left(p_{23}-p_{12}\right)-p_{12}^2-4p_{22}\xi w_g
\end{aligned} \tag{5.35}$$

$$\dot{p}_{23} = w_g^2\left(p_{33} - p_{13}\right) + \frac{p_{23}\hat{x}_6 - p_{26}\hat{x}_3 + p_{24}K_t}{\hat{x}_5} - 2\xi p_{23} w_g + \frac{p_{25}(\hat{x}_3\hat{x}_6 - K_t\hat{x}_4)}{\hat{x}_5^{\,2}}$$

$$\dot{p}_{24} = w_g^2\left(p_{34} - p_{14}\right) - \frac{p_{24}}{d} - 2\xi p_{24} w_g$$

$$\dot{p}_{25} = w_g^2\left(p_{35} - p_{15}\right) - 2\xi p_{25} w_g$$

$$\dot{p}_{26} = w_g^2\left(p_{36} - p_{16}\right) - 2\xi p_{26} w_g$$

$$\dot{p}_{33} = \frac{2p_{35}\left(-K_t\hat{x}_4 + \hat{x}_3\hat{x}_6\right)}{\hat{x}_5^{\,2}} - \frac{2(p_{36}\hat{x}_3 + p_{33}\hat{x}_6 - p_{34}K_t)}{\hat{x}_5}$$

$$\dot{p}_{34} = -\frac{p_{45}\left(K_t\hat{x}_4 - \hat{x}_3\hat{x}_6\right)}{\hat{x}_5^{\,2}} - \frac{\left(p_{46}\hat{x}_3 + p_{34}\hat{x}_6 - K_t p_{44}\right)}{\hat{x}_5} - \frac{p_{34}}{d}$$

$$\dot{p}_{35} = -\frac{p_{55}\left(K_t\hat{x}_4 - \hat{x}_3\hat{x}_6\right)}{\hat{x}_5^{\,2}} - \frac{\left(p_{56}\hat{x}_3 + p_{35}\hat{x}_6 - K_t p_{45}\right)}{\hat{x}_5}$$

$$\dot{p}_{36} = -\frac{p_{56}\left(K_t\hat{x}_4 - \hat{x}_3\hat{x}_6\right)}{\hat{x}_5^{\,2}} - \frac{\left(p_{66}\hat{x}_3 + p_{36}\hat{x}_6 - K_t p_{46}\right)}{\hat{x}_5} \qquad \text{(5.35 continued)}$$

$$\dot{p}_{44} = -\frac{2p_{44}}{d}$$

$$\dot{p}_{45} = -\frac{p_{45}}{d}$$

$$\dot{p}_{46} = -\frac{2p_{46}}{d}$$

$$\dot{p}_{55} = q_1$$

$$\dot{p}_{56} = 0$$

$$\dot{p}_{66} = q_2$$

Step 2: When measurement becomes available, make the measurement updates.

Note that to make time update, it is required to solve 6 differential equations for states and 21 equations for covariance.

5.3.3. Results

The parameters of the system are identified under sinusoidal input at 4 Hz. In Fig. 46, the grey shows the current at the motor measured with current probe, and the black shows the gyro rate output. This test is used for both azimuth and elevation axis inertia and viscous friction constant determination.

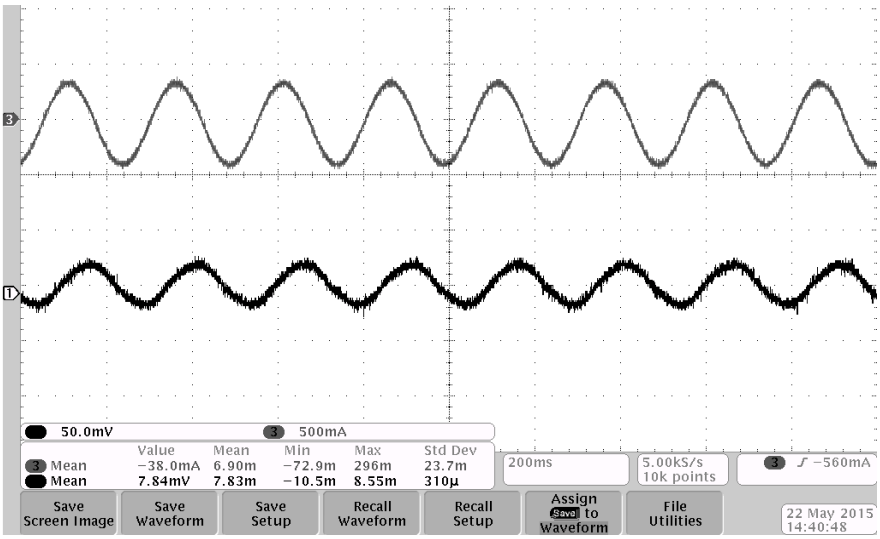

Figure 46: Current input (grey) and gyro output (black)

5.3.3.1. Azimuth Estimations

While 4 Hz, 0.8 A_{peak} sinusoidal current excitation is made to azimuth motor, the online results derived from CD-EKF is investigated. Figure 47 shows the actual and filtered output, and Fig. 48 and Fig. 49 show the inertia J and viscous constant B_v estimation for azimuth gimbal respectively.

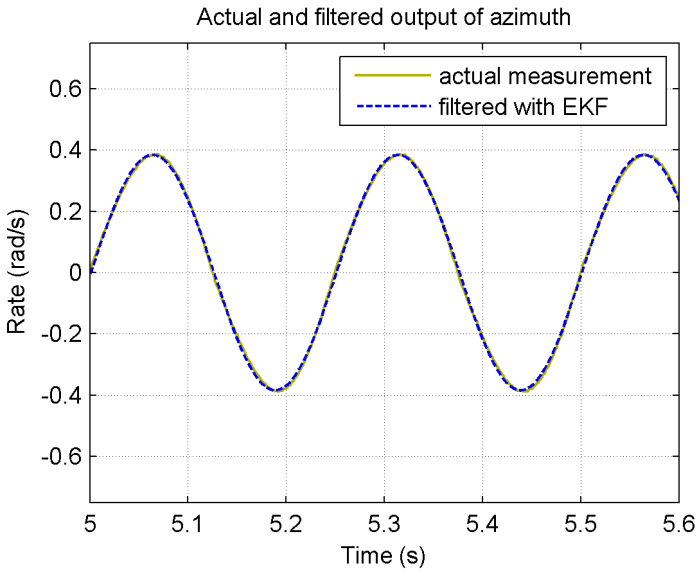

Figure 47: Actual and filtered output of azimuth

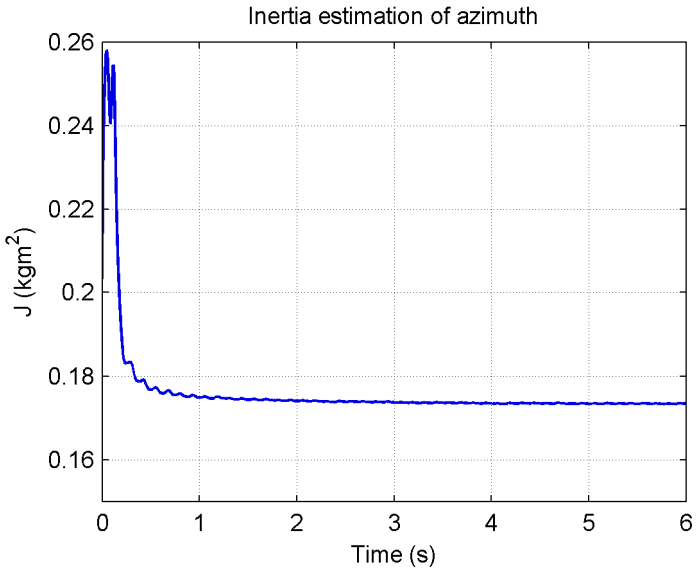

Figure 48: Inertia estimation of azimuth

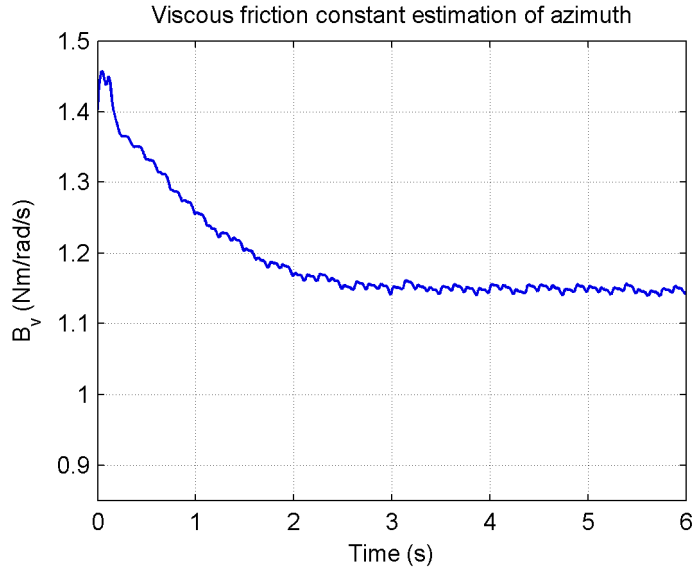

Figure 49: Viscous friction constant estimation of azimuth

5.3.3.2. Elevation Estimations

While 4 Hz, 0.5 A_{peak} sinusoidal current excitation, the results of CD-EKF is investigated for elevation gimbal. Figures 50, 51 and 52 show the actual and filtered output, the inertia J and viscous constant B_v estimation for elevation gimbal, respectively.

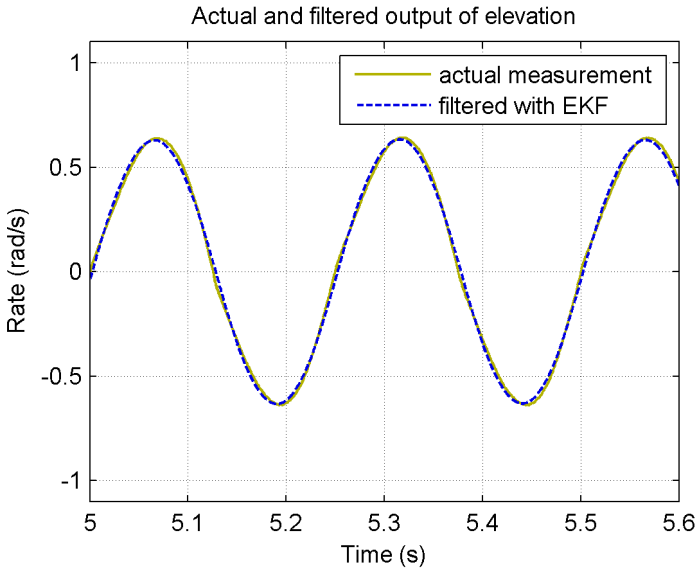

Figure 50: Actual and filtered output of elevation

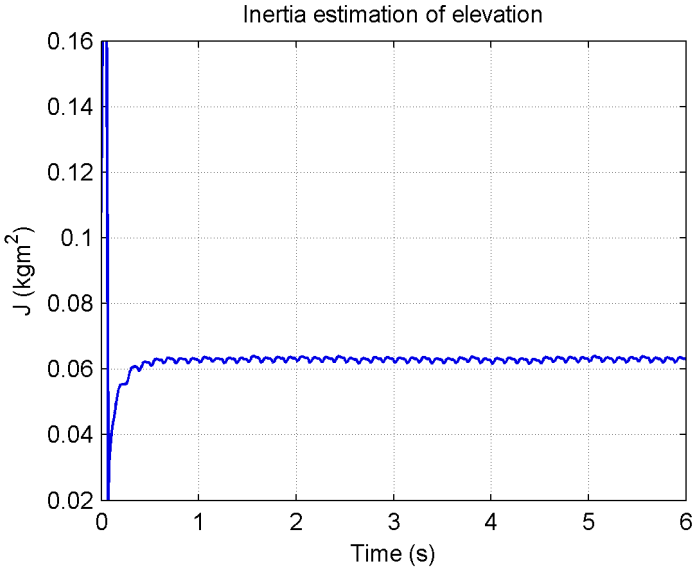

Figure 51: Inertia estimation of elevation

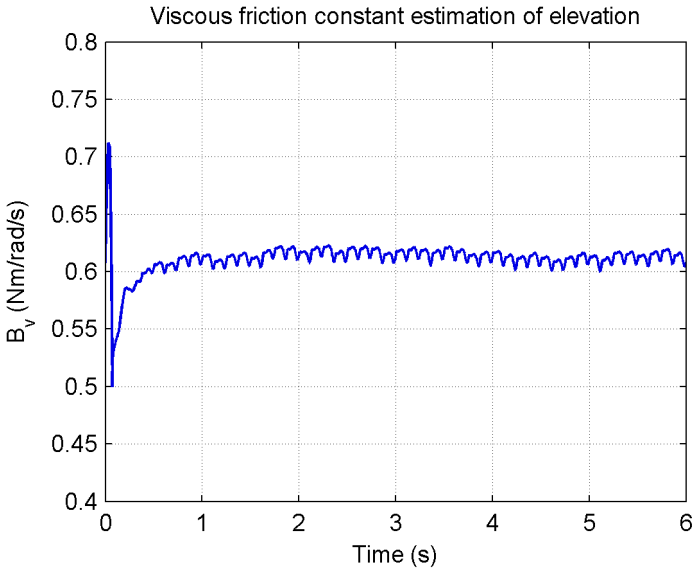

Figure 52: Viscous friction constant estimation of elevation

The results derived from parameter estimation process are expressed in Table 3.

Table 3: Estimated parameters of the system

Estimated Parameters	Values
Azimuth inertia J	0.1736 kgm^2
Azimuth viscous constant B_v	1.15 Nm/(rad/s)
Elevation inertia J	0.063 kgm^2
Elevation viscous constant B_v	0.61 Nm/(rad/s)

5.3.4. Validation of the Model

The theoretical linear model in Eq. (5.26) is evaluated with the estimation results, and it is compared with experimental data obtained by applying sine sweep to the gimbal inputs, and excitation level is selected to be same as in the parameter estimation part. The results are illustrated in Figs. 53-56.

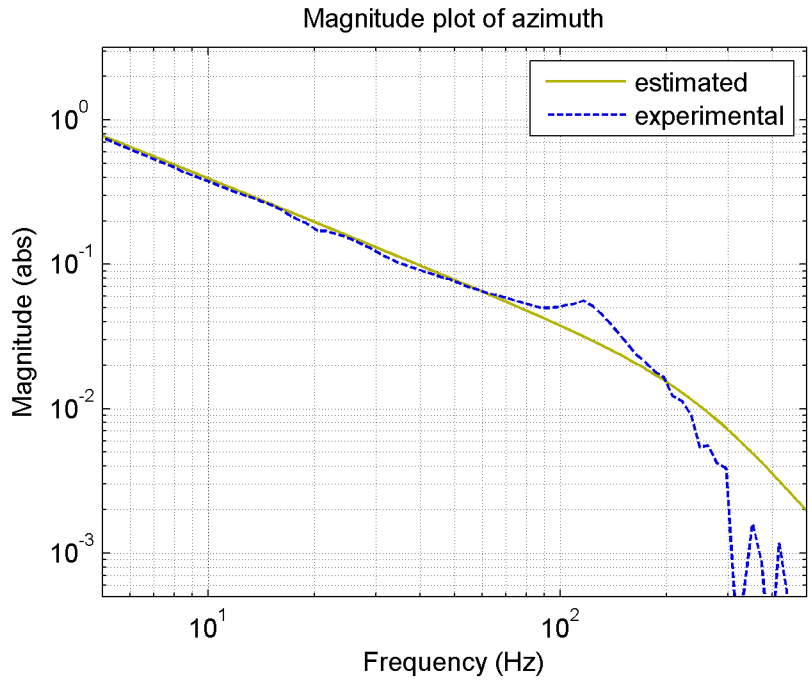

Figure 53: Magnitude plot of azimuth

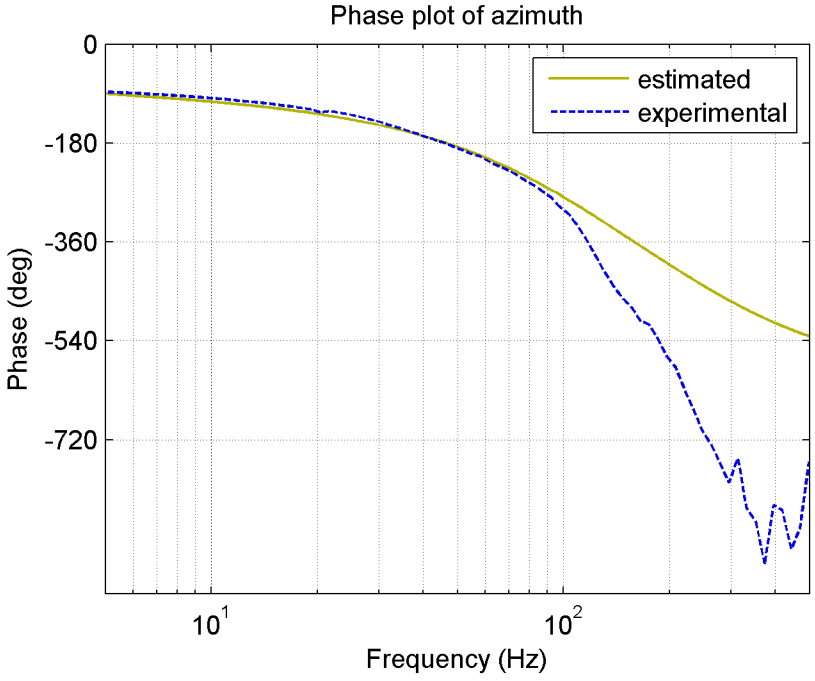

Figure 54: Phase plot of azimuth

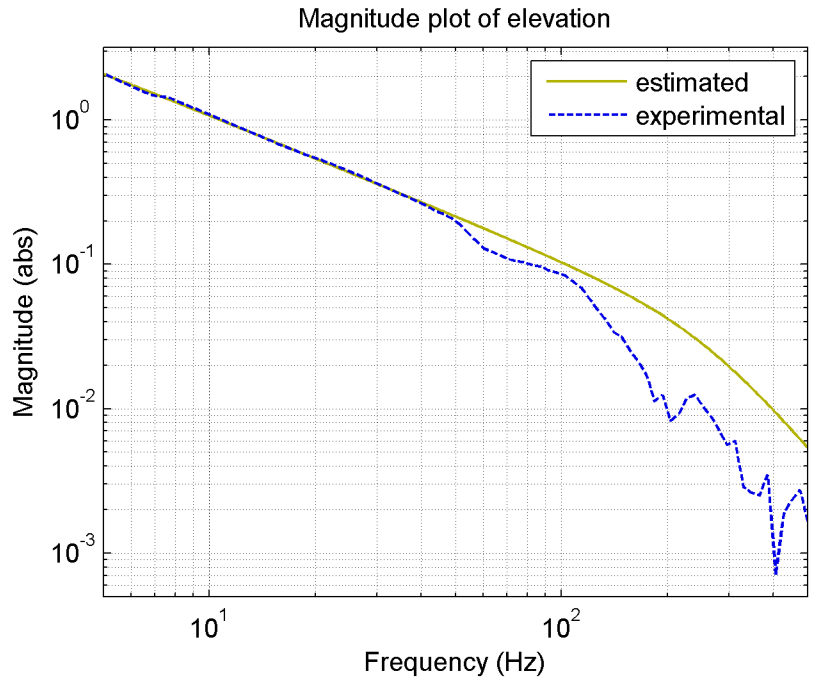

Figure 55: Magnitude plot of elevation

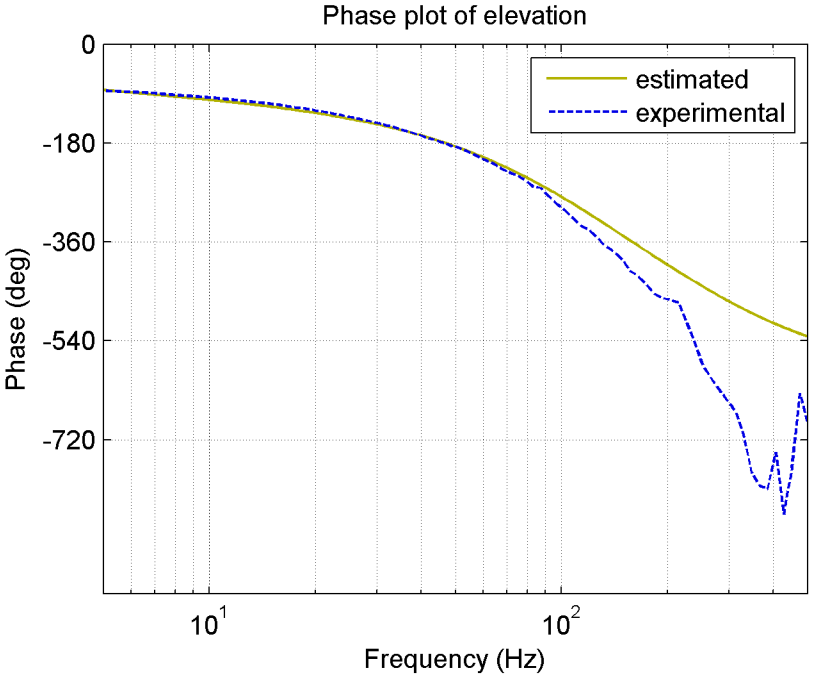

Figure 56: Phase plot of elevation

Figures 53-56 illustrate that the modeling errors at low frequencies are small. This error mainly results from the neglected nonlinearity in the model. Moreover, in high frequencies due to the neglected sensor or plant dynamics the error increases.

The detailed analysis of the modeling error determination will be discussed in Chapter 6. In this section, only the nominal model is constructed by using the estimated parameters and model in Eq. (5.26).

5.4. Nominal Model Construction

As discussed in Section 5.2, when the gimbal is accepted to be mass balanced the elevation and azimuth axes decouple. Now, validity of this assumption is investigated through the experimental data. The linearized two-axis gimbal system, can be represented by Eq. (5.36) where w_{az}, w_{el}, i_{az} and i_{el} are the azimuth and elevation angular rates and current inputs to corresponding axes' motors.

$$\begin{bmatrix} w_{az} \\ w_{el} \end{bmatrix} = \begin{bmatrix} G_{11} & G_{12} \\ G_{21} & G_{22} \end{bmatrix} \begin{bmatrix} i_{az} \\ i_{el} \end{bmatrix} \tag{5.36}$$

By making i_{el} zero, G_{11} was determined by looking at w_{az} in Section 5.3 previously. The azimuth to elevation transfer matrix G_{21} can be assumed to be zero if the gimbal is mass balanced as expressed in Section 5.2. Now by keeping i_{el} zero, under different i_{az} levels, (0.3, 0.4, 0.5, 0.6, 0.75 A_{peak}), G_{21} is examined and experimental results of these perturbations are depicted in Fig. 57.

The experimental data shows that at low frequencies the cross coupling is very small and it gets bigger at the higher frequencies where the azimuth axis has resonant mode. However, since there are very small disturbances at high frequencies, the excitement of the structure at those frequencies is not possible. In short, due to the small coupling at low frequencies where disturbances are available, the transfer function G_{21} can be assumed to be zero.

Similarly by making i_{az} zero, G_{22} was determined earlier with identification procedure in Section 5.3. By keeping i_{az} zero, under different i_{el} levels, (0.2, 0.25, 0.3, 0.35, 0.4 A_{peak}), G_{12} is examined and experimental results are given in Fig. 58.

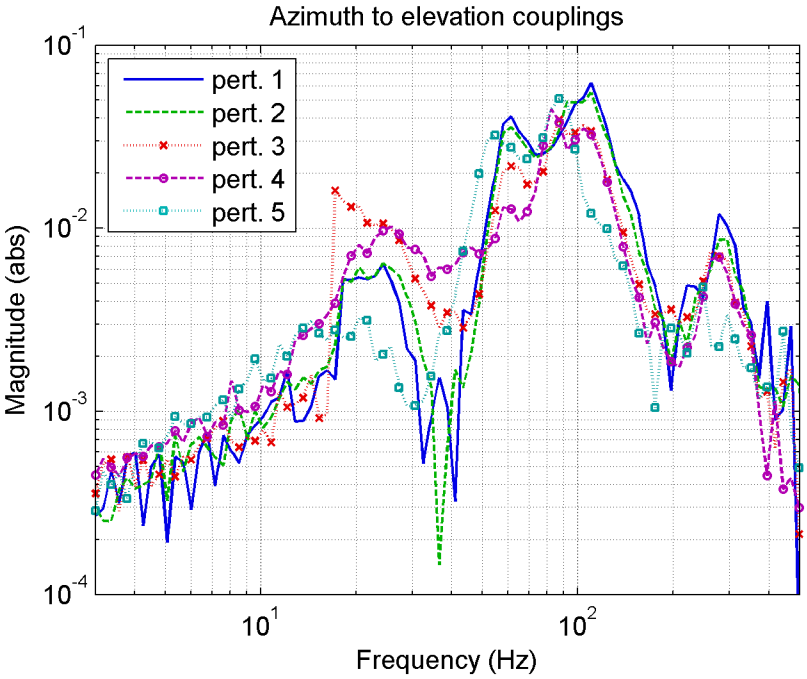

Figure 57: Azimuth to elevation couplings

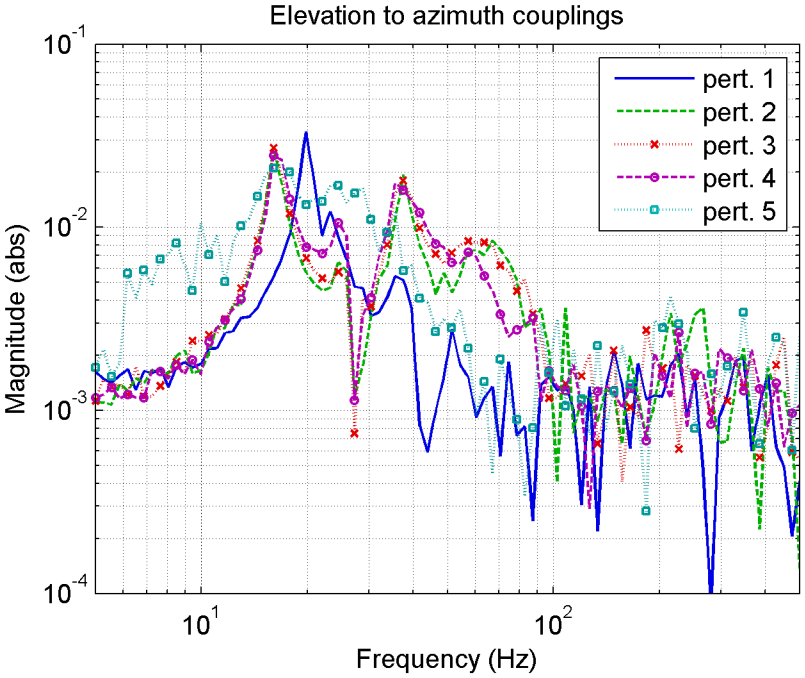

Figure 58: Elevation to azimuth couplings

The experimental data illustrates that at low frequencies the cross coupling is very small. Even if it gets bigger slightly at mid frequencies, the transfer function G_{12} can still be assumed to be zero. To conclude, the nominal model in Eq. (5.36) is constructed by assuming G_{12} and G_{21} to be zero, and the G_{11} and G_{22} are the transfer functions obtained in Section 5.3 with parameter estimation procedure.

5.5. Summary

The main motivation of this chapter is to find the nominal model of the two-axis gimbal. First, the dynamics equations of two-axis gimbal are derived. Next, by assuming gimbal is mass balanced, simpler model is obtained. Then the parameters of the gimbal are identified. Moreover, the validity of the assumption is investigated with experimental data. Finally, the nominal model of the two-axis gimbal is constructed.

CHAPTER 6

LQG/LTR, $\mathcal{H}_\infty$ AND μ CONTROLLERS DESIGN DESCRIPTIONS

6.1. Introduction

The design methods discussed in Chapter 3 use generalized plant *P*. In LQG/LTR case, the plant is augmented with transfer matrix which reflects the disturbance power spectrum. For $\mathcal{H}_\infty$ mixed sensitivity design, *S*/*KS* and *T* are weighted with corresponding transfer matrices. On the other hand, for μ-synthesis case, *S* and *KS* are weighted with transfer matrices and multiplicative uncertainty at the plant output uses maximum uncertainty bound as a weight as expressed in Chapter 3. While constructing the generalized plant for different design methods, the corresponding weight matrices must be known. In this chapter, the performance and uncertainty weights and their determination are discussed. The uncertainty bound is obtained using the experimental data that can be related with different plant perturbations. Moreover, the performance weight selection is made after a few iterations to satisfy the different design objectives. Using the weights determined in this chapter and the methods discussed in Chapter 3, the controller will be designed and results will be reported in Chapter 7.

6.2. Design Specification

The design specification for the LOS stabilization problem includes the determination of performance indices by investigating the information about external disturbances and model errors. In this section, the performance requirements are derived from the disturbance properties. After that, the modeling errors are examined by looking at the different experimental data.

6.2.1. Motivation of LOS Stabilization

The control objective of LOS stabilization includes keeping pointing vector along the LOS under the effects of platform motions. In literature, the instantaneous error between

the LOS and sensor pointing vector is called as jitter. Moreover, the angle that a single detector pixel is sensitive to radiation is named as instantaneous field of view (IFOV).

Main objective of the LOS stabilization is to reduce the jitter due to the platform disturbances. In most of the applications, it is desired that the root mean square (RMS) of the jitter during the sensor integration time should be smaller than IFOV value.

As given in Fig. 59, to get a clear image, the jitter must be small such that each detector pixel can obtain the correct radiation of the targeted object in sensor integration time [1]. In other words, when the RMS of the jitter is higher than IFOV, the radiation of each pixel mixes. When a pixel receives radiation from neighboring pixels, the image gets blurry. Consequently, to obtain a clear image RMS of the error must be smaller than IFOV value. In this thesis, jitter which has a RMS value smaller than 75 microradian (μrad) is aimed.

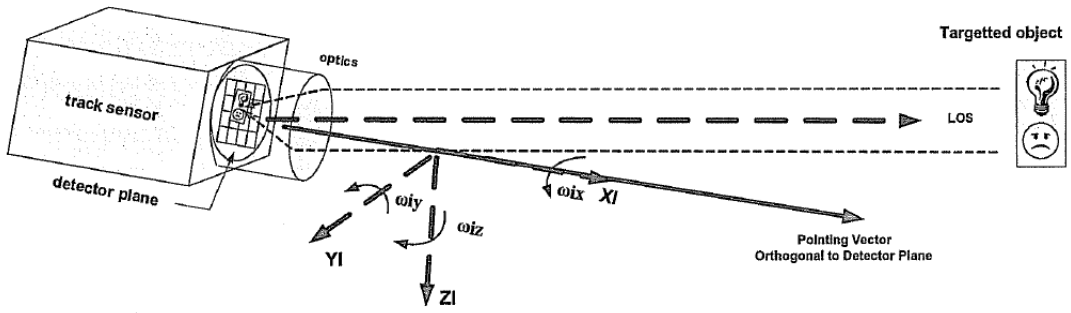

Figure 59: Track sensor

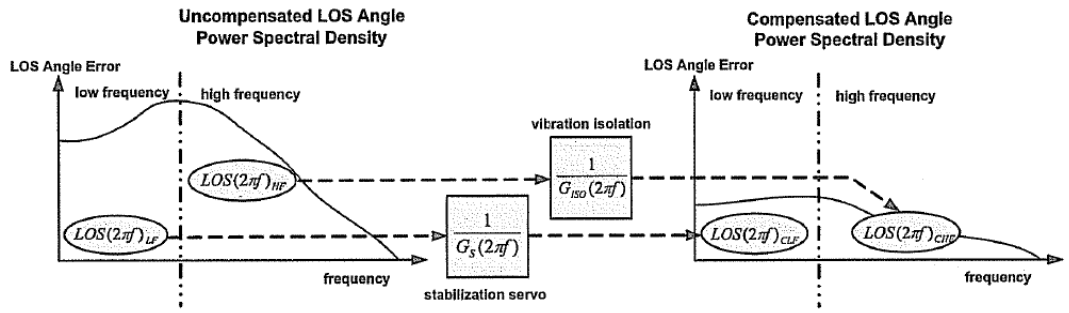

Figure 60: Conceptual performance of stabilization and vibration isolation

6.2.2. Sensitivity Weight Selection

In most applications, the power spectral density of the disturbance is considered while designing a stabilization servo loop. Usually, the low frequency disturbance is suppressed with the stabilization servo loop, and high frequency disturbances are eliminated by the vibration isolation as given in Fig. 60 graphically [1].
In this work, the platform power spectral density is obtained from the data taken from platform gyro. The spectral densities of disturbance rates for azimuth and elevation axes are depicted in Fig. 61.

It is not odd to think that these disturbances act directly to the plant output as given in Fig. 62 with *d*. After closed loop is designed, the gimbal output rates can be found by evaluating the platform rates through output sensitivity function. Then resulting rates need to be integrated to reach the jitter in both axes. Finally, by investigating the power spectral density of the jitter, required sensitivity function is searched. In other words, to satisfy the jitter below 75 μrad RMS, the true sensitivity function need to be chosen. Since high frequency disturbances are suppressed by structure itself and isolators, while analyzing jitter only the component between 0.1 and 50 Hz is considered. In this thesis, the sensitivity function depicted in Eq. (6.1) is aimed for each axis.

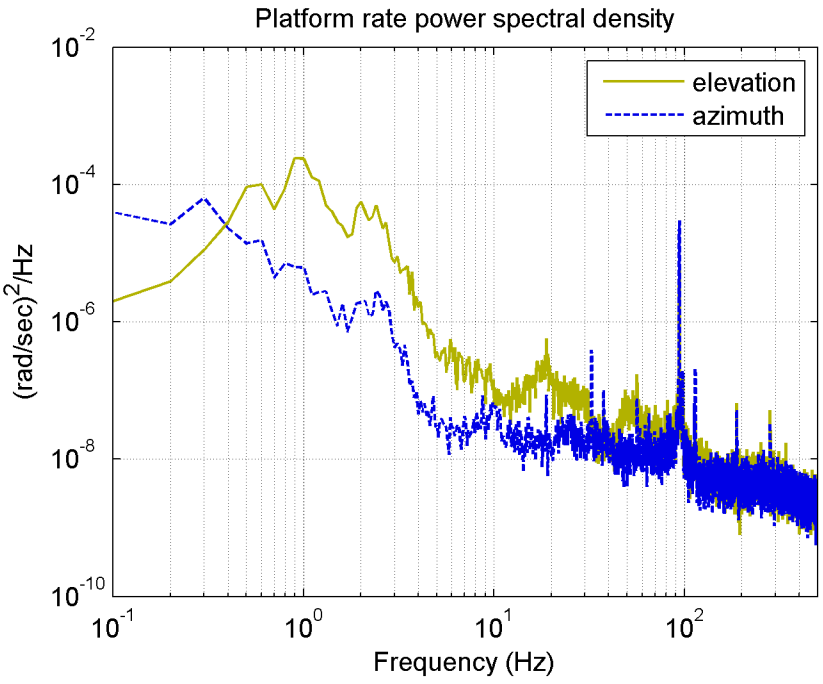

Figure 61: Platform rate power spectral density

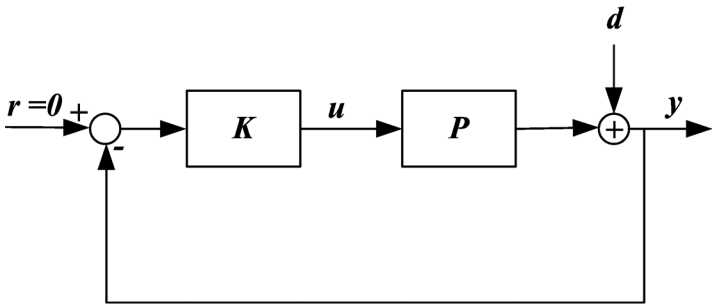

Figure 62: Feedback loop for LOS stabilization

$$S^{-1} = \left(\frac{s^2 / M_s + 2\xi w_b \sqrt[2]{M_s} + w_b^{\,2}}{s^2 + 2\xi w_b \sqrt[2]{\varepsilon} + w_b^{\,2}\varepsilon} \right),\ M_s = 1,\ \varepsilon = 0.01,\ \xi = 0.5, w_b = 2\pi 10 \quad (6.1)$$

Note that in Chapter 2 for k = 2, the sensitivity weight represented with Eq. (6.2) is discussed.

$$w_e = \left(\frac{s^2 / M_s + 2 w_b \sqrt[2]{M_s} + w_b^{\,2}}{s^2 + 2 w_b \sqrt[2]{\varepsilon} + w_b^{\,2}\varepsilon} \right) \quad (6.2)$$

However, for better loop shaping especially in *S*/*KS*/*T* scheme the weight slightly changes to the one given in Eq. (6.3). This necessity comes from the fact that higher roll off leads to higher *S* and *T* peaks at the crossover region [18].

$$w_e = \left(\frac{s^2 / M_s + 2\xi w_b \sqrt[2]{M_s} + w_b^{\,2}}{s^2 + 2\xi w_b \sqrt[2]{\varepsilon} + w_b^{\,2}\varepsilon} \right),\ M_s = 3.162,\ \varepsilon = 0.01,\ \xi = 0.5, w_b = 2\pi 10 \quad (6.3)$$

The magnitudes of weights given by Eqs. (6.2) and (6.3) are given in Fig. 63. The modified weight in Eq. (6.3) yields a higher disturbance rejection below 3 Hz, however it allows higher sensitivity peaking around the crossover. Moreover, at low frequencies disturbances are suppressed by a factor of 100. The weight lower bound at high frequencies is chosen to be 1/(3.162).

According to sensitivity shown in Eq. (6.1), the output rate power spectral density shown in Fig. 64 is obtained. After integration is made, the output position power spectral density given in Fig. 65 is obtained.

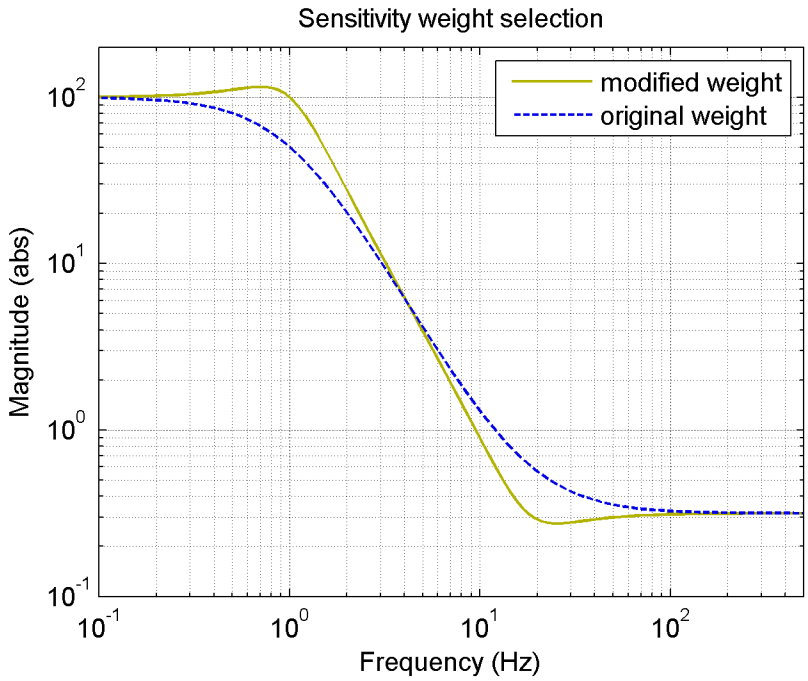

Figure 63: Sensitivity weight selection

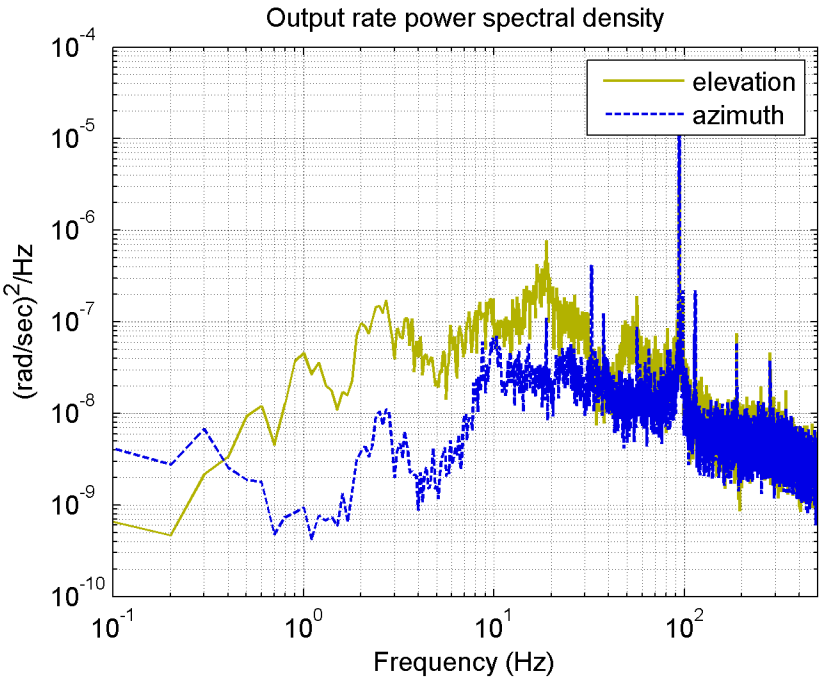

Figure 64: Output rate power spectral density

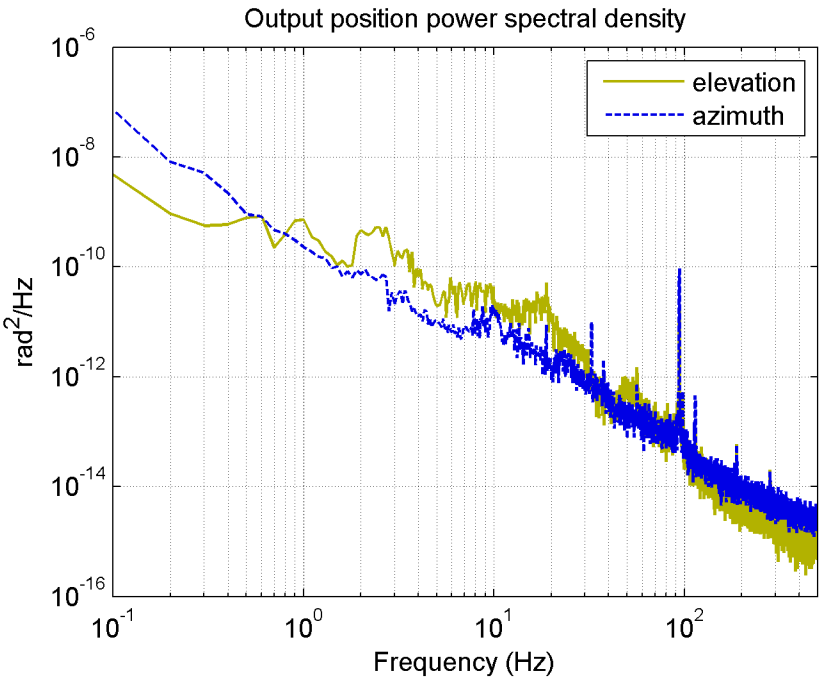

Figure 65: Output position power spectral density

The variance of the LOS error is calculated using Eq. (6.4) where G_e is the power spectral density in Fig. 65.

$$\sigma^2{}_e = \int_0^\infty G_e df \tag{6.4}$$

In pointing error analysis the process can be accepted to be zero mean [17]. Since the RMS value of jitter in 0.1 and 50 Hz is important Eq. (6.5) is used.

$$e_{rms} = \sqrt{\int_{0.1}^{50} G_e df} \tag{6.5}$$

The RMS values of the jitter are calculated from Fig. 65. For elevation axis 46 μrad and for azimuth 76 μrad RMS values are obtained. In short, sensitivity in Eq. (6.1) is a good design aim for this problem. So, sensitivity weight which is chosen for MIMO system is given in Eq. (6.6) where w_e is the transfer function given in Eq. (6.3).

$$W_e = \begin{bmatrix} w_e & 0 \\ 0 & w_e \end{bmatrix} \tag{6.6}$$

6.2.3. Control Weight Selection

It is possible to use the same procedure that was applied for sensitivity weight selection in previous section. In this case, the RMS of the control needs to be minimized such that the motors are not saturated. After closed loop is designed, the control signals can be found by evaluating the platform rates through KS_o function. The maximum possible current supplied to motor is 3 ampere (A), and recall that there is current amplifier of gain 2 in the motor driver. Then the design aim is to keep the RMS value of the control signal below 1.5 A RMS over all frequencies and for both axes.

$$(KS_o)^{-1} = \frac{s + w_{bc}/M_u}{\varepsilon_1 s + w_{bc}},\ M_u = 100,\ \varepsilon_1 = 0.01,\ w_{bc} = 2\pi 1200 \tag{6.7}$$

According to KS_o selection represented with Eq. (6.7), the control power spectral density given in Fig. 66 is obtained. According to Eq. (6.4), the RMS values of the controls are found to be 1.32 and 0.53 A RMS for elevation and azimuth axes, respectively.

$$w_u = \frac{s + w_{bc}/M_u}{\varepsilon_1 s + w_{bc}}, M_u = 100, \varepsilon_1 = 0.01, w_{bc} = 2\pi 1200 \tag{6.8}$$

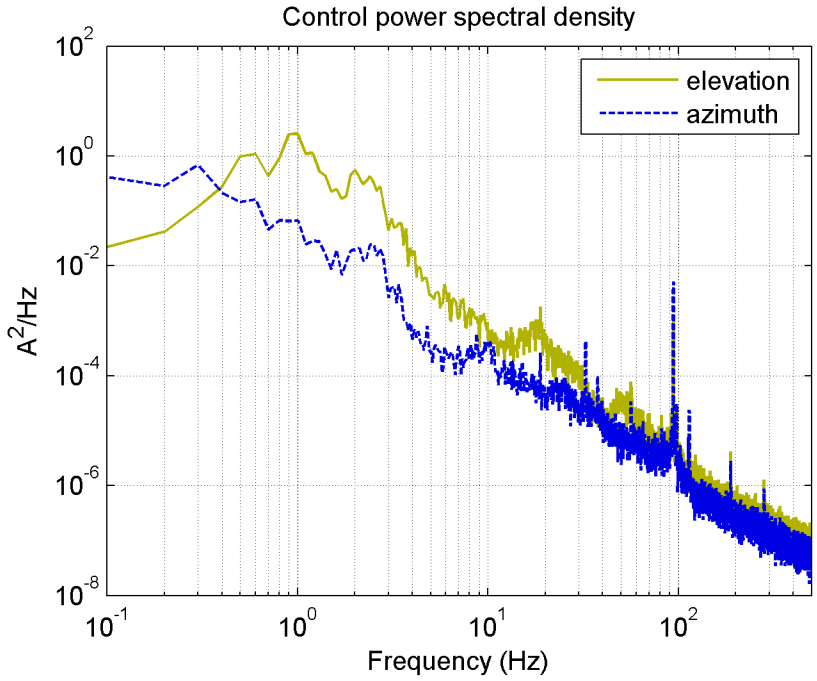

Figure 66: Control power spectral density

Hence, the control weight which is chosen for MIMO system is given in Eq. (6.9) where w_u is the transfer function given in Eq. (6.8).

$$W_u = \begin{bmatrix} w_u & 0 \\ 0 & w_u \end{bmatrix} \tag{6.9}$$

6.2.4. Uncertainty Weight Selection

As discussed in Chapter 5, the actual system is nonlinear, and the nominal model constructed is valid around a single operating point. Apart from the nonlinearity, there are also unmodeled dynamics of the gimbal which consist of structural resonances and isolator effects that are used for vibration isolation at high frequencies [1, 2]. Moreover, at high frequencies the error due to delay approximation gets bigger.

So, the purpose of this section is to construct a model set which covers all the errors which result from not only the linear model approximation but also the unmodeled dynamics.

The local linearizations of the plant are obtained by applying swept sine tests to gimbal with different excitation levels. Then using these data and nominal model the uncertainty bound is obtained.

Output multiplicative uncertainty set can be represented as Eq. (6.10) where $\|\Delta\|_\infty < 1$ and Δ and $W_1 \in \mathcal{RH}_\infty$ are satisfied.

$$\mathbf{\Pi} = \left(I + \Delta W_1\right) P \tag{6.10}$$

In order to find the uncertainty upper bound W_1, first all possible multiplicative perturbations (Δ_m's) as given in Eq. (6.11) need to be found.

$$\Delta_m(s) = \left(P_\Delta(s) - P(s)\right) / P(s) \tag{6.11}$$

In Eq. (6.11), P_Δ denotes any possible plant in the model set $\mathbf{\Pi}$. When each axis is treated as a SISO system, the uncertainty upper bound w_1 can be found which satisfy the Eq. (6.12).

$$\left|\Delta_m(jw)\right| \le \left|w_1(jw)\right| \tag{6.12}$$

By evaluating Eq. (6.11) over a grid of frequencies where there is an experimental data, the uncertainty upper bound w_1 is found by fitting a stable transfer function which upper bounds the perturbations. The results for two axes are illustrated respectively.

First, the experimental data and the nominal model of the azimuth gimbal are given in Figs. 67 and 68. The perturbations correspond to cases where the motor is excited with 0.6, 0.8, 1, 1.2 and 1.5 A_{peak} sinusoidal currents. After that, the upper bound w_{1a} is obtained using Eqs. (6.11) and (6.12) for azimuth axis, and depicted in Fig. 69.

Next, the experimental data and the nominal model of the elevation gimbal are shown in Figs. 70 and 71. In Figs. 70 and 71, perturbations are obtained under 0.4, 0.5, 0.6, 0.7 and 0.8 A_{peak} sinusoidal currents for elevation gimbal. Then the upper bound w_{1e} is obtained using Eqs. (6.11) and (6.12) for elevation axis and shown in Fig. 72.

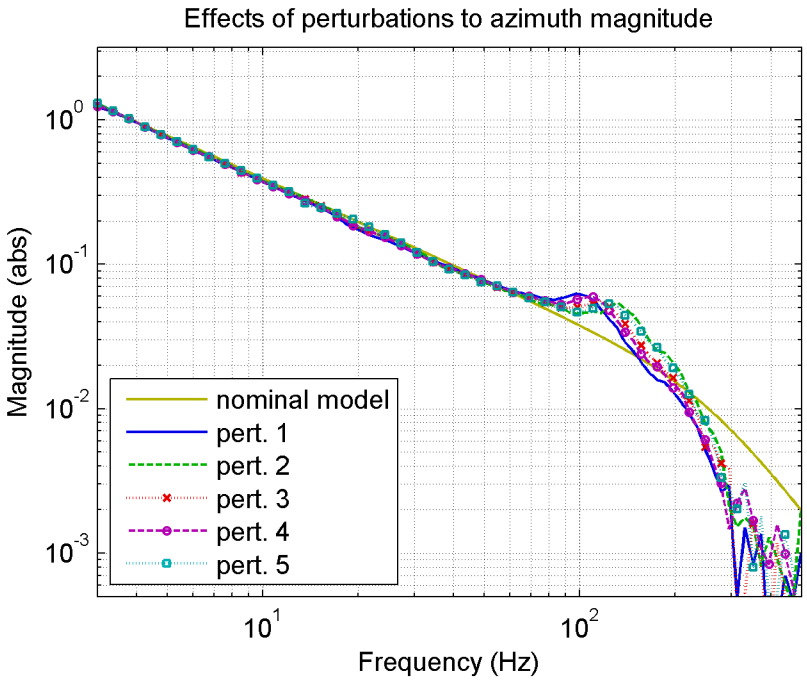

Figure 67: Effect of perturbations to azimuth magnitude

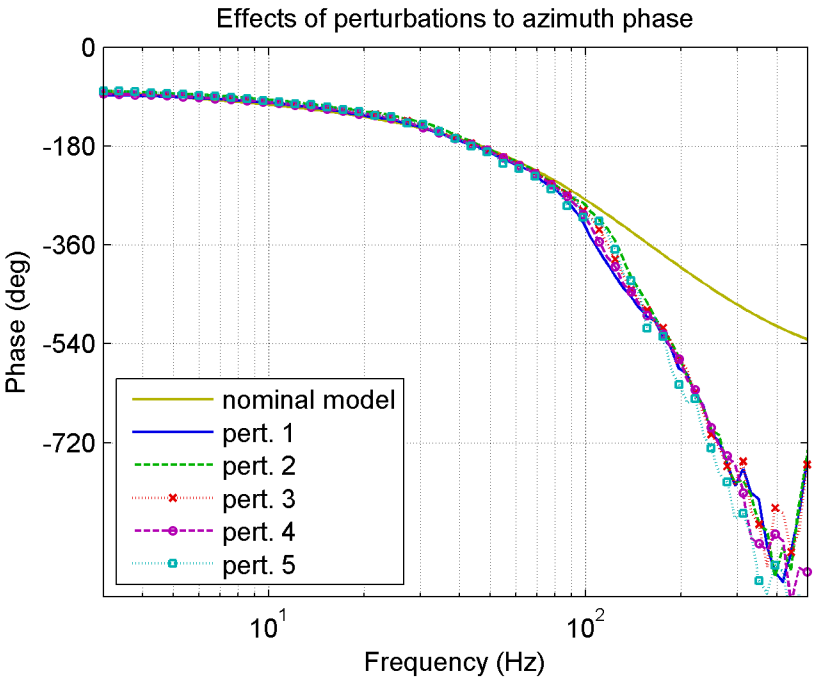

Figure 68: Effect of perturbations to azimuth phase

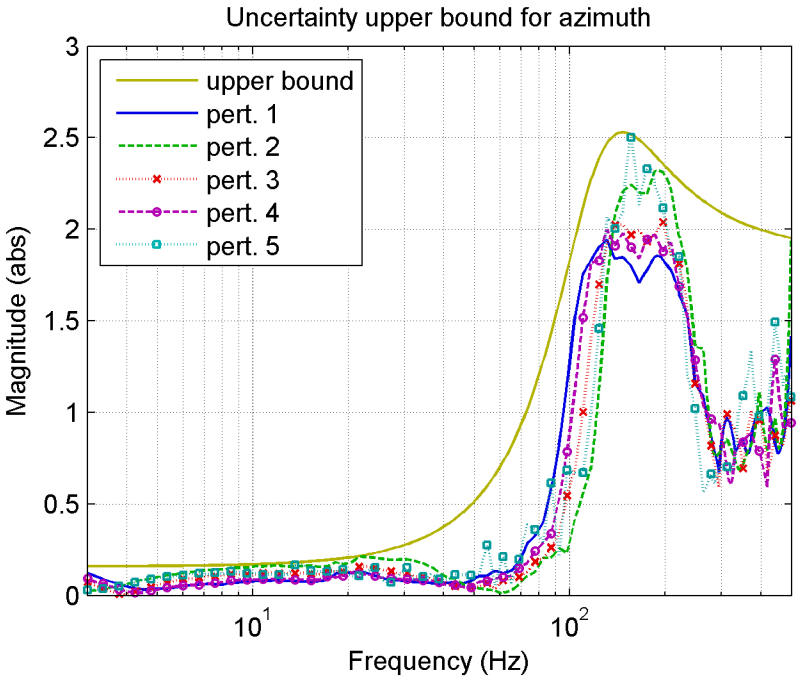

Figure 69: Uncertainty upper bound for azimuth

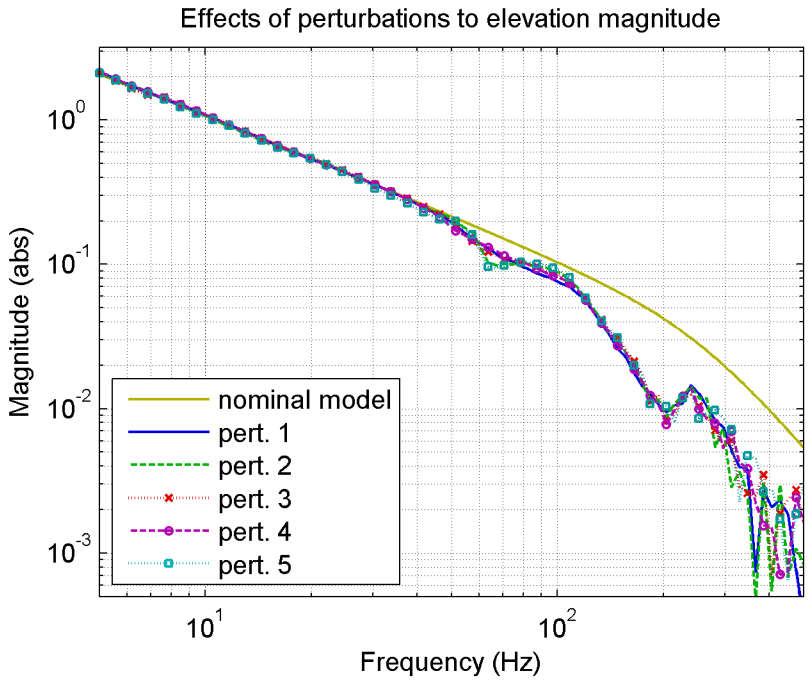

Figure 70: Effects of perturbations to elevation magnitude

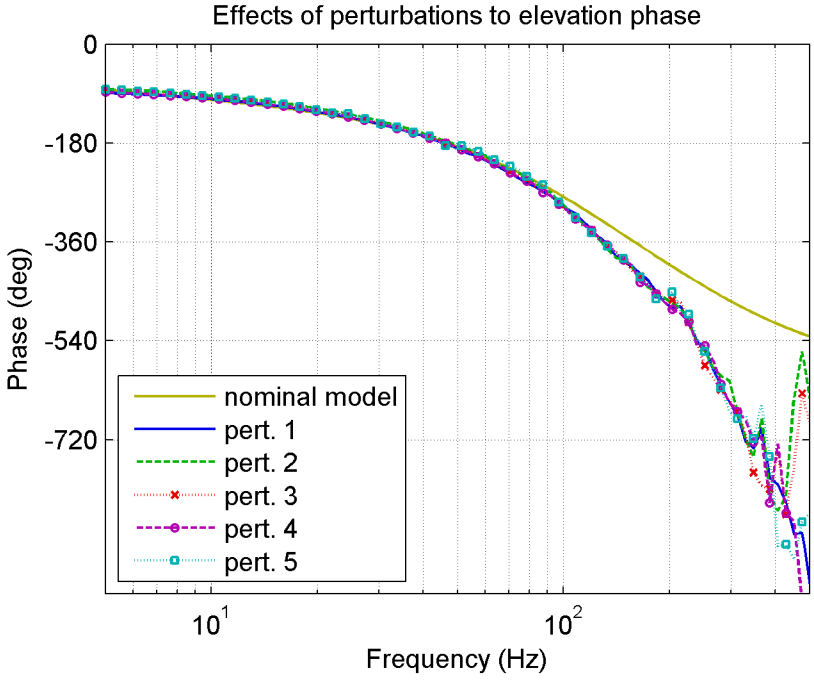

Figure 71: Effects of perturbations to elevation phase

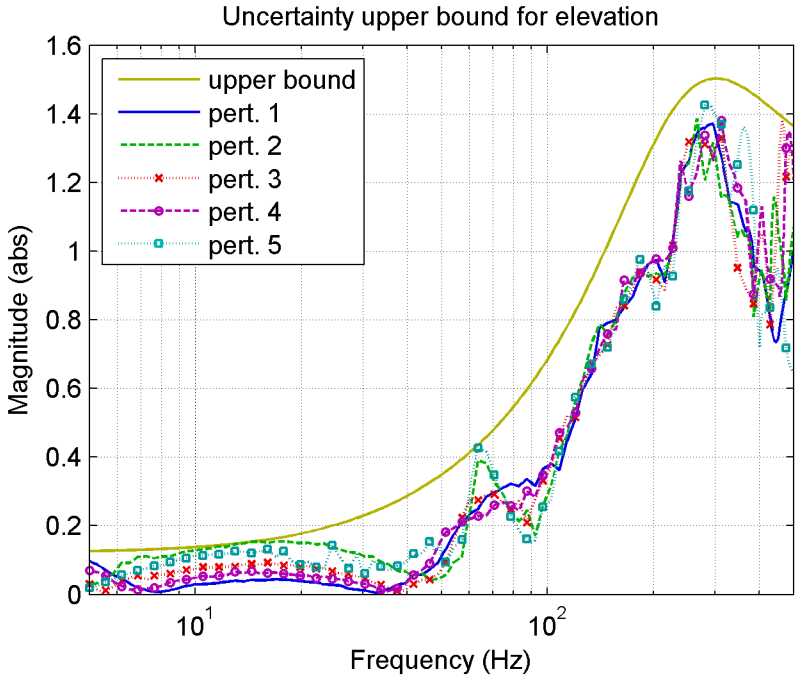

Figure 72: Uncertainty upper bound for elevation

The uncertainty upper bounds w_{1a} and w_{1e} are found for azimuth and elevation axes, respectively and denoted in Eqs. (6.13) and (6.14).

$$w_{1a} = \frac{1.87s^2 + 792.65s + 90750}{1s^2 + 650.35s + 572624} \tag{6.13}$$

$$w_{1e} = \frac{1.12s^2 + 2564.28s + 289957}{1s^2 + 2059.65s + 2375266} \tag{6.14}$$

Then the overall perturbation bound for MIMO system is given in Eq. (6.15).

$$W_1 = \begin{bmatrix} w_{1a} & 0 \\ 0 & w_{1e} \end{bmatrix} \tag{6.15}$$

By looking at the Figs. 69, 72 and transfer functions in Eqs. (6.13), (6.14), it can be seen that at low frequencies the uncertainties are below 0.15 and 0.12 for azimuth and elevation axes respectively. At high frequencies due to the structural resonances of the gimbal, the uncertainties increase dramatically. Azimuth axis uncertainty exceeds 1 around 100 Hz and reaches 2.5 at resonant frequencies. Similarly, elevation axis uncertainty goes beyond 1 at 200 Hz and reaches 1.4 at resonant frequencies. Note that these results are very similar to observations reported in [39].

6.3. Summary

Throughout this chapter, how weight selection is performed and its motivation are discussed. Briefly, the sensitivity weight W_e and control weight W_u result from the RMS requirement of the output error and control respectively. The perturbation transfer matrices are obtained using experimental data. The selected transfer matrices are given in Table 4.

Table 4: Selected weights

$$w_e = \left(\frac{s^2/M_s + 2\xi w_b/\sqrt[2]{M_s} + w_b^{\,2}}{s^2 + 2\xi w_b \sqrt[2]{\varepsilon} + w_b^{\,2}\varepsilon} \right),\ M_s = 3.162,\ \varepsilon = 0.01,\ \xi = 0.5, w_b = 2\pi 10$$

$$w_u = \frac{s + w_{bc}/M_u}{\varepsilon_1 s + w_{bc}},\ M_u = 100,\ \varepsilon_1 = 0.01,\ w_{bc} = 2\pi 1200$$

$$w_{1a} = \frac{1.87s^2 + 792.65s + 90750}{1s^2 + 650.35s + 572624},\ w_{1e} = \frac{1.12s^2 + 2564.28s + 289957}{1s^2 + 2059.65s + 2375266}$$

$$W_e = \begin{bmatrix} w_e & 0 \\ 0 & w_e \end{bmatrix},\ W_u = \begin{bmatrix} w_u & 0 \\ 0 & w_u \end{bmatrix},\ W_1 = \begin{bmatrix} w_{1a} & 0 \\ 0 & w_{1e} \end{bmatrix}$$

The state space matrices required at the plant augmentation for LQG/LTR design are illustrated in Table 5. Similarly, for $\mathcal{H}_\infty$ *S*/*KS*/*T* mixed sensitivity design, the transfer matrices in Table 6 are used. In Table 7, the weights that are used in μ-synthesis are expressed.

The transfer matrices and their usage are discussed extensively in Chapter 3. One can see Section 3.1 for LQG/LTR design, Section 3.2 for mixed sensitivity $\mathcal{H}_\infty$ design and Section 3.3 for μ-synthesis design.

Table 5: Weights for LQG/LTR design

$\left[\begin{array}{c\|c} A_d & B_d \\ \hline C_d & D_d \end{array}\right] = W_e, \quad \left[\begin{array}{c\|c} A_v & B_v \\ \hline C_v & D_v \end{array}\right] = I$

Table 6: Weights for $\mathcal{H}_\infty$ *S*/*KS*/*T* mixed sensitivity design

$W_e = W_e, \quad W_u = W_u, \quad W_t = W_1$

Table 7: Weights for μ-synthesis design

$W_e = W_e, \quad W_u = W_u, \quad W_p = W_1$

CHAPTER 7

LQG/LTR, $\mathcal{H}_\infty$ AND μ CONTROLLERS DESIGN RESULTS

7.1. Introduction

In Chapter 5, the nominal model was constructed. After augmenting this model with appropriate weights found in Chapter 6, the generalized plants are obtained. Then as discussed in Chapter 3, the LQG/LTR, $\mathcal{H}_\infty$ and μ controllers are synthesized.

For each designed controllers, the resulting closed loop two-axis gimbal system is constructed and analyzed. First, the LQG/LTR control design is made by following the procedure discussed in Chapter 3. For this case, two designs are presented to satisfy the control objectives. Next, the $\mathcal{H}_\infty$ controller is synthesized in *S*/*KS*/*T* mixed sensitivity design framework as expressed in Chapter 3 in detail. Finally, the μ-synthesis design is discussed by following the *D-K* iteration procedure by using the structures given in Chapter 3. After the controllers are obtained, the resulting closed loop transfer matrices are evaluated. The robustness of corresponding closed loops is investigated in two methods. The first method is applicable if the performance criterion is measured only by sensitivity ($\|W_e S_o\|_\infty < 1$) and there is only one uncertainty block in the loop as given in Chapter 2. The second method is applied in μ framework by accepting that the performance requirement is given as Eq. (7.1).

$$\left\| \begin{bmatrix} W_e S_o \\ W_u K S_o \end{bmatrix} \right\|_\infty < 1 \tag{7.1}$$

After the performances of the controllers are investigated individually, the comparison between them is made, and the differences among them are discussed. Finally, their performance objective achievements are briefly summarized.

7.2. LQG/LTR Design

As given in Table 4, the transfer matrix W_e which reflects the power spectrum of output disturbance *d,* is of order 4. Moreover, the nominal model constructed is of order 10. For that reason, the augmentation leads to generalized plant of order 14. Hence the corresponding LQG/LTR controller will have an order of 14.

7.2.1. Design 1

The LQG/LTR controller is designed by following the procedure outlined in Chapter 3. As discussed previously, the aim is such that the open loop transfer matrix GK_{LQG} need to approach to Kalman filter open loop transfer matrix $C\Phi K_f$. First, the designed Kalman filter and weight W_e are shown in Fig. 73. Then by reducing ρ, different optimal state feedbacks are designed, and the resulting open loop gains are given in Fig. 74. In Fig. 75, the closed loop output sensitivities can be found. Please observe that gains of the open and closed loop transfer matrices are given for nominal model. Finally, in Fig. 76 the controllers are illustrated.

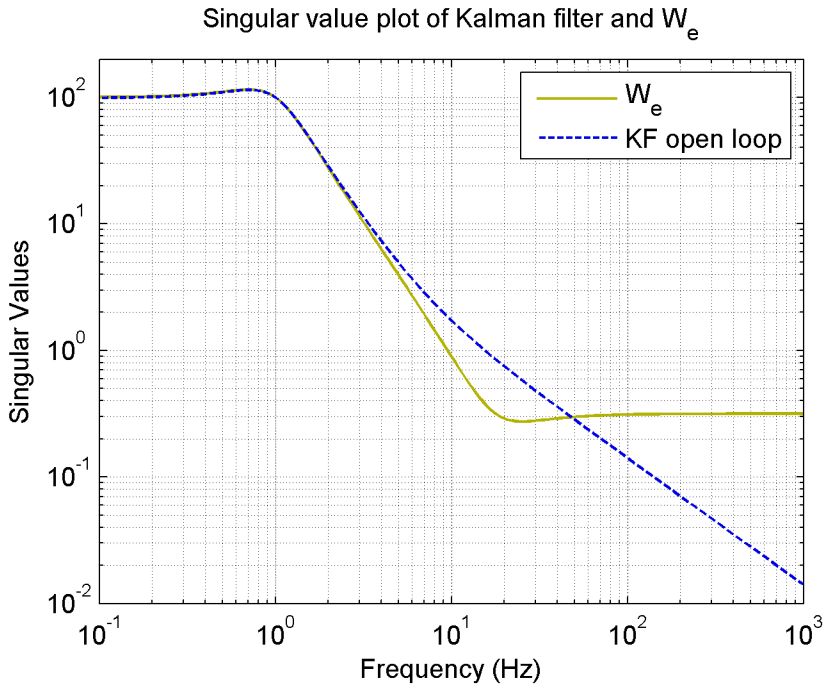

Figure 73: Singular value plot of Kalman filter and W_e for design 1

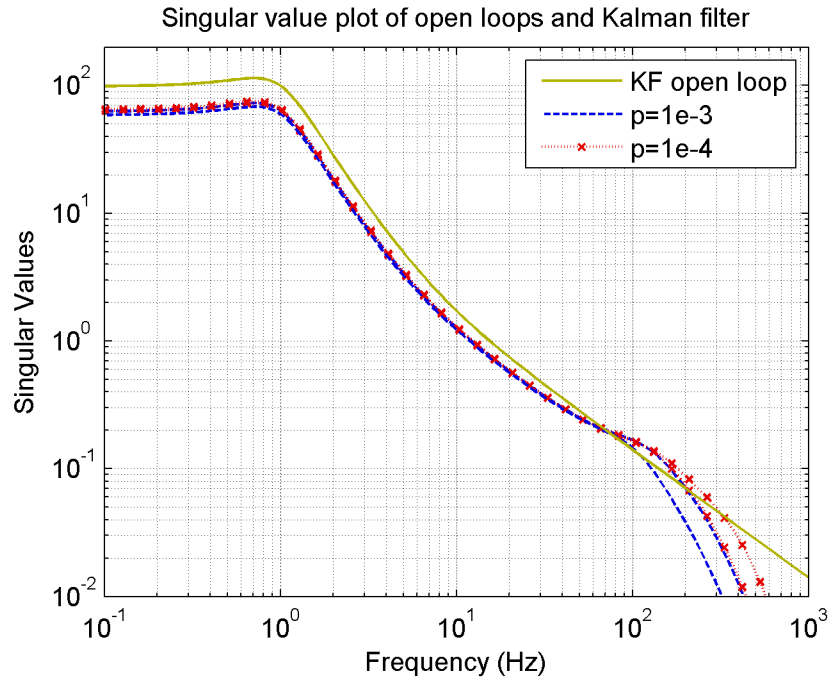

Figure 74: Singular value plot of open loops and Kalman filter for design 1

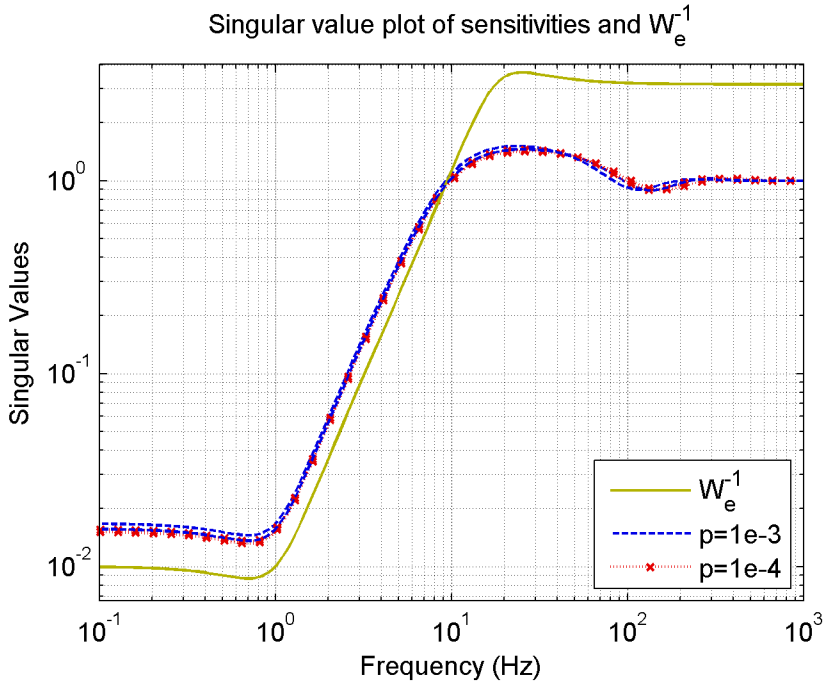

Figure 75: Singular value plot of sensitivities and W_e^{-1} for LQG/LTR design 1

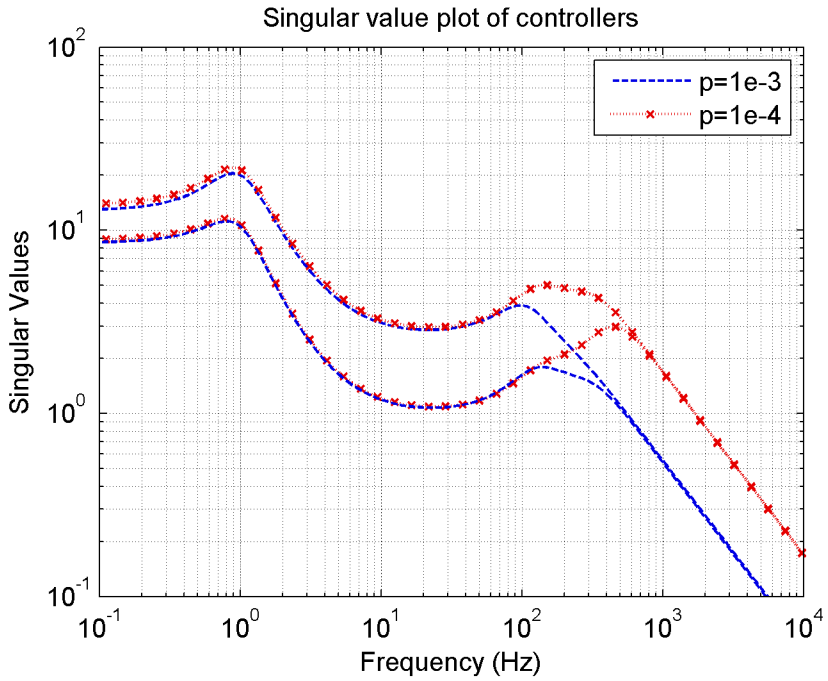

Figure 76: Singular value plot of the LQG/LTR controllers for design 1

As given in Figs. 74 and 75, the recovery procedure does not achieve the objectives successfully even if one continuously reduces ρ. The main result behind this fact is the non-minimum phase behavior of the gimbal. As discussed previously, for successful loop recovery the plant zeros are usually canceled by the compensator poles [11]. Since this is not possible for non-minimum phase plants, the procedure success reduces. To get rid of this drawback, the design 1 is reconsidered and design 2 is made.

7.2.2. Design 2

For design 2, the transfer matrix W_e which reflects the power spectral density of output disturbance d, is modified such that it has a higher bandwidth and a dc gain. For this case, the Kalman filter from two designs and modified weight W_e is plotted in Fig. 77. Then different optimal state feedbacks are designed by reducing ρ, and the resulting open loop singular values are given in Fig. 78. In Fig. 79, the closed loop output sensitivities can be found for nominal model. Finally, in Fig. 80 the controllers are plotted.

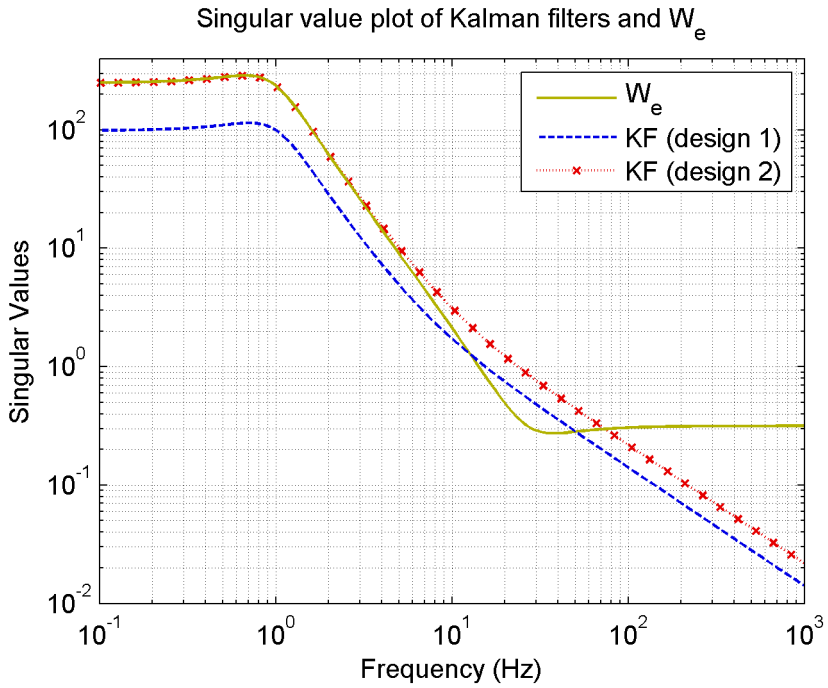

Figure 77: Singular value plot of Kalman filters and W_e for design 2

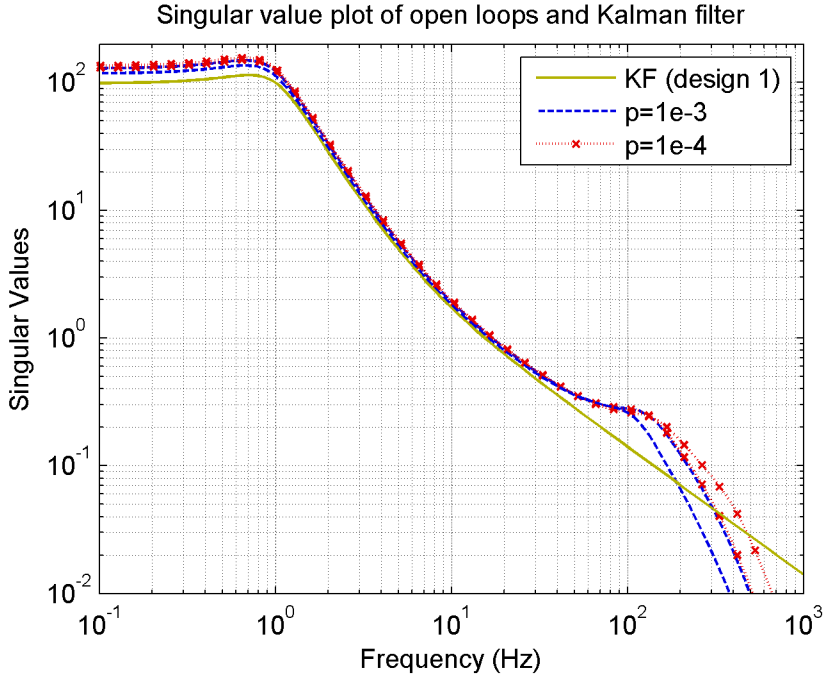

Figure 78: Singular value plot of open loops and Kalman filter for design 2

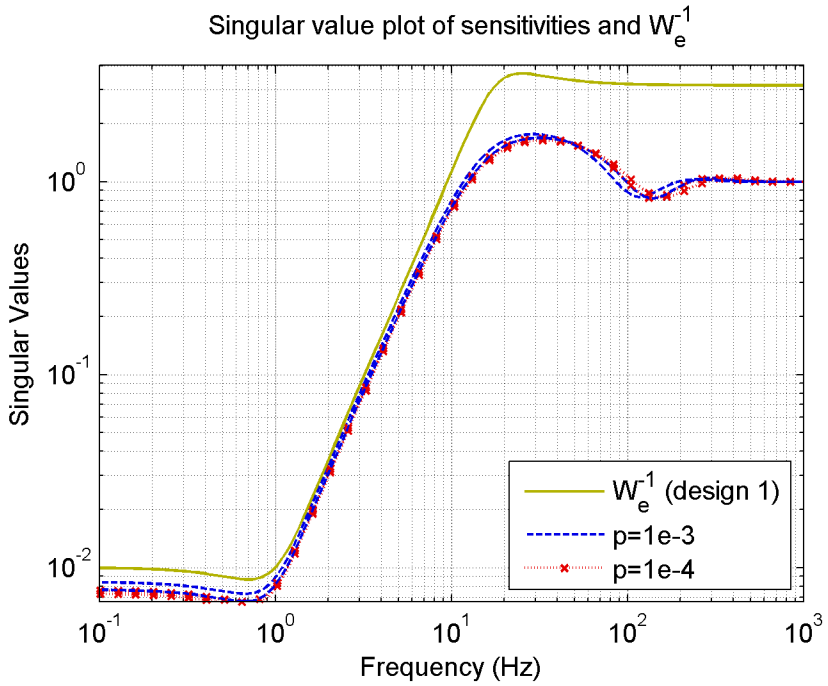

Figure 79: Singular value plot of sensitivities and W_e^{-1} for LQG/LTR design 2

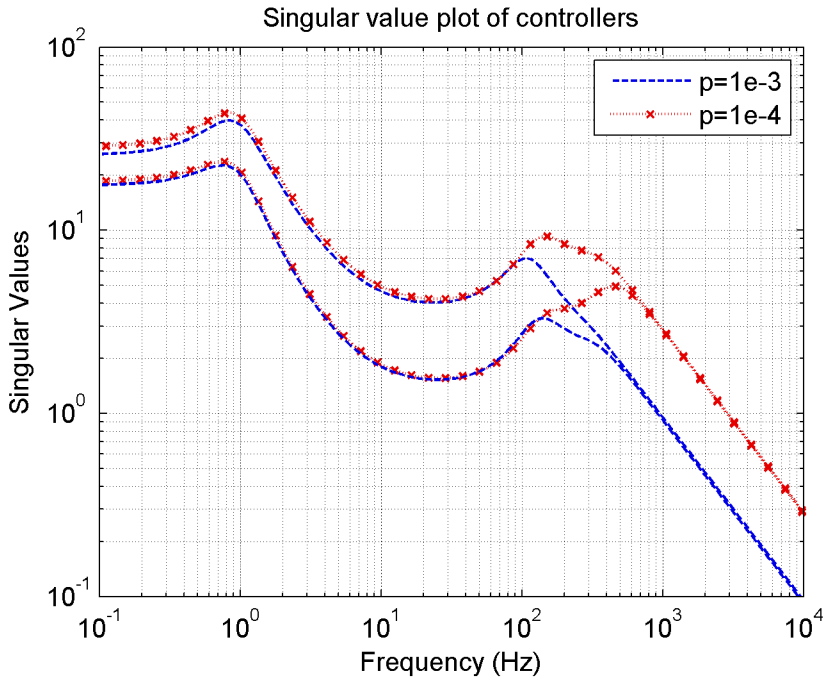

Figure 80: Singular value plot of the LQG/LTR controllers for design 2

As given in Figs. 78 and 79 the recovery procedure is made such that the design objectives of the design 1 are recovered. To do that, the weighting matrix is modified such that the bandwidth is enlarged to 15 Hz from 10 Hz, and 2.5 multiples of the dc gain is used.

7.3. $\mathcal{H}_\infty$ Design

As given in Table 4, the sensitivity weight W_e is of order 4, and the control weight W_u is of order 2. Moreover, the complementary sensitivity weigh W_t which comes from the perturbations upper bound has order of 4. On the other hand, the nominal model has order of 10. All these create a generalized plant having order of 20. In short, the $\mathcal{H}_\infty$ controller which has order of 20 will be synthesized.

The $\mathcal{H}_\infty$ controller is designed in *S*/*KS*/*T* mixed sensitivity framework as discussed in Chapter 3. For this problem, the objective is to find suboptimal controller such that Eq. (7.2) is satisfied where γ value is very close to optimal value γ_{min}.

$$\left\| \begin{bmatrix} W_e S_o \\ W_u K S_o \\ W_t T_o \end{bmatrix} \right\|_\infty < \gamma \tag{7.2}$$

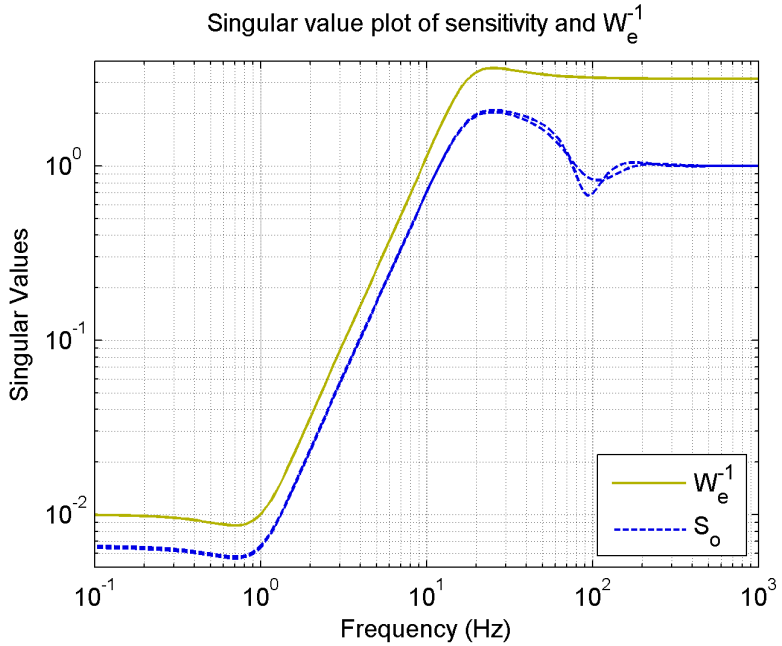

Figure 81: Singular value plot of sensitivity and W_e^{-1} for $\mathcal{H}_\infty$ design

The $\mathcal{H}_\infty$ controller with γ value of 0.68 is obtained, and resulting closed loop output sensitivity gains for nominal model are shown in Fig. 81.

7.4. μ-synthesis Design

For this problem the generalized plant has the same structure as in the case of $\mathcal{H}_\infty$ design. That is, for this problem generalized plant has an order of 20. The controller synthesized with *D-K* iteration will be of order of 20 plus the orders of *D* scaling matrices.

In our case, the uncertainty has the form given in Eq. (7.3).

$$\tilde{\boldsymbol{\Delta}} = \left\{ \text{diag}\left[\boldsymbol{\Delta}, \boldsymbol{\Delta}_p \right] : \boldsymbol{\Delta} \in \mathbb{C}^{2x2}, \boldsymbol{\Delta}_p \in \mathbb{C}^{2x4} \right\} \tag{7.3}$$

The first block corresponds to the uncertainty used in the modeling of two-axis gimbal. The second fictitious uncertainty block is used while evaluating the robust performance in the μ framework [19]. In addition, both uncertainty blocks are norm bounded.

Please observe that this $\tilde{\boldsymbol{\Delta}}$ structure is slightly different than the structure introduced in Chapter 2. In other words, the perturbations blocks are no longer square. This small modification leads to a small change in optimization procedure that is made to reduce the structural singular value upper bound. In other words, the cost function of the optimization changes to $\bar{\sigma}\left(D_l M D_r^{-1} \right)$ where D_l and D_r are the left and right scaling matrices, and they have the form given in Eqs. (7.4) and (7.5), respectively [40].

$$\boldsymbol{D}_l = \left\{ \text{diag}\left[d_1 I_{m1}, I_{m_p} \right] : d_1 \in \mathbb{R},\ d_1 > 0,\ m_1 = 2,\ m_p = 4 \right\} \tag{7.4}$$

$$\boldsymbol{D}_r = \left\{ \text{diag}\left[d_1 I_{m1}, I_{m_p} \right] : d_1 \in \mathbb{R},\ d_1 > 0,\ m_1 = 2,\ m_p = 2 \right\} \tag{7.5}$$

Then the objective during the optimization procedure reduces to find $d_1(jw)$ which will minimize the $\bar{\sigma}\left(D_l M D_r^{-1} \right)$. Next, it is desired to fit a stable and minimum phase transfer function to $d_1(jw)$. After that, the iterative procedure discussed in Chapter 2 can be used.

Iteration 1:

Iteration 1 is made by choosing *D* scaling matrices as identity with corresponding sizes, and the resulting controller will be of order 20. The resulting controller results in the following μ bounds as shown in Fig. 82. Note that the controller of the iteration 1 is actually equal to $\mathcal{H}_\infty$ controller designed in mixed sensitivity framework in Section 7.3.

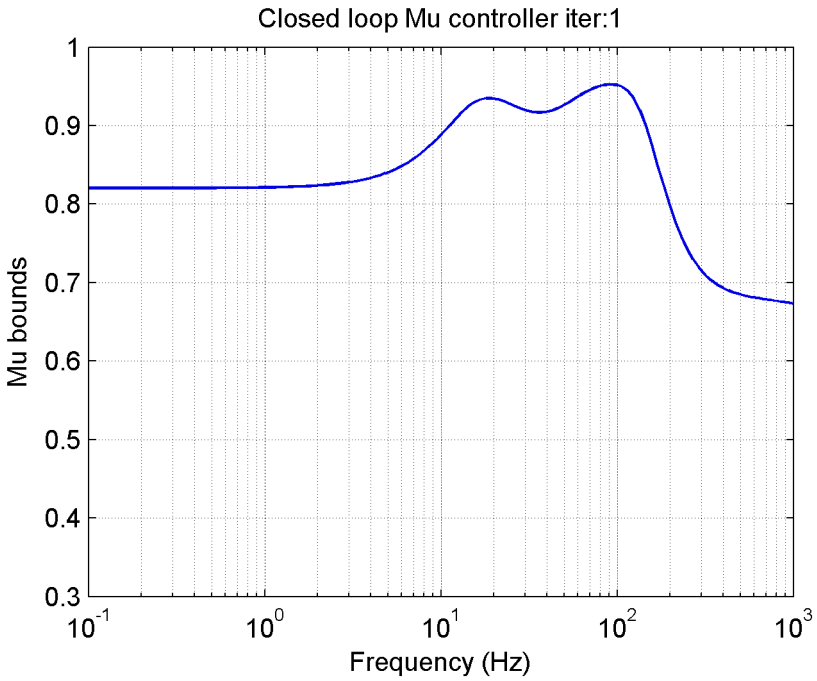

Figure 82: Closed loop μ controller iter:1

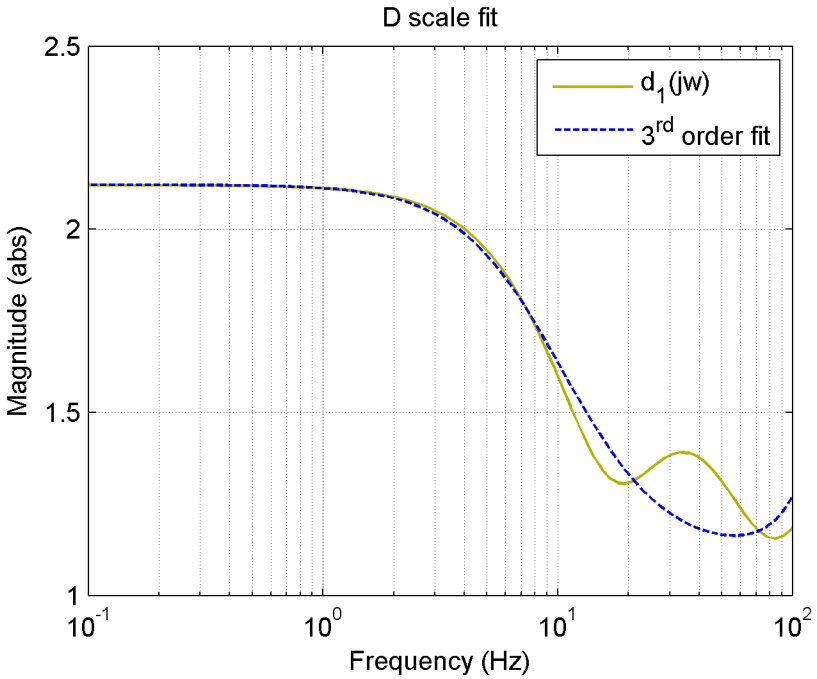

Figure 83: *D* scale fit

At first iteration during optimization, corresponding $d_1(jw)$ is obtained at different frequencies and appropriate transfer function is fitted. The $d_1(jw)$ and the fitted transfer function of order 3 is given in Fig. 83.

Note that the D scalings are of order 12 in total, and then the resulting controller in the next iteration will be order of 32.

Iteration 2:

The $\mathcal{H}_\infty$ controller is synthesized for the scaled plant and the resulting μ bounds are given in Fig. 84. The iterations are stopped at this point because the local optimum solution is found. In other words, the μ upper bound could not be minimized any more. For the nominal model, gains of the output sensitivity and weight are illustrated in Fig. 85 for two iterations.

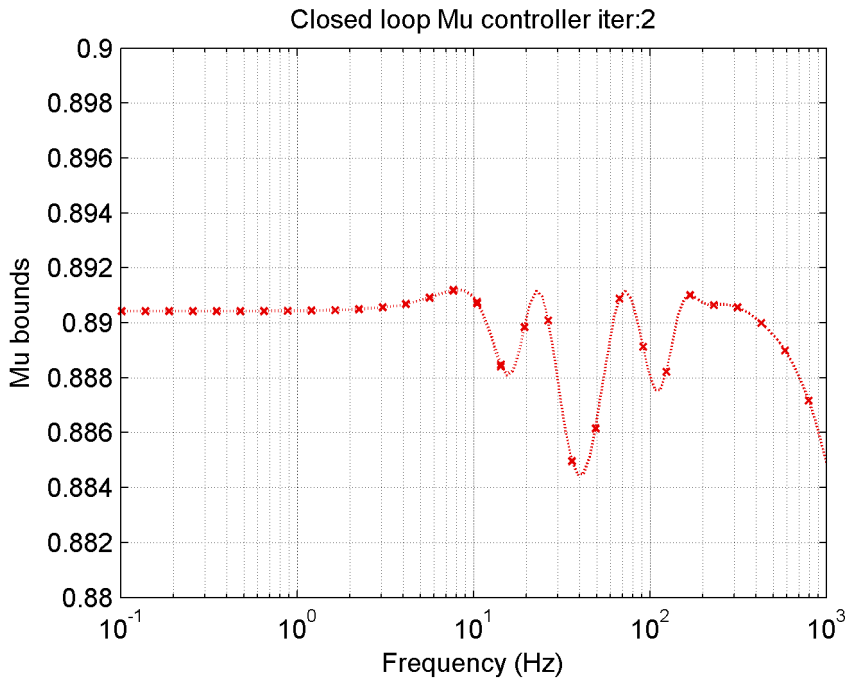

Figure 84: Closed loop μ controller iter:2

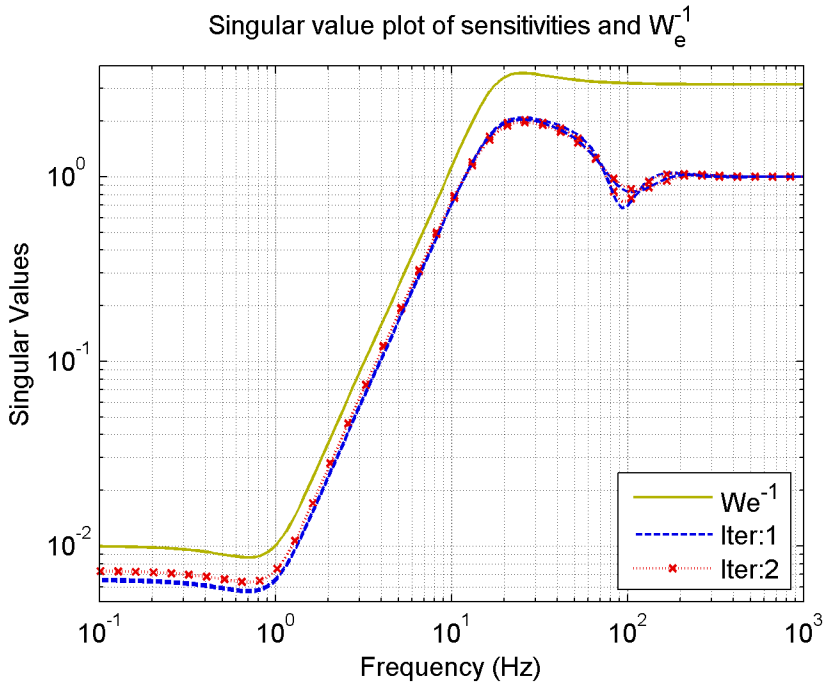

Figure 85: Singular value plot of sensitivities and W_e^{-1} for μ-synthesis

7.5. Robustness Analysis

The robustness analysis is usually performed by investigating the μ values of the closed loop system. The required μ conditions for robust stability and robust performance are discussed in Section 2.6. However, when there is only one full block perturbation in the system, and if the performance criterion is measured only by sensitivity ($\|W_e S_o\|_\infty < 1$), the robustness analysis can be done with simple singular value tests. The detailed procedure is discussed in Section 2.4. Since singular value tests are very simple compared to μ tests, in the first part of this section, the robustness is analyzed in this way. Then in the next section the robustness is discussed in μ framework and the performance criterion is changed to one given in Eq. (7.6).

$$\left\| \begin{bmatrix} W_e S_o \\ W_u K S_o \end{bmatrix} \right\|_\infty < 1 \tag{7.6}$$

7.5.1. Robustness Analysis with Singular Value Tests

The singular value tests for the structure given in Fig. 86 are summarized here as Eqs. (7.7)-(7.10).

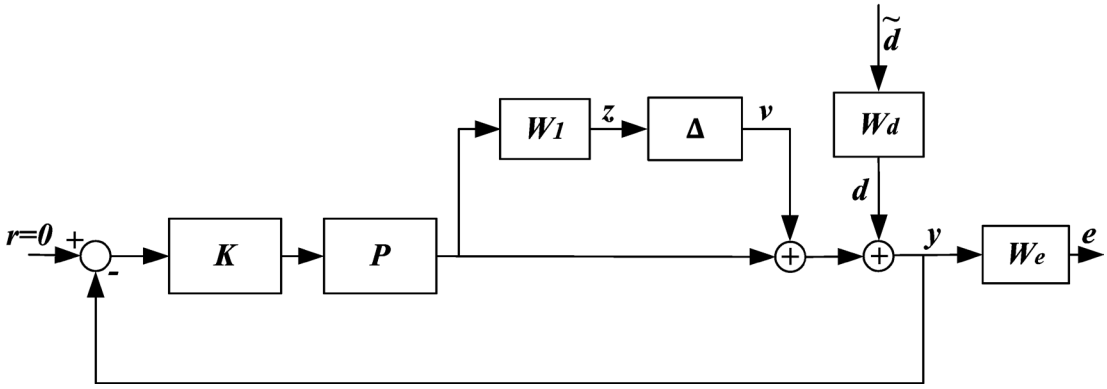

Figure 86: Output multiplicative perturbed system

$$\left\| W_e S_o \right\|_\infty < 1 \tag{7.7}$$

$$\left\| W_1 T_o \right\|_\infty < 1 \tag{7.8}$$

$$\bar{\sigma}\left(W_d\right)\bar{\sigma}\left(W_e S_o\right) + \bar{\sigma}\left(W_1 T_o\right) \le 1,\ \forall w \tag{7.9}$$

Equations (7.7)-(7.9) are the nominal performance, robust stability and robust performance singular value tests for nominally stable system respectively. In our case, W_d is taken to be identity, so the resulting robust performance test reduces to Eq. (7.10).

$$\bar{\sigma}\left(W_e S_o\right) + \bar{\sigma}\left(W_1 T_o\right) \le 1,\ \forall w \tag{7.10}$$

Now, the singular value tests are applied to three designs consecutively.

7.5.1.1. LQG/LTR Design 2

Since the recovery is not satisfied for design 1, robustness analysis is only made for design 2. In design 2 as explained in Section 7.2, the plant is augmented with modified weight and new controllers are designed. The nominal performance, robust stability and robust performance of the design 2 are shown in Figs. 87 and 88. With these controllers, nominal performance and robust stability are satisfied for both ρ values. Since the peak value of robust performance test is very close to 1, robust performance can be assumed to be satisfied for $\rho = 1e^{-4}$. For $\rho = 1e^{-3}$ the robust performance is not satisfied; however, it leads to more stable loop. In short, reducing ρ makes the performance better at the cost of reducing stability. This situation result from the high controller gains at high frequencies for small ρ as shown in Fig. 80 previously.

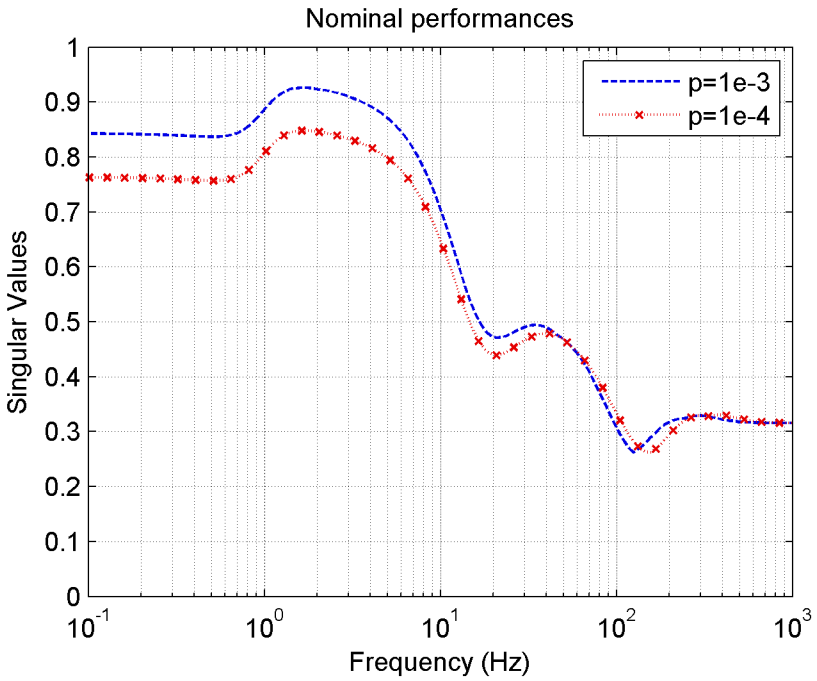

Figure 87: Nominal performances with the LQG/LTR controllers

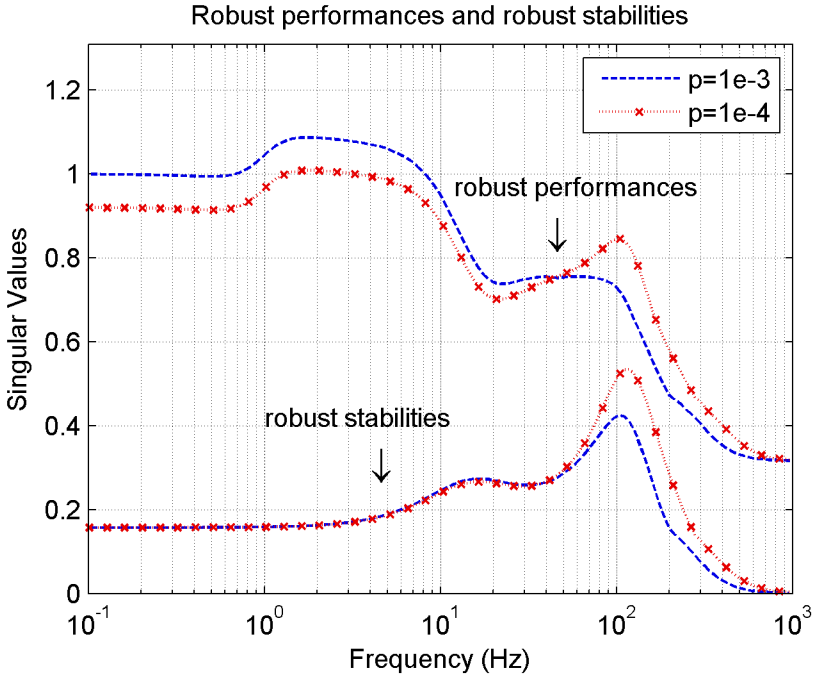

Figure 88: Robust performances and robust stabilities with the LQG/LTR controllers

7.5.1.2. $\mathcal{H}_\infty$ Design

The nominal performance, robust stability and robust performance of the closed loop of $\mathcal{H}_\infty$ design are depicted in Figs. 89 and 90. They show that the required stability and performance are satisfied.

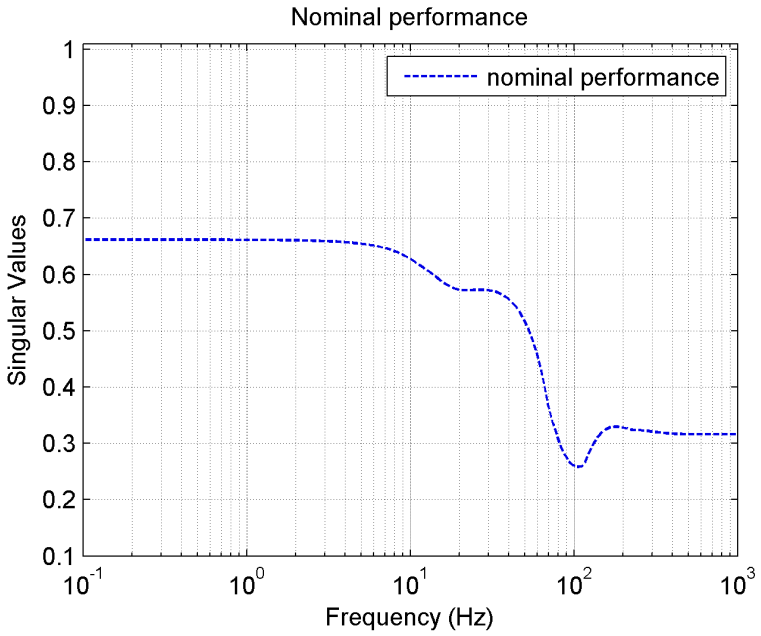

Figure 89: Nominal performance with the $\mathcal{H}_\infty$ controller

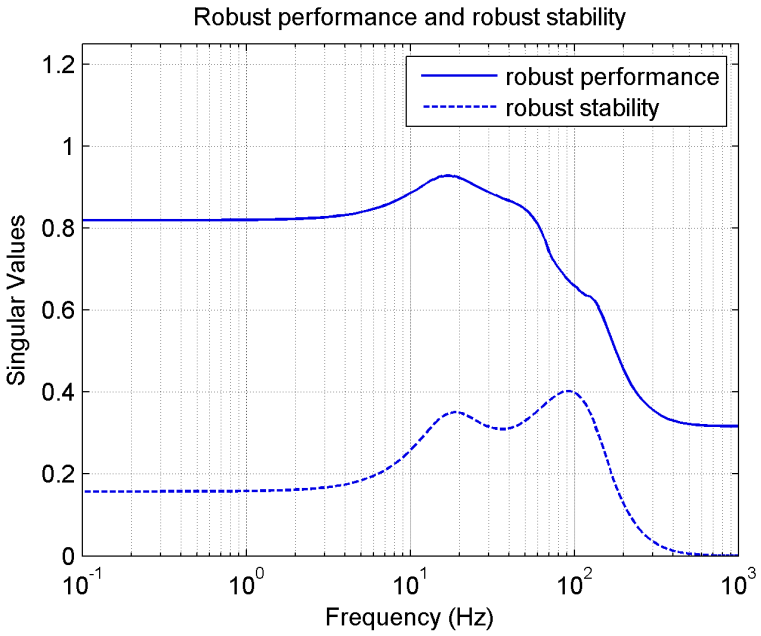

Figure 90: Robust performance and robust stability with the $\mathcal{H}_\infty$ controller

7.5.1.3. μ-synthesis Design

The nominal performance, robust stability and robust performance of the closed loops with the μ controllers are given in Figs. 91 and 92 for two iterations. They show that the required stability and performance are satisfied. Moreover, the controller at first iteration ($\mathcal{H}_\infty$ controller) has better nominal performance than the controller at next iteration. However, iteration 2 leads to smaller performance peak. In short, μ-synthesis tries to flatten the robust performance at each iteration at the cost of reducing nominal performance.

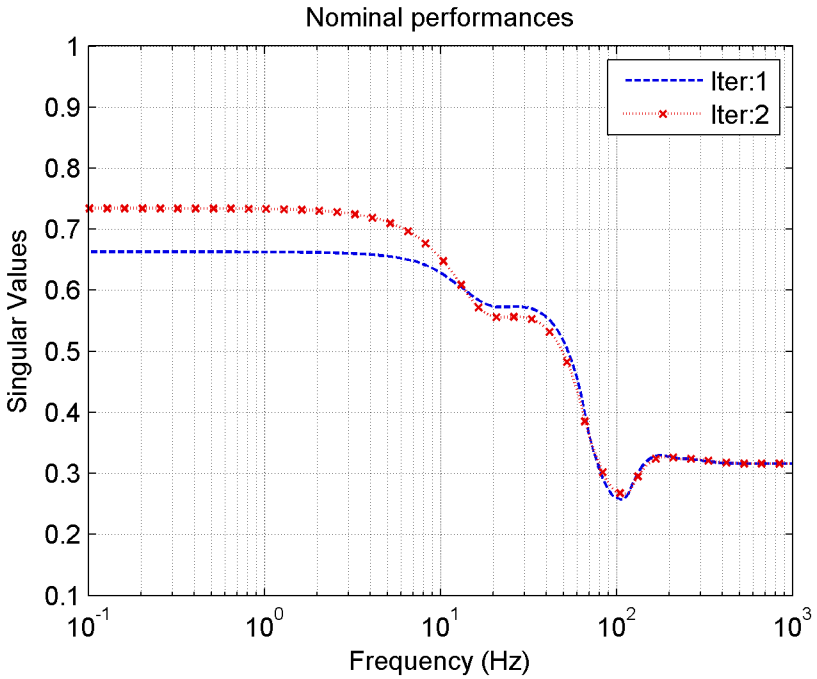

Figure 91: Nominal performances with the μ controllers

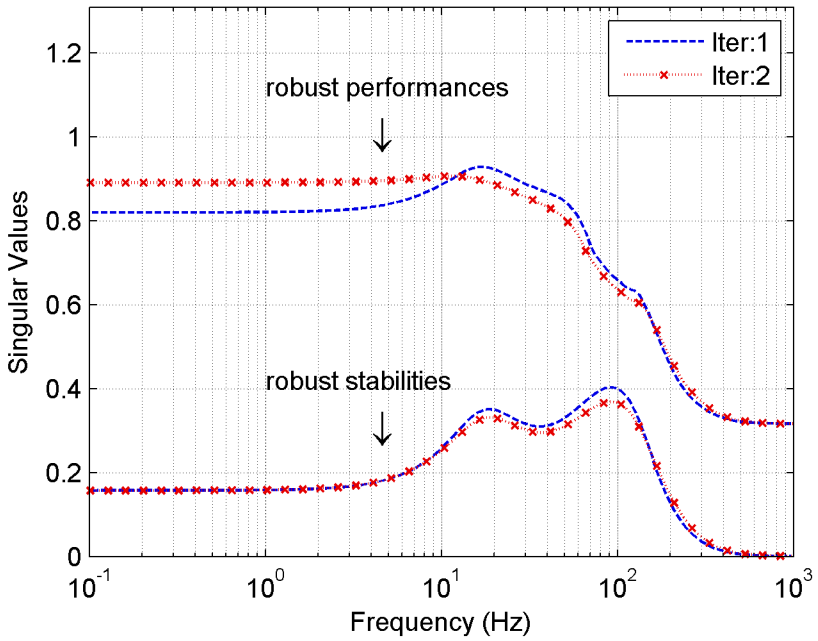

Figure 92: Robust performances and robust stabilities with the μ controllers

7.5.2. Robustness Analysis with μ Tests

The μ tests for the structure given in Fig. 93 are summarized here where $\tilde{\Delta}$ has the form represented in Eq. (7.11) and M is partitioned as in Eq. (7.12).

$$\tilde{\Delta} = \left\{ \text{diag}\left[\Delta, \Delta_p \right] : \Delta \in \mathbb{C}^{2x2}, \Delta_p \in \mathbb{C}^{2x4} \right\} \tag{7.11}$$

$$M = \begin{bmatrix} M_{11} & M_{12} \\ M_{21} & M_{22} \end{bmatrix}, \; M_{11}, M_{12} \in \mathbb{C}^{2x2}, \;\; M_{21}, M_{22} \in \mathbb{C}^{4x2} \tag{7.12}$$

$$NP \Leftrightarrow \bar{\sigma}\left(M_{22} \right) = \mu_{\Delta_p} < 1, \; \forall w \tag{7.13}$$

$$RS \Leftrightarrow \mu_{\Delta}\left(M_{11} \right) < 1, \forall w \tag{7.14}$$

$$RP \Leftrightarrow \mu_{\tilde{\Delta}}\left(M \right) < 1, \forall w \tag{7.15}$$

Equations (7.13)-(7.15) are the nominal performance, robust stability and robust performance μ tests for nominally stable system respectively. Now, the μ tests are applied to three designs consecutively.

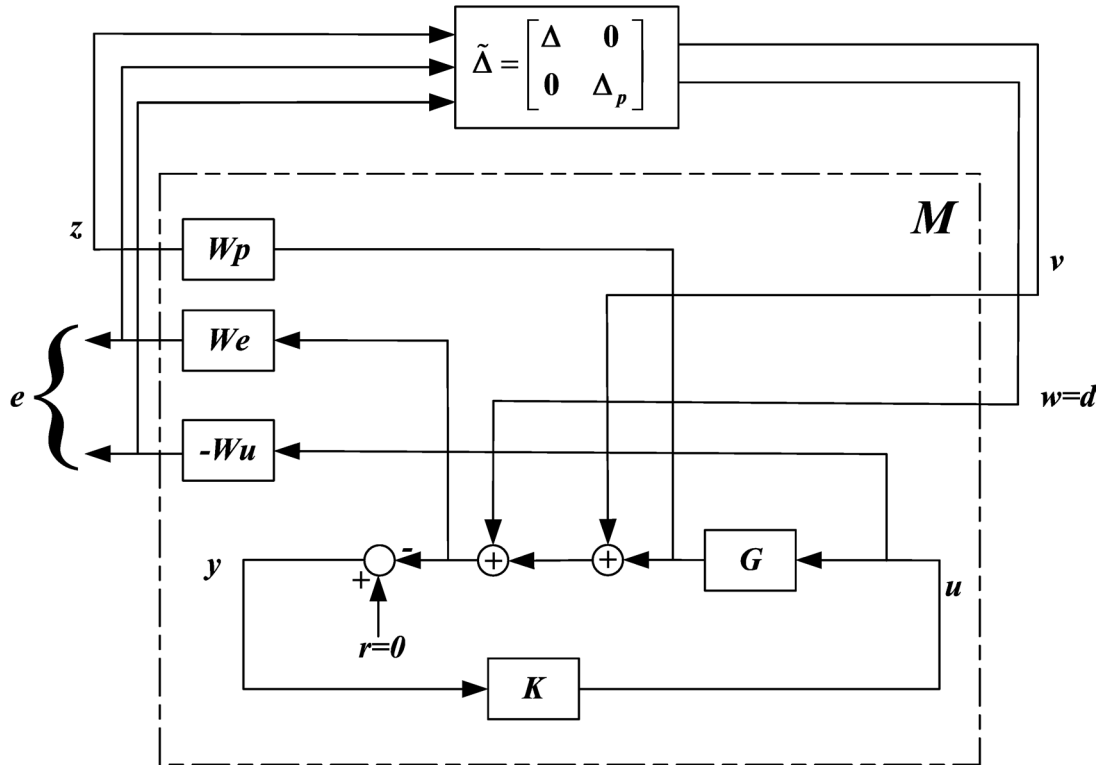

Figure 93: LFT structure for μ-analysis

7.5.2.1. LQG/LTR Design 2

The nominal performance, robust stability and robust performance of the closed loops of design 2 are depicted in Figs. 94 and 95. Note that there is no term related with control (KS_o) in the cost function of the LTR as given in Eq. (3.23). So, usually it is not expected to work well when the performance criterion is selected as in Eq. (7.6). Figures 94 and 95 show that at low frequencies robust performance is approximately satisfied for ρ = 1e^{-4}. However, at high frequencies robust performance degrades. This shows that reducing ρ leads to a controller that has higher gain at high frequencies as shown in Fig. 80.

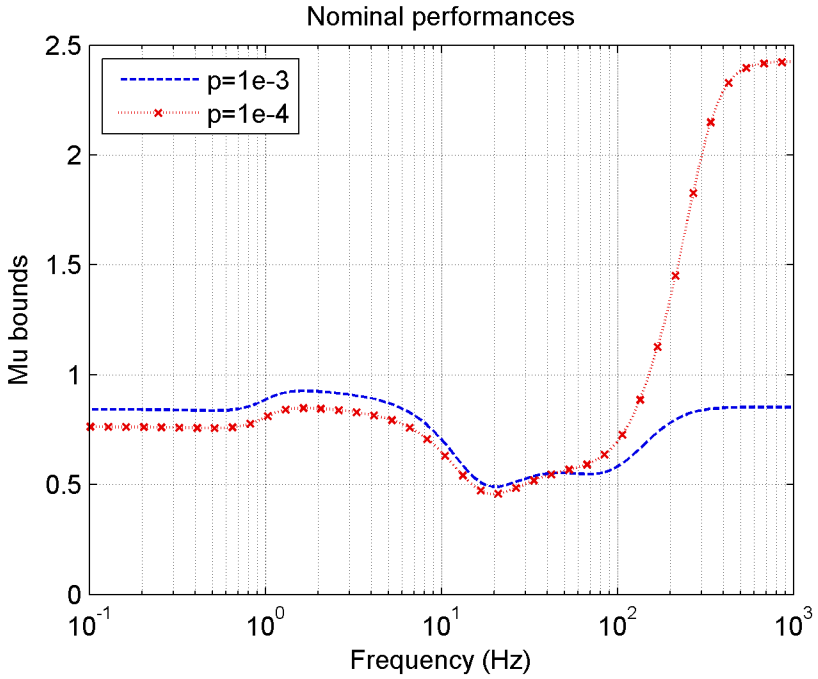

Figure 94: Nominal performances with the LQG/LTR controllers

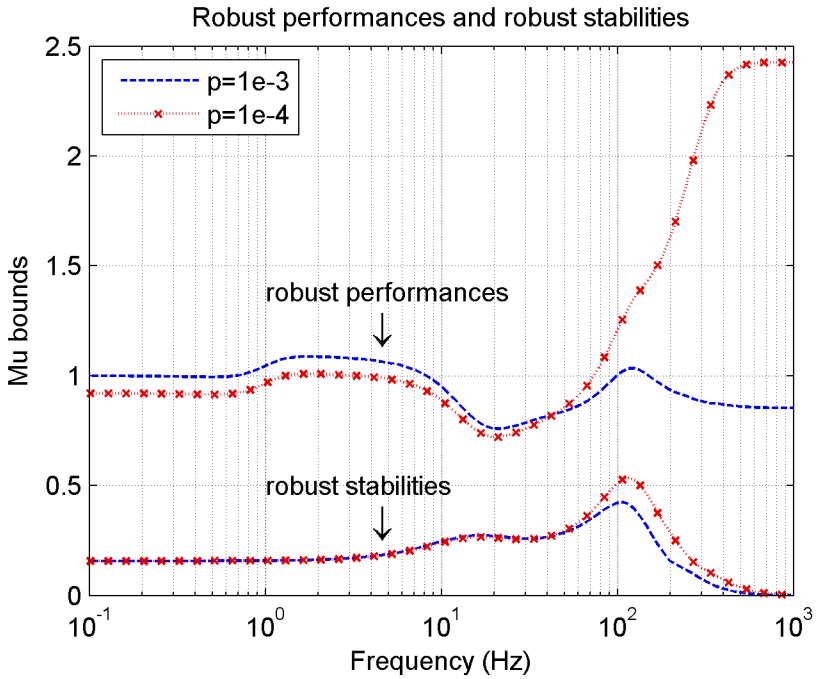

Figure 95: Robust performances and robust stabilities with the LQG/LTR controllers

7.5.2.2. $\mathcal{H}_\infty$ Design

The nominal performance, robust stability and robust performance of the closed loop of $\mathcal{H}_\infty$ design are depicted in Figs. 96 and 97. They show that the required stability and performance are satisfied.

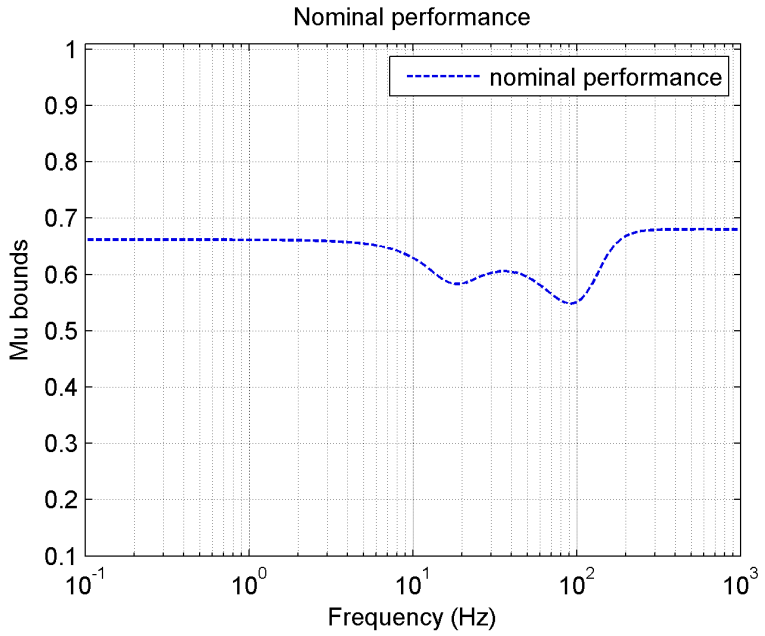

Figure 96: Nominal performance with the $\mathcal{H}_\infty$ controller

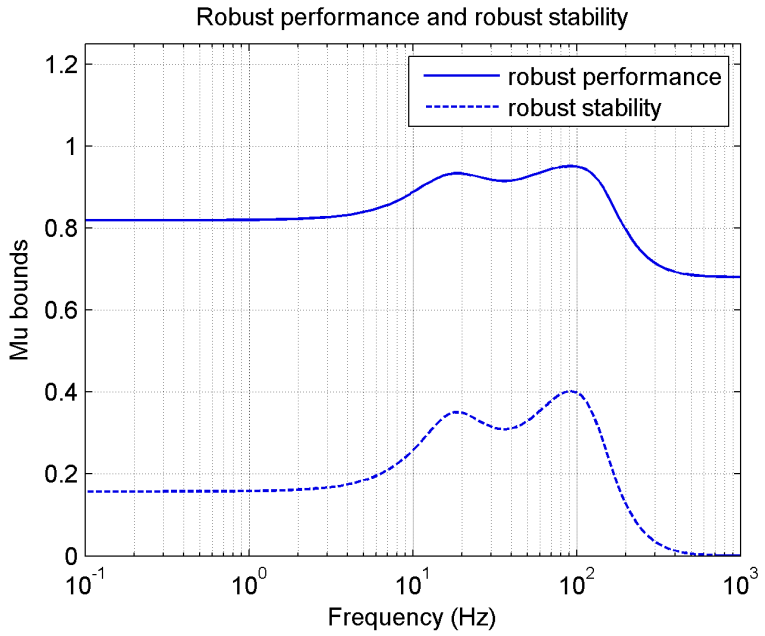

Figure 97: Robust performance and robust stability with the $\mathcal{H}_\infty$ controller

7.5.2.3. μ-synthesis Design

In Figs. 98 and 99 the nominal performance, robust stability and robust performance of the closed loops with the μ controllers are illustrated. They show that the required stability and performance are satisfied. Note that the controller at first iteration ($\mathcal{H}_\infty$ controller) tries to minimize the nominal performance; however, the μ controller (controller at next iterations) tries to minimize the peak robust performance. At each iteration, robust performance is made flatter at the cost of nominal performance reduction.

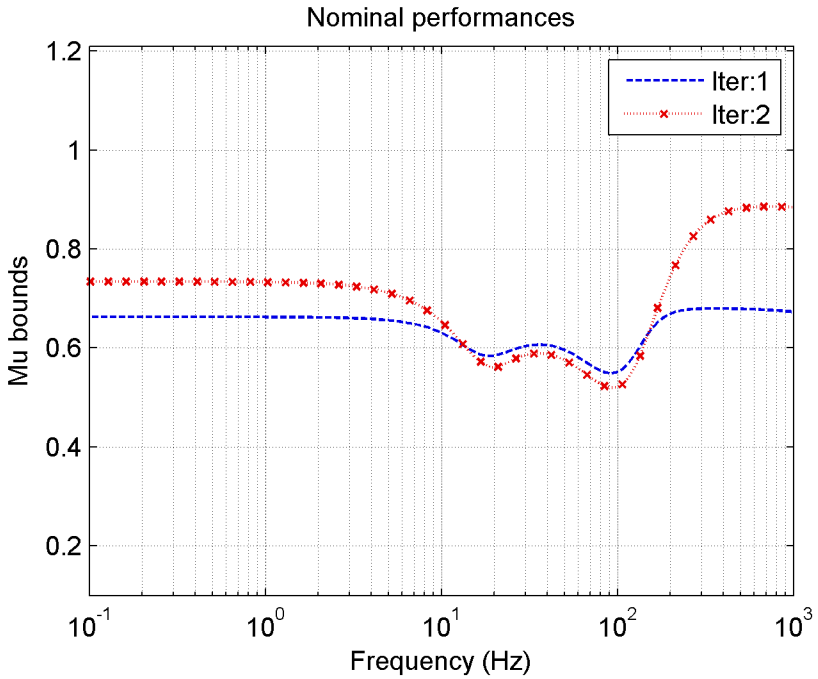

Figure 98: Nominal performances with the μ controllers

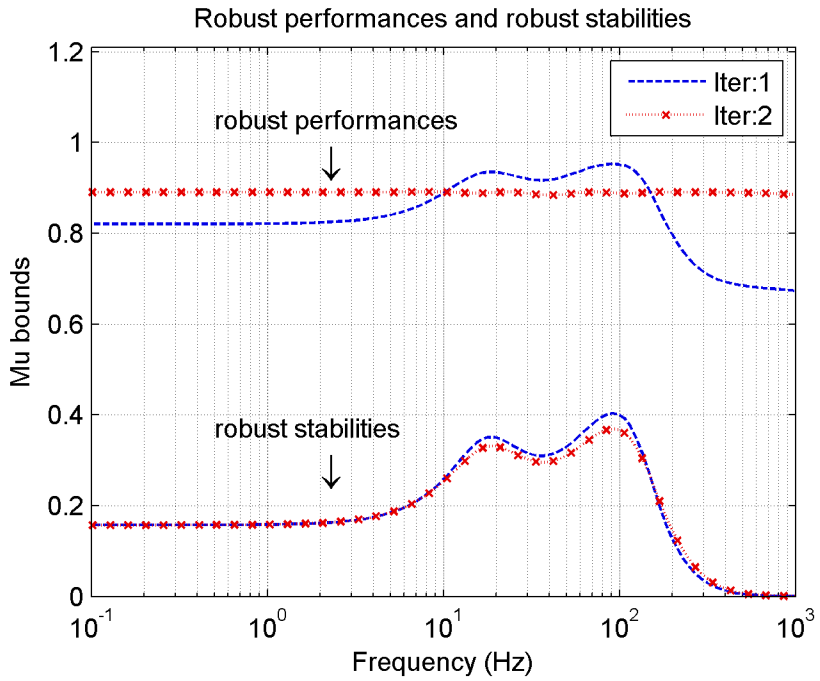

Figure 99: Robust performances and robust stabilities with the μ controllers

7.5.3. Comparison of Controllers

In this section, the performances of the three controllers are compared. The LQG/LTR controller is taken from the design 2 when ρ = 1e^{-4}. As discussed previously, the $\mathcal{H}_\infty$ controller is actually the μ controller at iteration 1. So, it is possible to compare the two controllers at two iterations in μ approach. First, the gains of the controllers are illustrated in Fig. 100. It shows that the $\mathcal{H}_\infty$ controller has larger gain at low frequencies which leads to better performance at this region. On the other hand, the LQG/LTR controller has large gain at high frequencies which reduces the stability at this region.

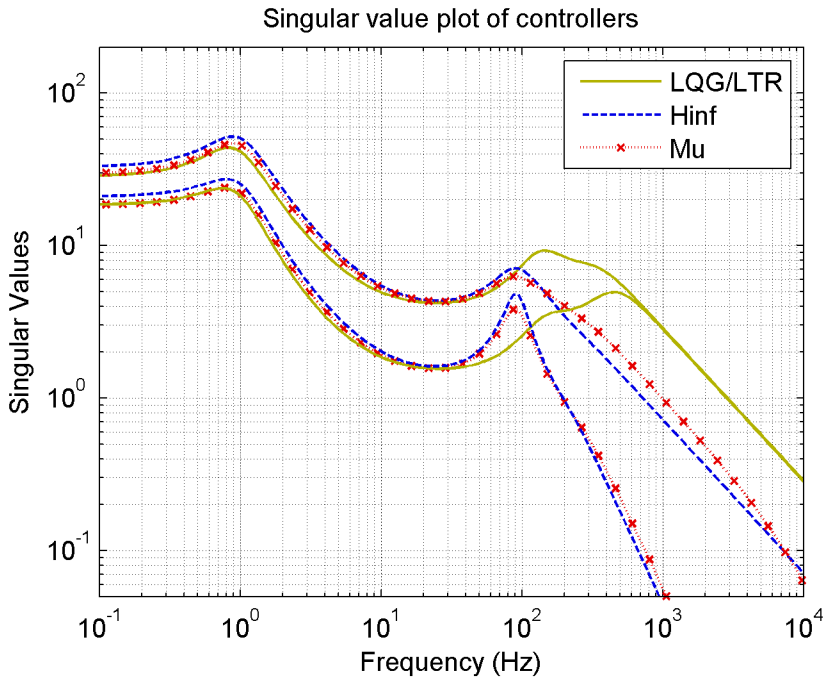

Figure 100: Singular value plot of controllers

Now, the results obtained in the previous sections are compared. First, the comparison is made by looking at singular value tests. Next, μ tests are utilized.

7.5.3.1. Robustness Comparison with Singular Value Tests

In this section, it is assumed that the structure given in Fig. 86 is considered. Then the corresponding nominal performances, robust stabilities and robust performances are depicted in Figs. 101 and 102 below with the three controllers by using the corresponding singular value tests.

7.5.3.2. Robustness Comparison with μ Tests

For the structure given in Fig. 93, the nominal performances, robust stabilities and robust performances are depicted in Figs. 103 and 104 by using the corresponding μ tests.

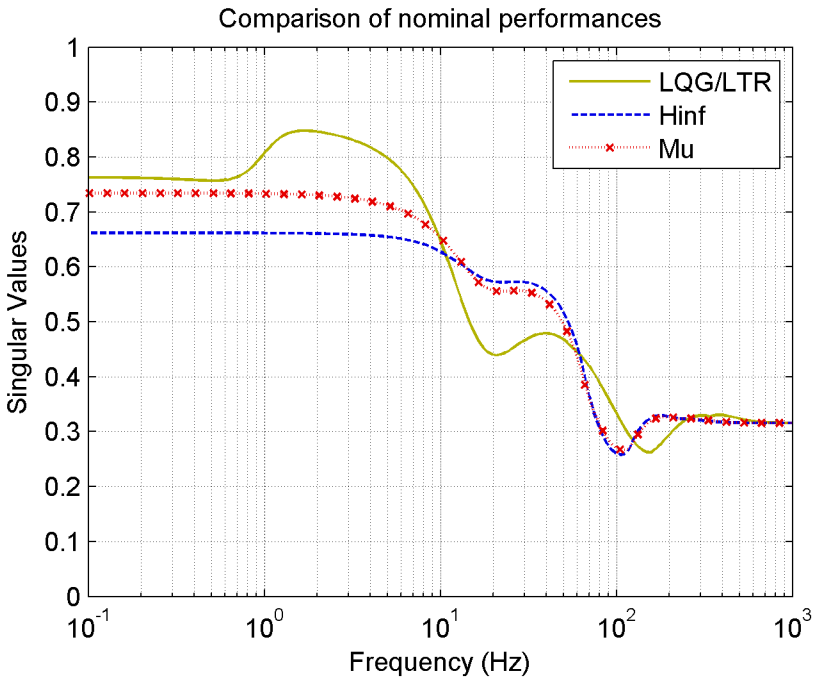

Figure 101: Comparison of nominal performances with singular value tests

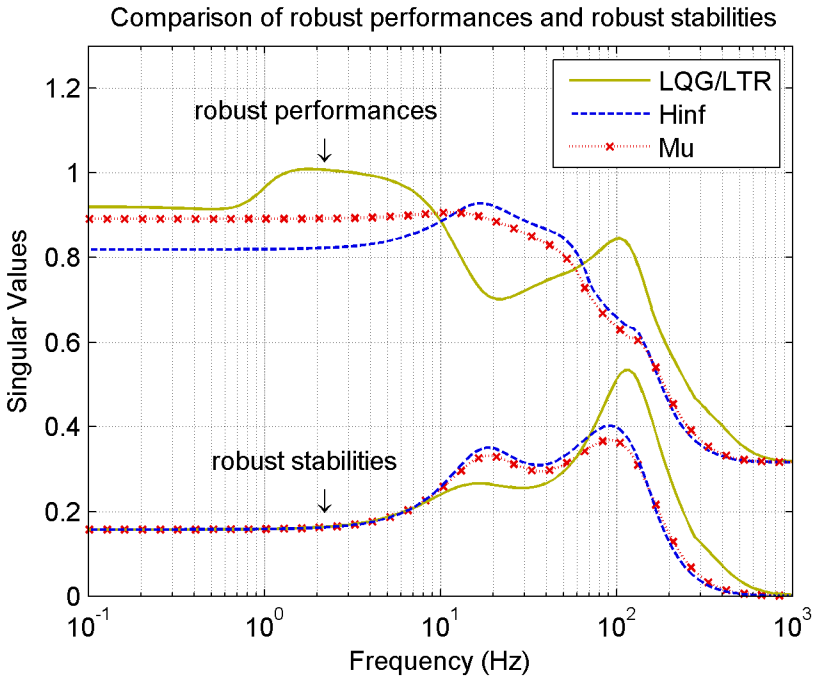

Figure 102: Comparison of robust performances and robust stabilities with singular value tests

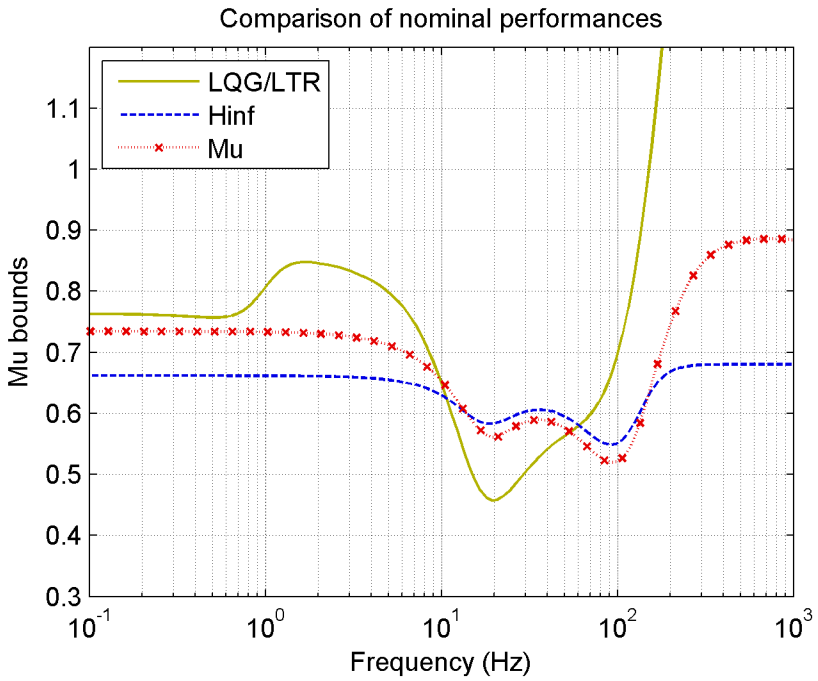

Figure 103: Comparison of nominal performances with μ tests

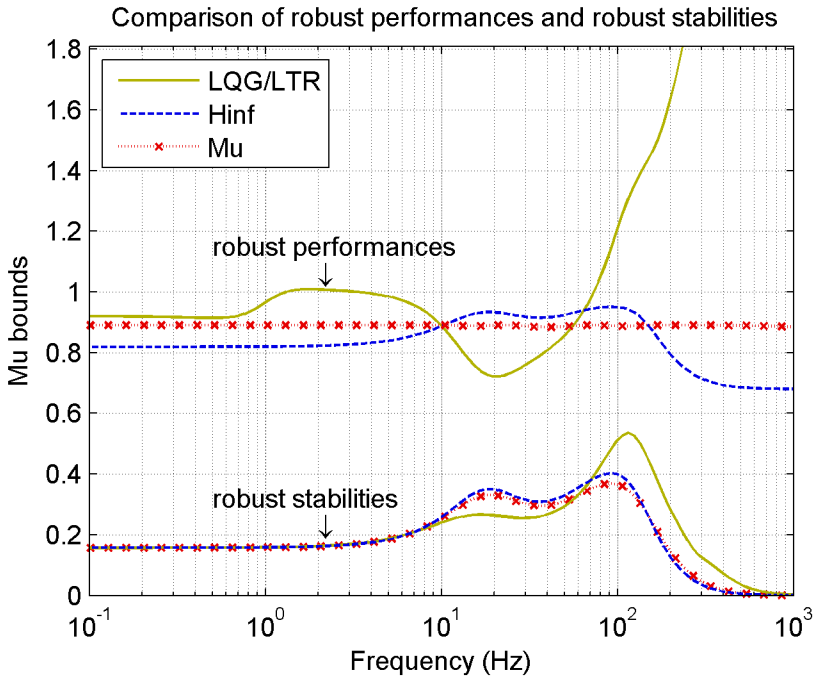

Figure 104: Comparison of robust performances and robust stabilities with μ tests

7.5.3.3. Results of the Comparisons

Figures 101-104 illustrate the following results:

The LQG/LTR controller satisfies the robust stability and performance when the performance is measured in terms of output sensitivity only. However, LTR leads to controller having large gains at high frequencies which reduces the stability at these frequencies. When the performance is measured in terms of S_o and KS_o, the robust performance reduces dramatically at high frequencies. This results from the fact that there is no term with KS_o in the LTR cost function.

The $\mathcal{H}_\infty$ controller satisfies the robust stability and performance for both structures. In low frequency region it has the best performance. However, at mid frequencies the μ controller has better performance than $\mathcal{H}_\infty$ controller.

When the $\mathcal{H}_\infty$ controller is considered as the μ controller at iteration 1, it is observed that *D-K* iteration tries to find a controller that minimizes the peak of the robust performance. In other words, at each iteration, μ of the closed loop gets flatter. However, this procedure achieves that by reducing the nominal performance.

Briefly, when the performance at low frequencies is important one can use the $\mathcal{H}_\infty$ controller. On the other hand, the performance over all frequencies is essential the μ controller should be chosen. When performance is only measured by weighted output sensitivity, the LQG/LTR controller can be used; however, it has the poorest stability. So, LQG/LTR controller must be the third choice.

7.6. Summary

Firstly, in this chapter the LQG/LTR, $\mathcal{H}_\infty$ and μ controllers are synthesized. Secondly, the nominal performances, robust stabilities and robust performances of the closed loops with these three controllers are investigated. Finally, the three controllers are compared and observations about their properties are summarized.

CHAPTER 8

IMPLEMENTATION AND EXPERIMENTAL RESULTS

In this chapter, how the designed controllers are implemented is discussed. Firstly, since the designed controllers have high order, reduced order controllers are found using Balanced Truncation method. Next, the reduced order controllers are discretized so that they can be implemented in digital computer. After that, the experimental closed loop transfer matrices are depicted. The chapter ends with the investigation of experimental performances of the system at different conditions.

8.1. Implementation

In this section, the motivation of the controller reduction is expressed. Next, discretization of the controllers is discussed.

8.1.1. Controller Reduction

The design methods discussed throughout the thesis all create complex high order controllers. For example, the LQG/LTR controller is of order 14, $\mathcal{H}_\infty$ controller is of order 20, and the μ controller is of order 32 as discussed in Chapter 7. However, the implementations of these high order controllers are difficult task. Apart from that, they lead to high process cost and poor reliability in the system. In this aspect, the lower order controller is always favorable by the control designers. In this section, how to obtain a low order controller is briefly discussed.

For this section let the original controller has a state space representation given in Eq. (8.1),

$$G(s) = \left[\begin{array}{c|c} A & B \\ \hline C & D \end{array}\right] \tag{8.1}$$

where $A \in \mathbb{R}^{n x n}$, $B \in \mathbb{R}^{n x m}$, $C \in \mathbb{R}^{p x n}$, $D \in \mathbb{R}^{p x m}$ and [A, B, C] is minimal realization. Moreover, let the reduced order controller G_r is represented with Eq. (8.2),

$$G_r(s) = \left[\begin{array}{c|c} A_r & B_r \\ \hline C_r & D_r \end{array}\right] \tag{8.2}$$

where $A_r \in \mathbb{R}^{rxr}$, $B_r \in \mathbb{R}^{rxm}$, $C_r \in \mathbb{R}^{pxr}$, $D_r \in \mathbb{R}^{pxm}$ and $r < n$ is satisfied.

Then the objective is to find a reduce order controller that minimizes the cost in Eq. (8.3).

$$\left\| G - G_r \right\|_\infty \tag{8.3}$$

There are various model reduction methods [40]; however, in this thesis Balanced Truncation method is investigated.

8.1.1.1. Balanced Model

A stable system $G(s)$ is called balanced if the solutions P and Q of Lyapunov Eqs. (8.4) and (8.5) have the form given in Eq. (8.6).

$$AP + PA^T + BB^T = 0 \tag{8.4}$$

$$A^T Q + QA + C^T C = 0 \tag{8.5}$$

$$P = Q := \sum = \text{diag}(\sigma_1, \sigma_2, \ldots, \sigma_n) \text{ with } \sigma_1 \geq \sigma_2 \geq \cdots \geq \sigma_n \geq 0 \tag{8.6}$$

In other words, the system is balanced if the controllability and observability Grammians P and Q are equal and diagonal. Moreover, σ_i is named as i^{th} Hankel singular value of the system [40].

8.1.1.2. Balanced Truncation Method

This method is based on neglecting the less observable or/and less controllable part of the original model. By doing that, important dynamics of the original model can be kept. However, in some models a mode can be weakly observable but highly controllable, or vice versa [40]. Therefore, before applying truncation, the balanced realization of the model needs to be found via state transformation.

It is shown in [41] that the system represented with Eq. (8.1) can be put into balanced form via an invertible state transformation $T \in \mathbb{R}^{nxn}$ such that Eq. (8.7) is satisfied. It also shows that the balanced realization can be partitioned as in Eq. (8.8).

$$\left[\begin{array}{c|c} A_{BAL} & B_{BAL} \\ \hline C_{BAL} & D_{BAL} \end{array}\right] = \left[\begin{array}{c|c} T^{-1}AT & T^{-1}B \\ \hline CT & D \end{array}\right] \tag{8.7}$$

$$\left[\begin{array}{c|c} A_{BAL} & B_{BAL} \\ \hline C_{BAL} & D_{BAL} \end{array}\right] = \left[\begin{array}{cc|c} A_r & A_{12} & B_r \\ A_{21} & A_{22} & B_2 \\ \hline C_r & C_2 & D_r \end{array}\right] \tag{8.8}$$

Then truncating the *n-k* least controllable-observable states leads to reduced order model given in Eq. (8.9). It is further reported in [41] that the reduced model is stable, minimal and balance with Grammians in Eq. (8.10) [42].

$$G_r(s) = \left[\begin{array}{c|c} A_r & B_r \\ \hline C_r & D_r \end{array}\right] = C_r\left(Is - A_r\right)^{-1} B_r + D_r \tag{8.9}$$

$$\Sigma_{BAL} = \mathrm{diag}(\sigma_1, \sigma_2, \ldots, \sigma_r) \tag{8.10}$$

The calculation of state transformation $T \in \mathbb{R}^{nxn}$ can be found using the state space balancing algorithm developed in [43]. Since this balancing algorithm is beyond the scope of this thesis, the details are not discussed further. In this thesis, the build in function of MATLAB is used to find the balanced realization of controllers.

It is reported in [44] that the error of the truncated model satisfies Eq. (8.11).

$$\left\|G - G_r\right\|_\infty < 2\sum_{i=r+1}^{m} \sigma_i, \forall w \tag{8.11}$$

So, in model truncation method, one can select *r* such that $\sigma_r \gg \sigma_{r+1}$ is satisfied. Even if this model gives freedom in selecting controller order, the control designer should always look at the stability and performance properties of the closed loop formed with reduced order controller [40].

8.1.1.3. Truncation of the Designed Controller

In this section, the model reductions of the designed controllers in Chapter 7 are made using the Truncation method.

8.1.1.3.1. LQG/LTR Design

First, the balanced realization of the designed LQG/LTR controller is obtained. Next, the Hankel singular values are investigated. The LQG/LTR controller is of order 14, so 14 Hankel singular values are plotted in Fig. 105. It shows that the first 12 Hankel singular values are significantly larger than the remaining two. That is, truncating last 2 states is appropriate which results in 12th order controller. The original (full order) and truncated

(reduced order) controller are depicted in Fig. 106. The robustness comparison of the closed loops is investigated for the LFT structure given in Fig. 93 in μ framework. Figures 106 and 107 show that the full and reduced order controllers show nearly the same performance and stability properties.

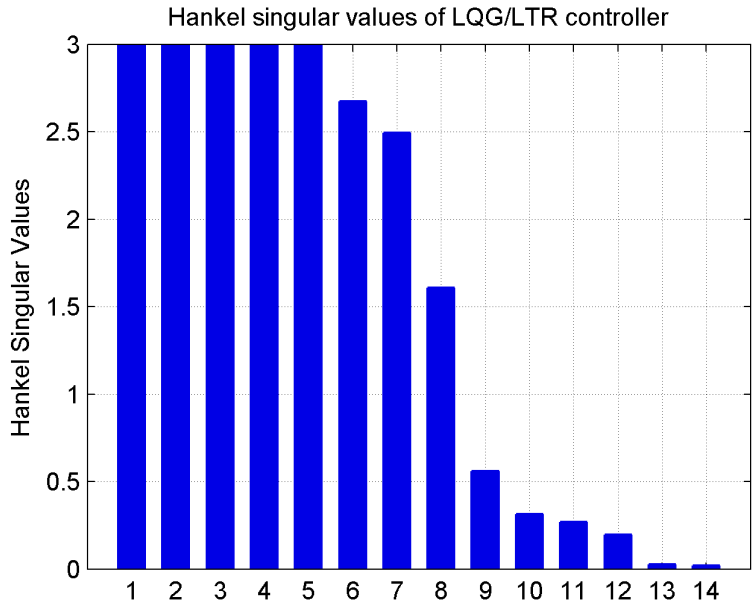

Figure 105: Hankel singular values of full order LQG/LTR controller

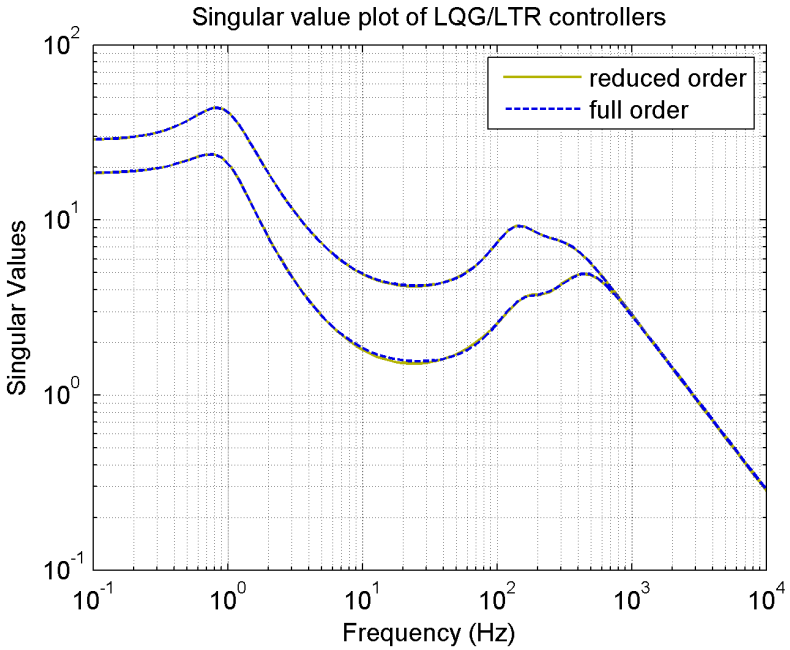

Figure 106: Singular value plot of full and reduced order LQG/LTR controllers

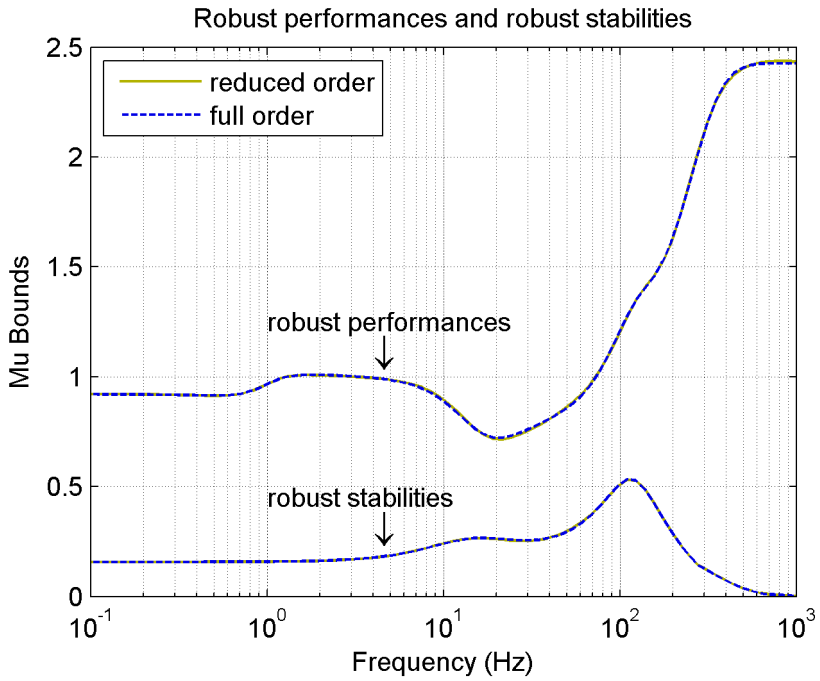

Figure 107: Robust performances and robust stabilities with full and reduced order LQG/LTR controllers

8.1.1.3.2. $\mathcal{H}_\infty$ Design

The same procedure outlined for LQG/LTR case is reconsidered. The designed $\mathcal{H}_\infty$ controller is of order 20, and corresponding Hankel singular values are shown in Fig. 108. It shows that the first 10 singular values are correspondingly larger than remaining ones. However, as in the LQG/LTR case the controller which has order of 12 is selected, and remaining 8 states are truncated. Then full and reduced order controllers and stabilities and performances with these controllers are illustrated in Figs. 109 and 110, respectively.

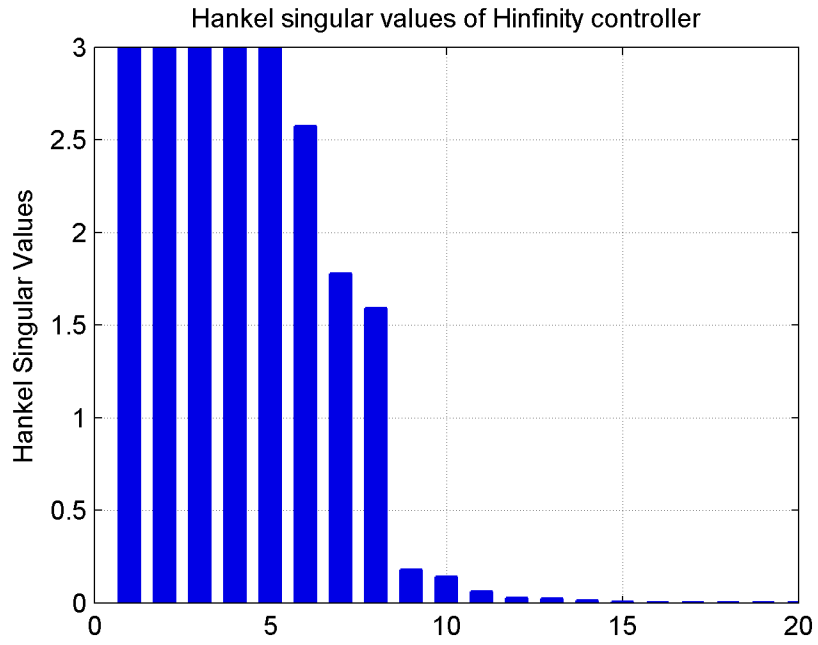

Figure 108: Hankel singular values of full order $\mathcal{H}_\infty$ controller

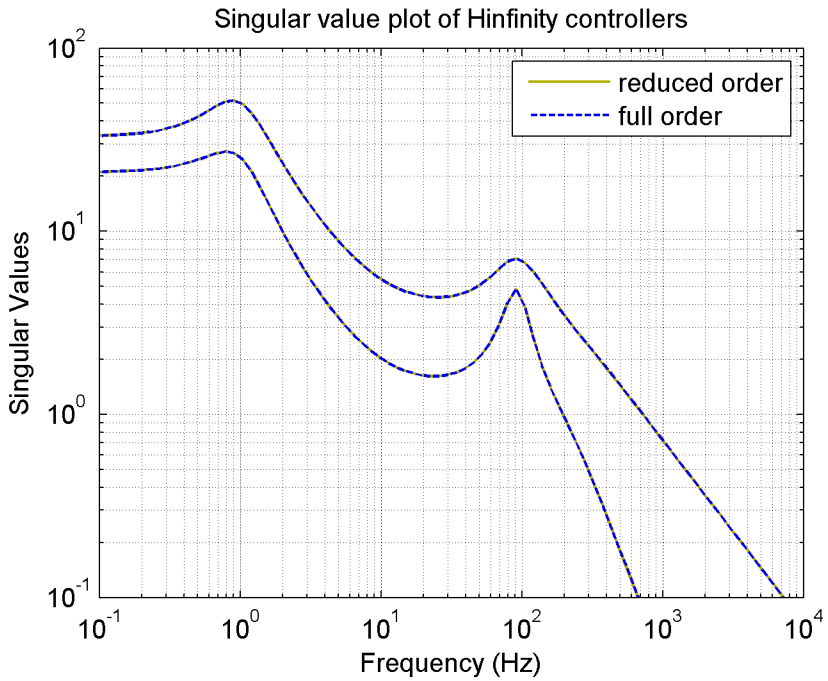

Figure 109: Singular value plot of full and reduced order $\mathcal{H}_\infty$ controllers

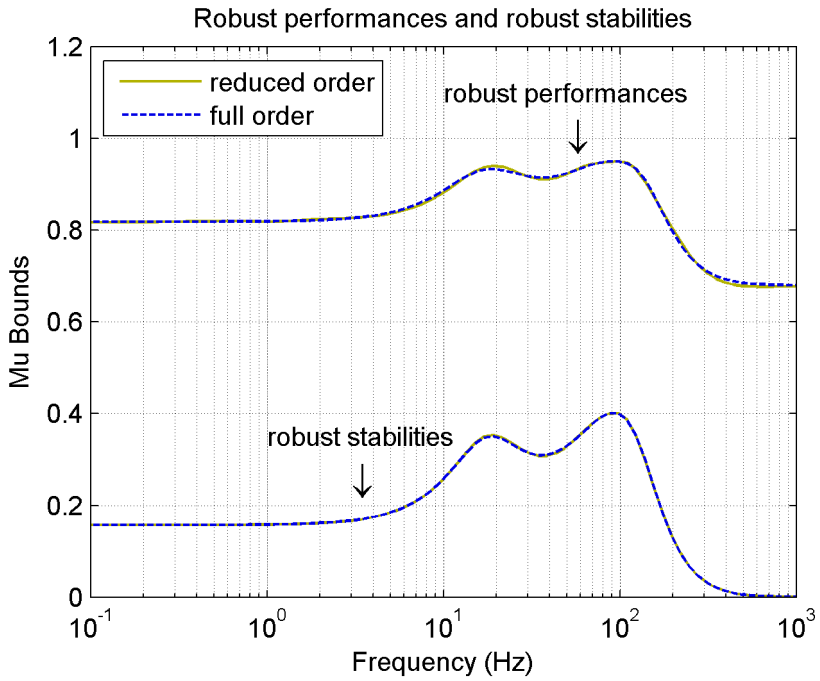

Figure 110: Robust performances and robust stabilities with full and reduced order $\mathcal{H}_\infty$ controllers

8.1.1.3.3. μ-synthesis Design

The designed μ controller is of order 32 and its Hankel singular values are given in Fig. 111. By truncating 20 states, reduced order controller having 12 states is obtained. Full and reduced order μ controllers and robustness of corresponding loops are illustrated in Figs. 112 and 113.

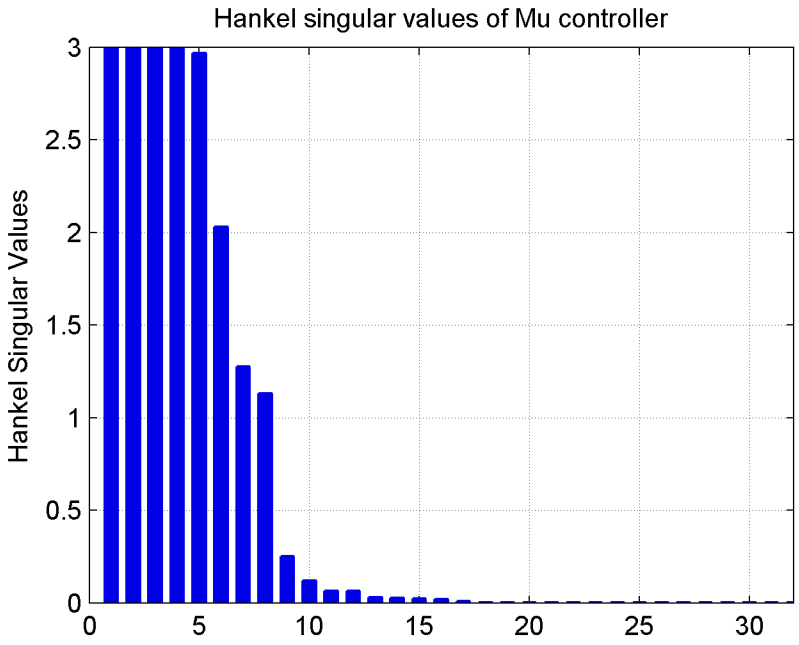

Figure 111: Hankel singular values of full order μ controller

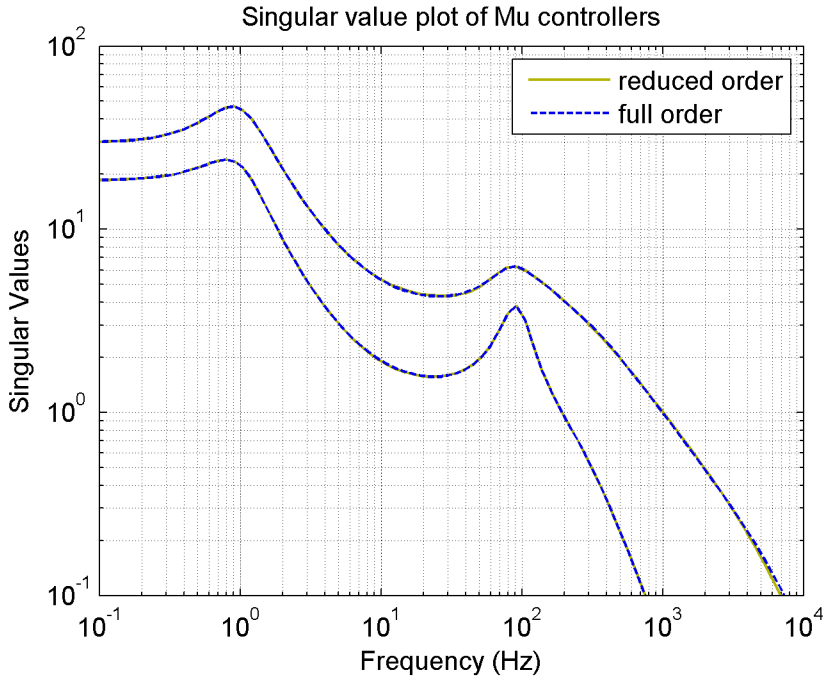

Figure 112: Singular value plot of full and reduced order μ controllers

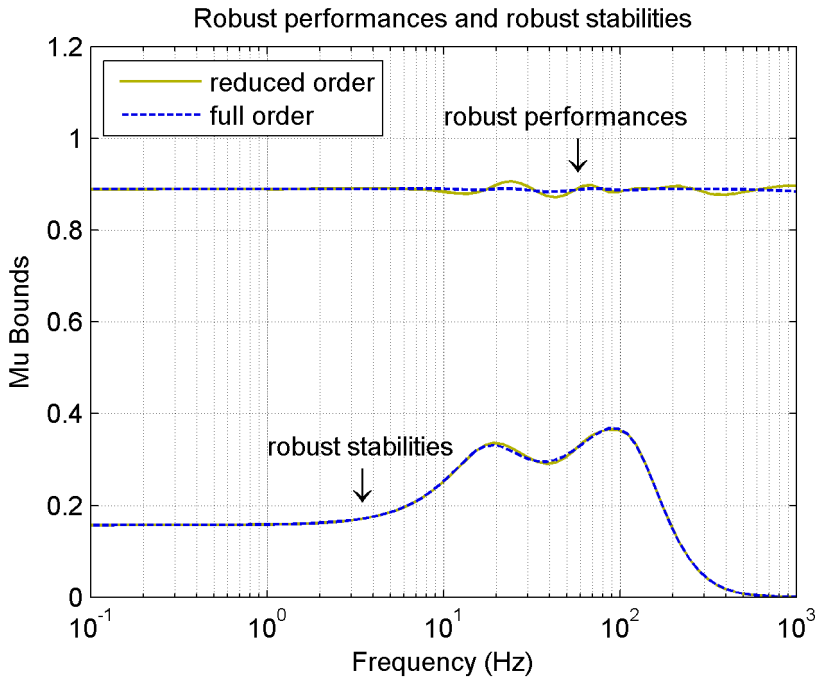

Figure 113: Robust performances and robust stabilities with full and reduced order μ controllers

8.1.1.3.4. Summary of the Model Truncation

In this section, the designed controllers and their reduced order models are obtained. The original controller orders were 14, 20 and 32 for the LQG/LTR, $\mathcal{H}_\infty$ and μ cases respectively. All the models are truncated such that they are of order 12. All the performances and stabilities given in this section show that the reduced and full order models possess very similar properties. To conclude, reduced order controllers can be used instead of full orders without hesitation.

8.1.2. Discretization with Bilinear Transform

In this section, the discretization of the continuous controller is discussed. In this thesis, bilinear transform which is a common discretization method is used. The bilinear transform results from the trapezoidal approximation of integral.

Let the continuous and discrete time controller be denoted by $G(s)$ and $G_{bt}(z)$ respectively. Then the state space matrices in Eq. (8.12) of discretized controller is obtained by using Eq. (8.13) as explained in appendix A in detail. The state space

formulas are valid if $T_s/2$ is not an eigenvalue of A where T_s denotes the sampling time of the system [45].

$$G(s)=\left[\begin{array}{c|c} A & B \\ \hline C & D \end{array}\right] \Rightarrow G_{bt}(z)=\left[\begin{array}{c|c} A_{bt} & B_{bt} \\ \hline C_{bt} & D_{bt} \end{array}\right] \tag{8.12}$$

$$\begin{aligned} A_{bt} &= \left(I - A\frac{T_s}{2}\right)^{-1}\left(I + A\frac{T_s}{2}\right) \\ B_{bt} &= \left(I - A\frac{T_s}{2}\right)^{-1} B\frac{T_s}{2} \\ C_{bt} &= C\left(I + A_{bt}\right) \\ D_{bt} &= D + CB_{bt} \end{aligned} \tag{8.13}$$

8.2. Experimental Results

In this section, the experimental results are depicted. Previously in this chapter, the reduced order controllers were obtained and they were discretized. Firstly, using these discretized reduced order controllers responses of the closed loop sensitivities are found. Then using these responses, the transfer matrices are constructed. After that, using these matrices, experimental performances are derived and illustrated.

In Chapter 2, the output was given as in Eq. (8.14).

$$y = T_o\left(r - n\right) + S_o P d_i + S_o d \tag{8.14}$$

Moreover, it was assumed in Chapter 3 that the reference r, noise n and input disturbance d_i are zero. The only external signal was assumed to be output disturbance d. Then Eq. (8.14) simplifies to Eq. (8.15) for two-axis gimbal.

$$\begin{bmatrix} w_{az} \\ w_{el} \end{bmatrix} = \begin{bmatrix} So_{11} & So_{12} \\ So_{21} & So_{22} \end{bmatrix} \begin{bmatrix} d_{az} \\ d_{el} \end{bmatrix} \tag{8.15}$$

By making d_{el} zero, So_{11} and So_{21} are determined by looking at w_{az} and w_{el} respectively. Similarly, under zero d_{az}, So_{12} and So_{22} are found. After finding responses of corresponding transfer functions, for two-input two-output system transfer matrix is constructed. Then the singular values of the sensitivity matrix are plotted. The results are now illustrated for different controllers successively. In this part by changing disturbance inputs, different perturbations are obtained which roughly yield the same input excitation

levels at low frequencies that are used while determining uncertainty upper bounds in Chapter 6.

8.2.1. LQG/LTR Design

First, the responses of So_{11}, So_{12}, So_{21} and So_{22} of the closed loop system constructed with the LQG/LTR controller are depicted in Figs. 114-117. Next, for MIMO system the singular values of S_o are given in Fig. 118.

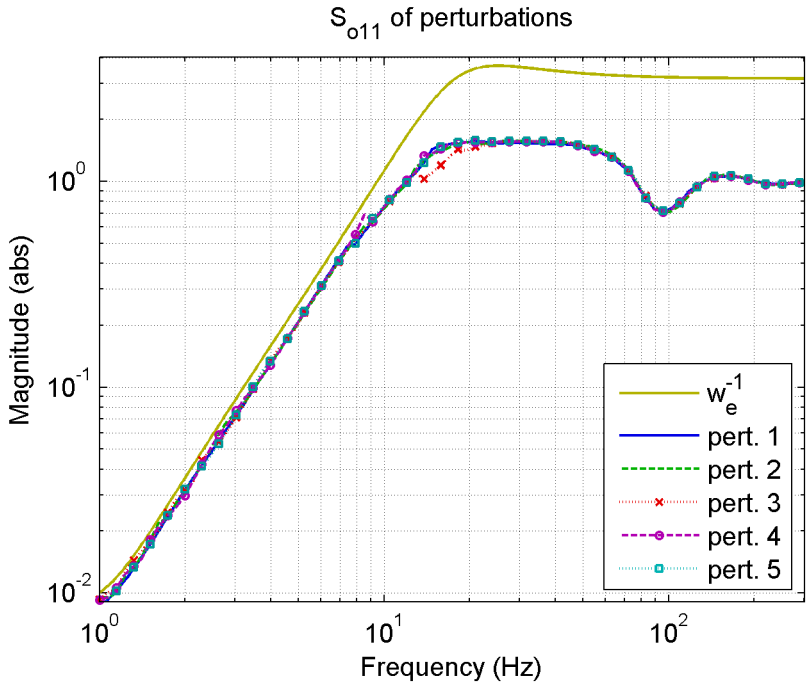

Figure 114: So_{11} of perturbations with the LQG/LTR controller

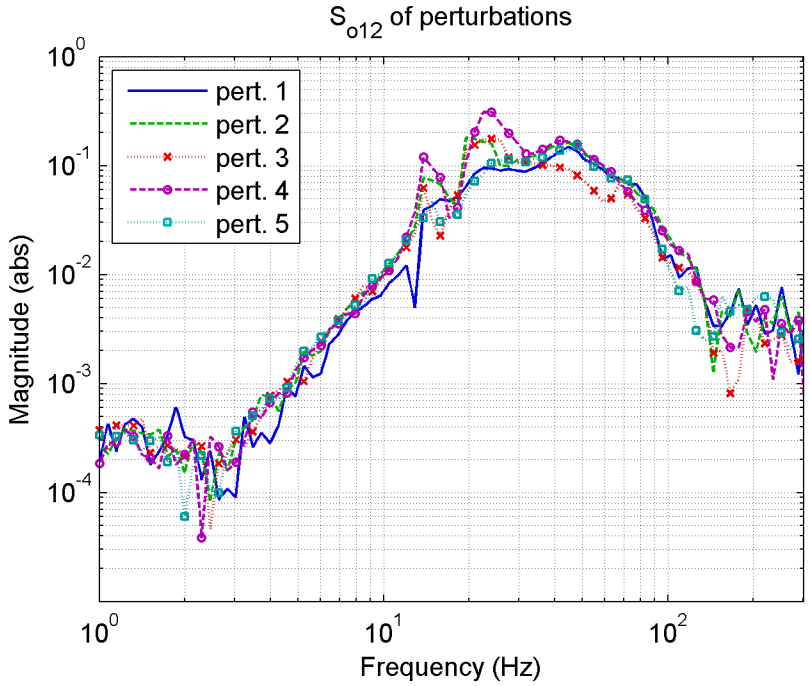

Figure 115: So_{12} of perturbations with the LQG/LTR controller

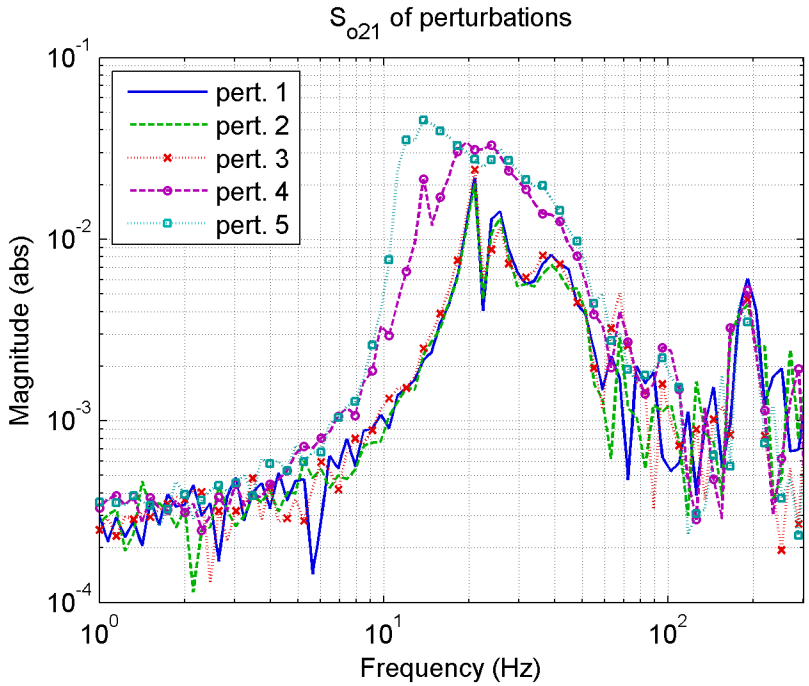

Figure 116: So_{21} of perturbations with the LQG/LTR controller

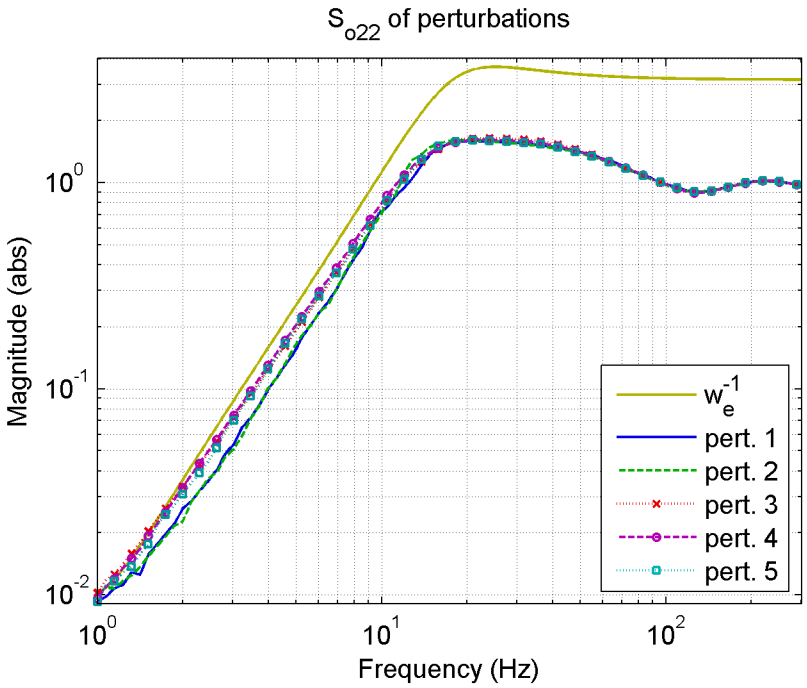

Figure 117: So_{22} of perturbations with the LQG/LTR controller

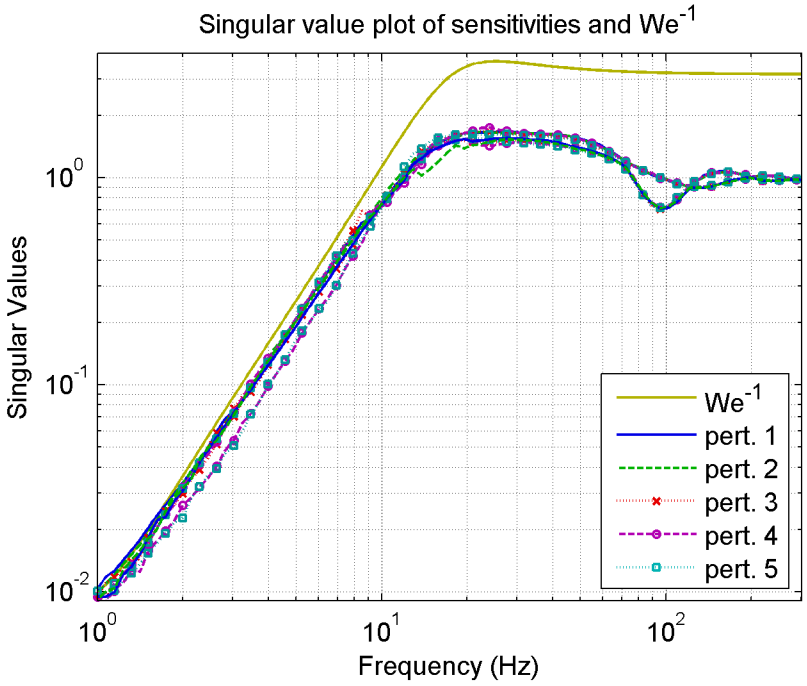

Figure 118: Singular value plot of sensitivities and W_e^{-1} with the LQG/LTR controller

8.2.2. $\mathcal{H}_\infty$ Design

The experimental closed loop transfer functions So_{11}, So_{12}, So_{21} and So_{22} created with the $\mathcal{H}_\infty$ controller are depicted in Figs. 119-122. After that, the singular values of S_o can be found in Fig. 123.

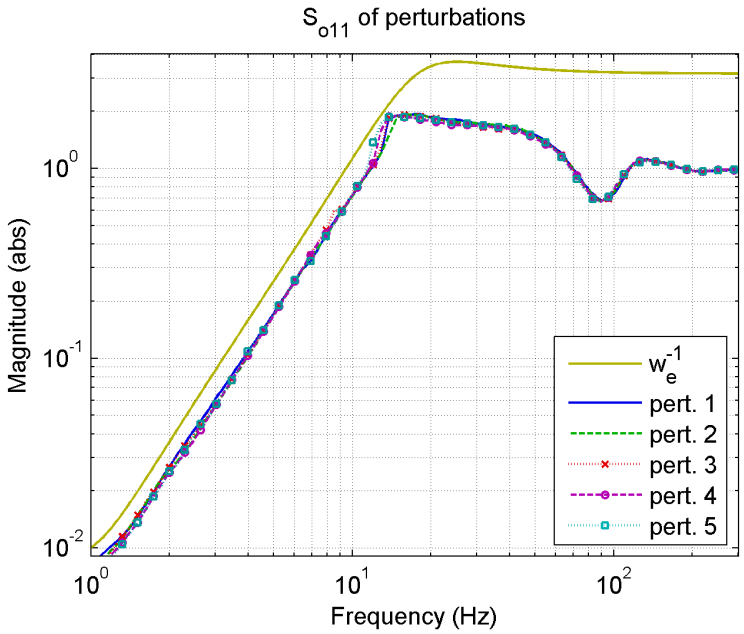

Figure 119: So_{11} of perturbations with the $\mathcal{H}_\infty$ controller

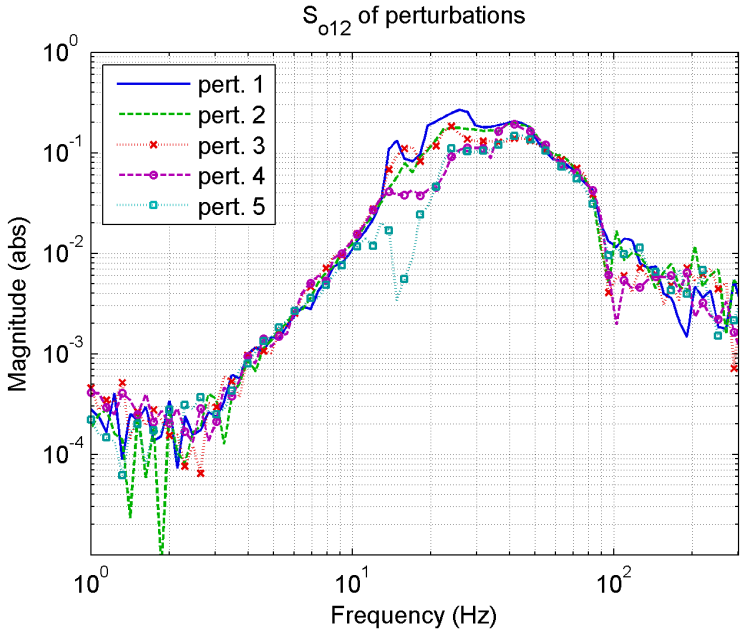

Figure 120: So_{12} of perturbations with the $\mathcal{H}_\infty$ controller

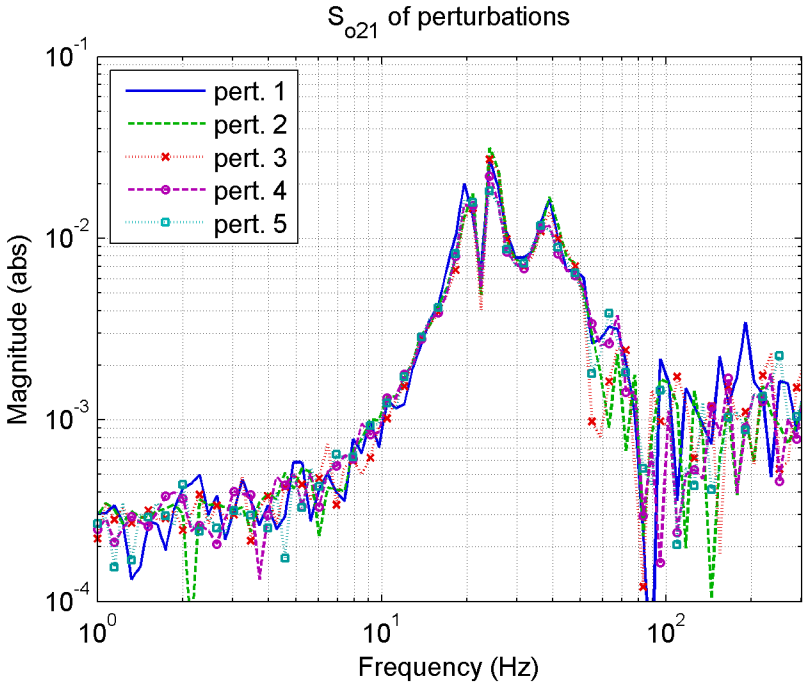

Figure 121: So_{21} of perturbations with the $\mathcal{H}_\infty$ controller

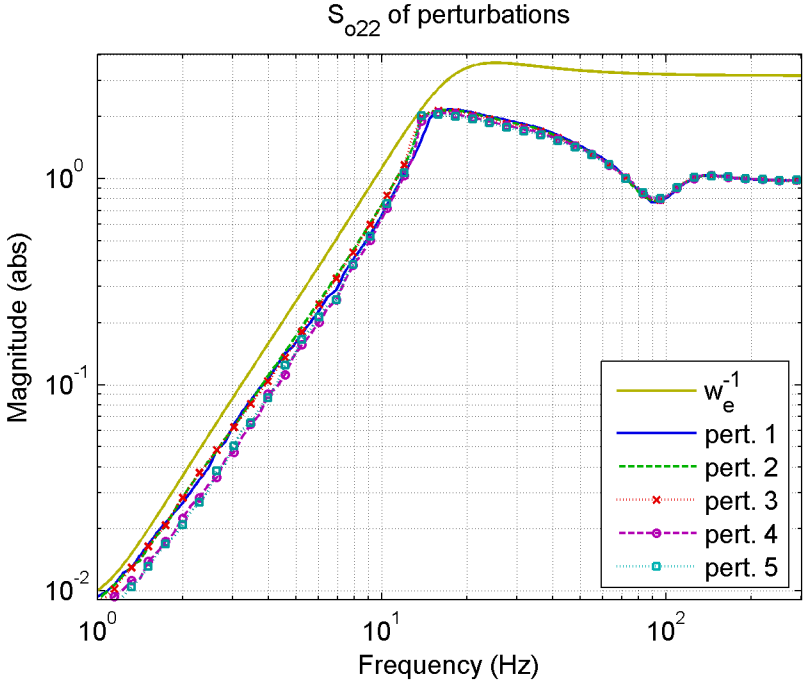

Figure 122: So_{22} of perturbations with the $\mathcal{H}_\infty$ controller

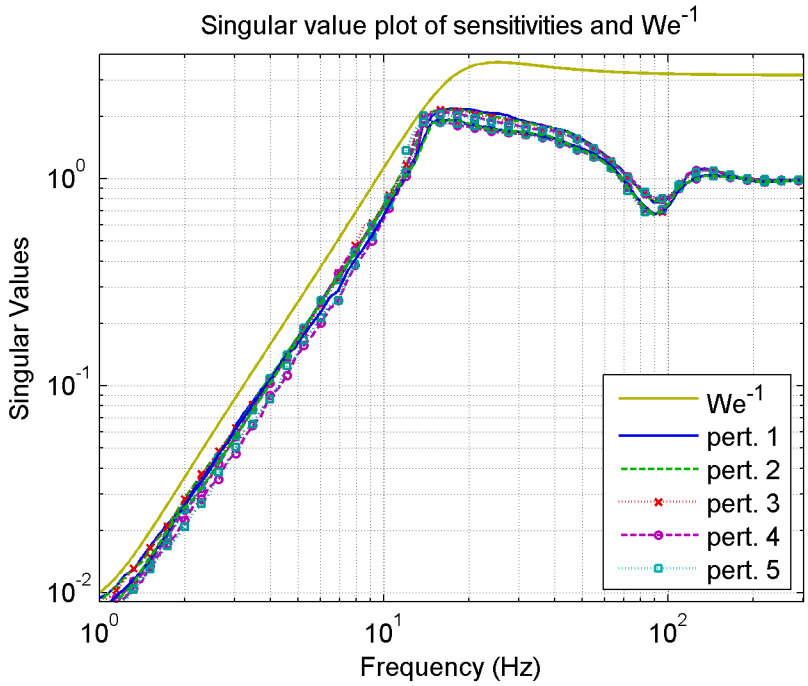

Figure 123: Singular value plot of sensitivities and W_e^{-1} with the $\mathcal{H}_\infty$ controller

8.2.3. μ-synthesis Design

The responses of transfer functions So_{11}, So_{12}, So_{21} and So_{22} given in Eq. (8.15) are obtained for the closed loop system constructed with the μ controller, and corresponding gains are given in Figs. 124-127. Then for two-input two-output system, singular values of S_o are plotted in Fig. 128.

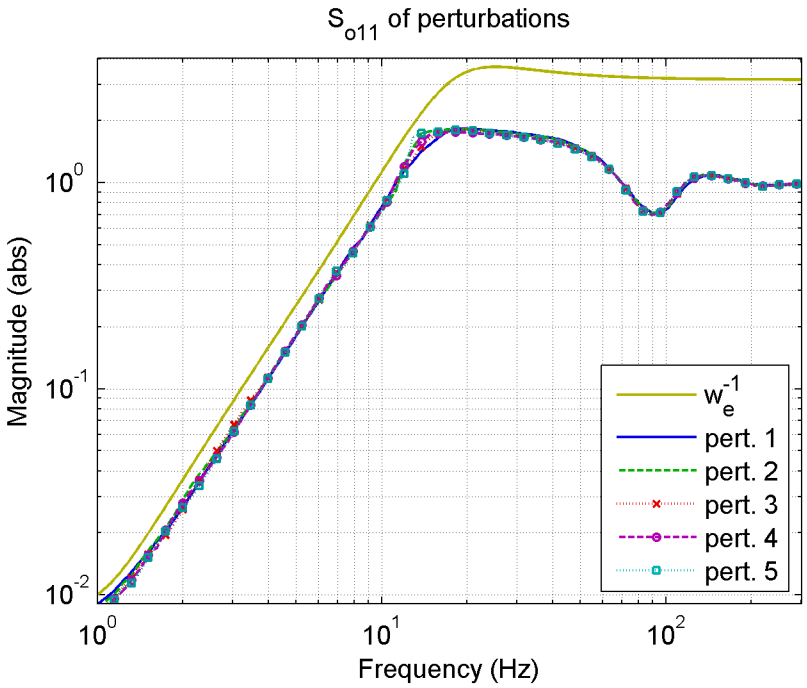

Figure 124: So_{11} of perturbations with the μ controller

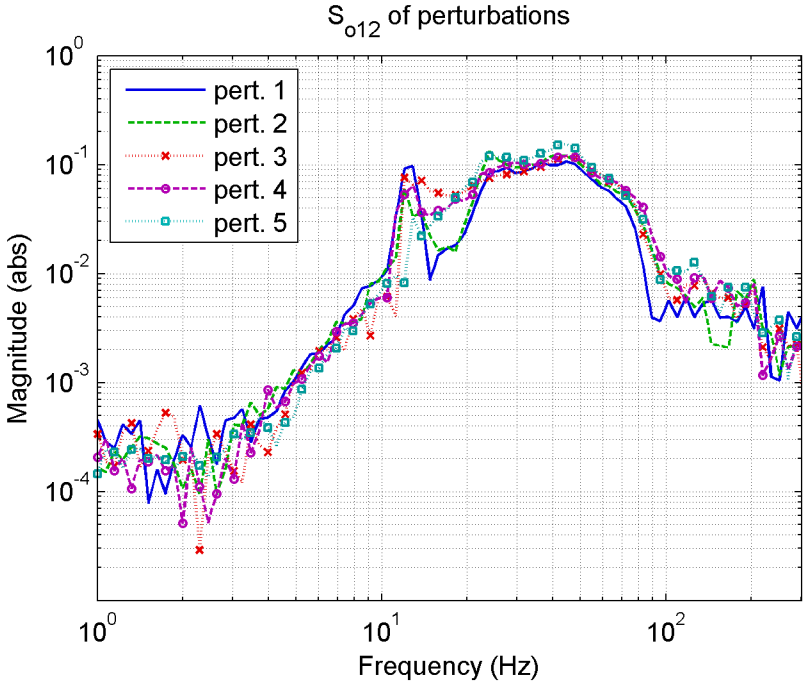

Figure 125: So_{12} of perturbations with the μ controller

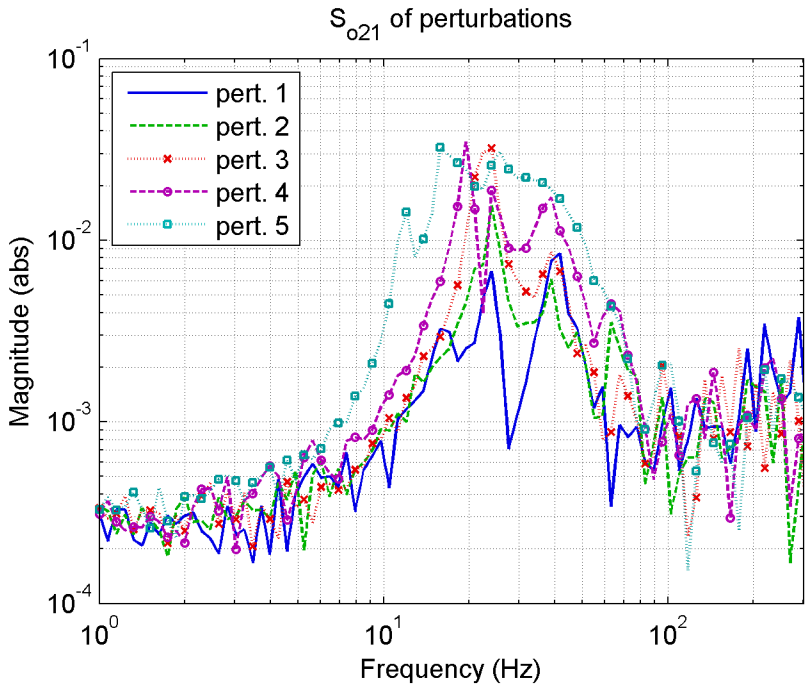

Figure 126: S_{o21} of perturbations with the μ controller

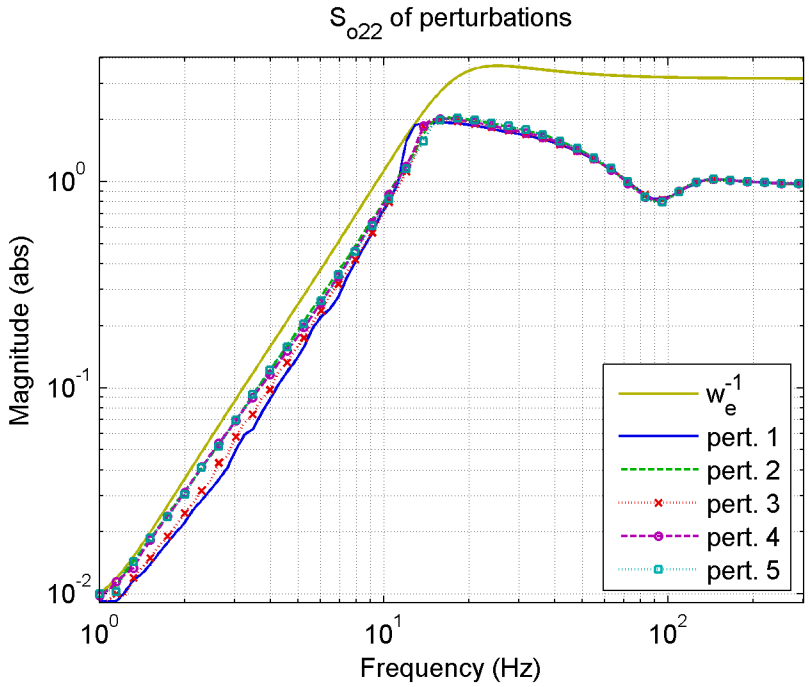

Figure 127: S_{o22} of perturbations with the μ controller

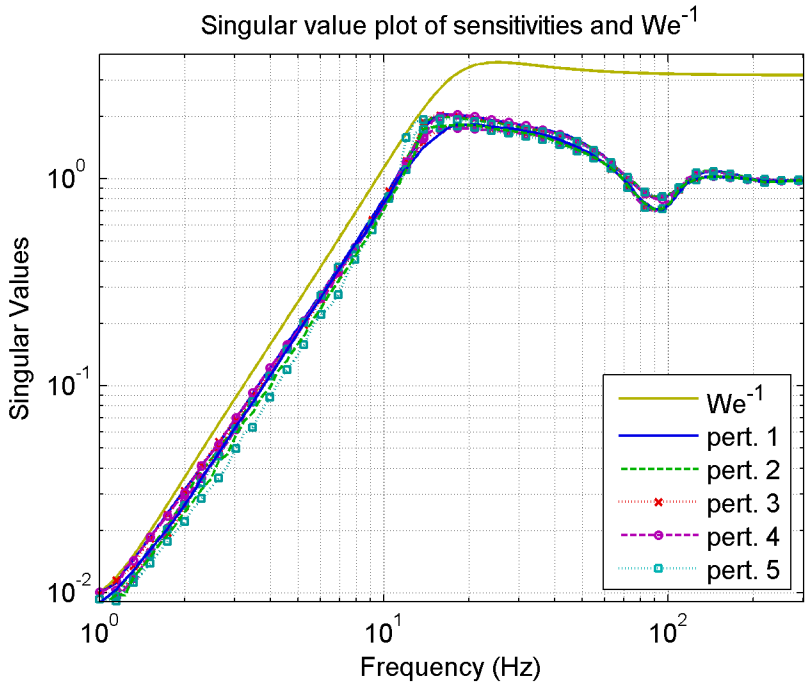

Figure 128: Singular value plot of sensitivities and W_e^{-1} with the μ controller

8.2.4. Performance Analysis

In this section, the performances of different perturbations are discussed. Again the analysis is done for two performance criteria. Firstly, the performance in Eq. (8.16) is considered. Next, the analysis is redone for requirement in Eq. (8.17) for three controllers.

$$\|W_e S_o\|_\infty < 1 \tag{8.16}$$

$$\left\| \begin{bmatrix} W_e S_o \\ W_u K S_o \end{bmatrix} \right\|_\infty < 1 \tag{8.17}$$

Define the performance analysis for the criterion in Eq. (8.16) as case 1, and analysis for requirement in Eq. (8.17) as case 2. Then the experimental results for the two cases are given for different controllers below.

8.2.4.1. LQG/LTR Design

The experimental performances of the LQG/LTR compensated closed loop for different disturbance levels are plotted in Figs. 129 and 130 for two cases.

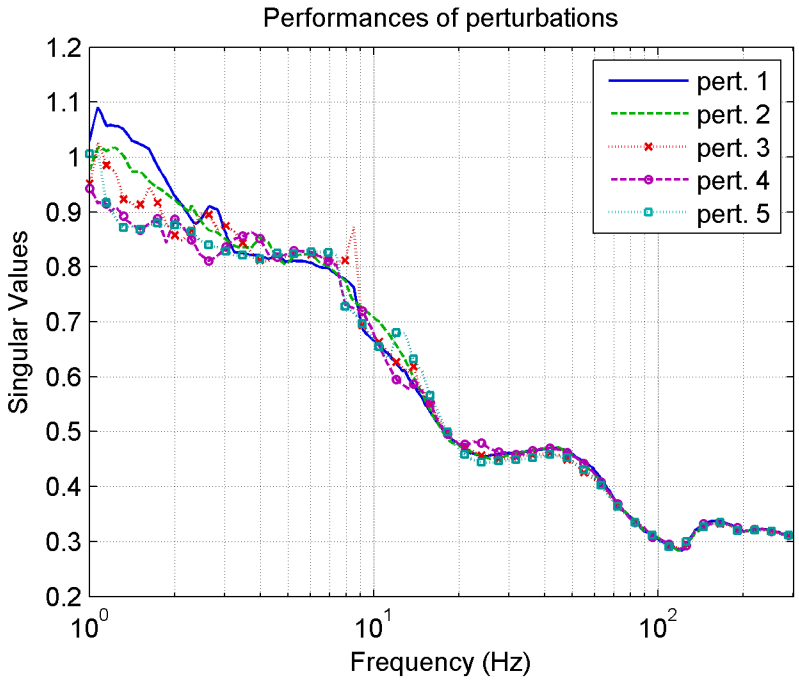

Figure 129: Performances of perturbations with the LQG/LTR controller (case 1)

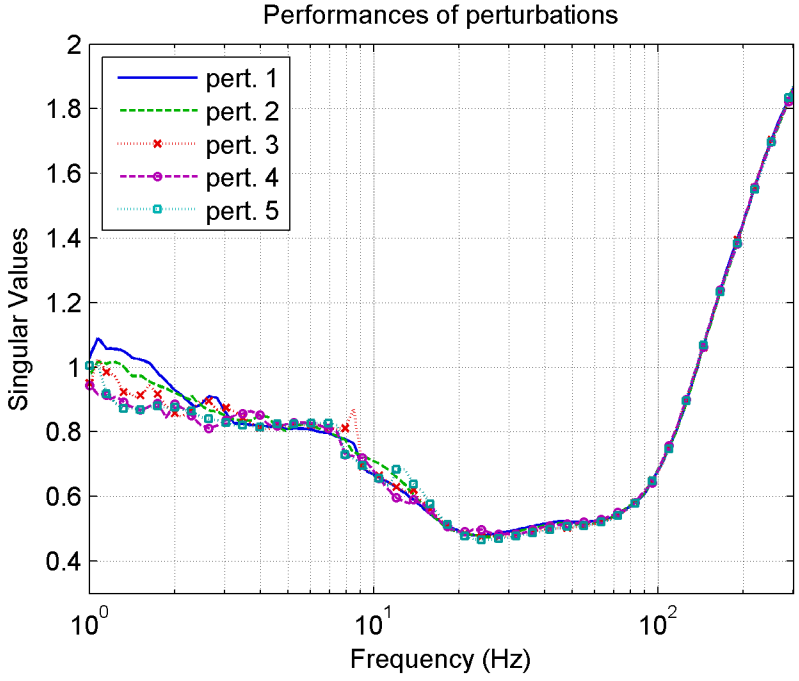

Figure 130: Performances of perturbations with the LQG/LTR controller (case 2)

8.2.4.2. $\mathcal{H}_\infty$ Design

The performances of closed loop with the $\mathcal{H}_\infty$ controller are given in Figs. 131 and 132.

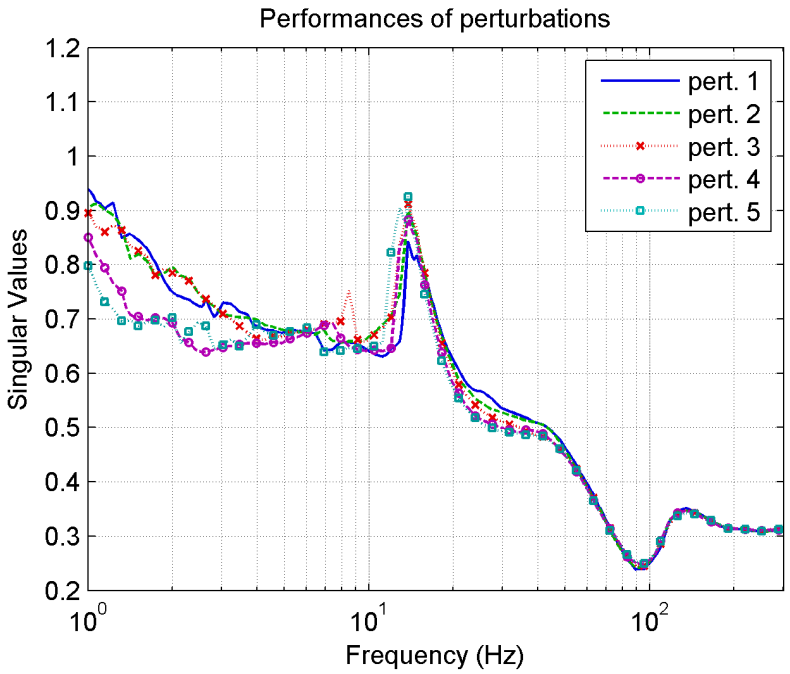

Figure 131: Performances of perturbations with the $\mathcal{H}_\infty$ controller (case 1)

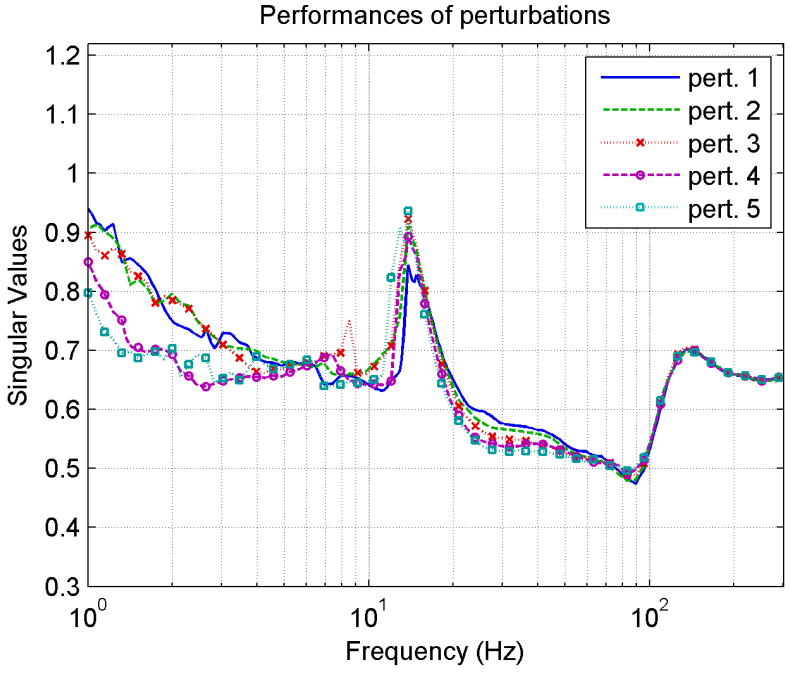

Figure 132: Performances of perturbations with the $\mathcal{H}_\infty$ controller (case 2)

8.2.4.3. μ-synthesis Design

Finally, experimental performances with the μ controller are shown in Figs. 133 and 134.

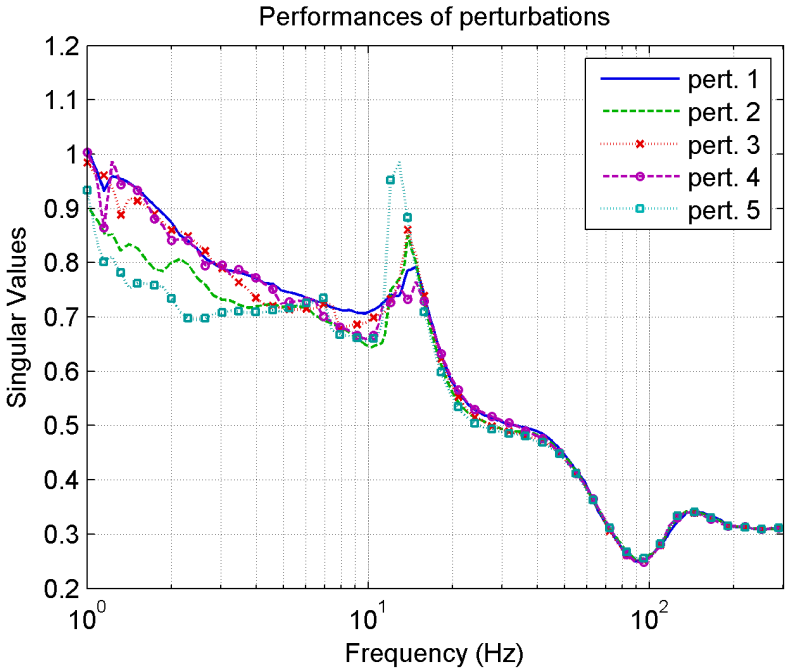

Figure 133: Performances of perturbations with the μ controller (case 1)

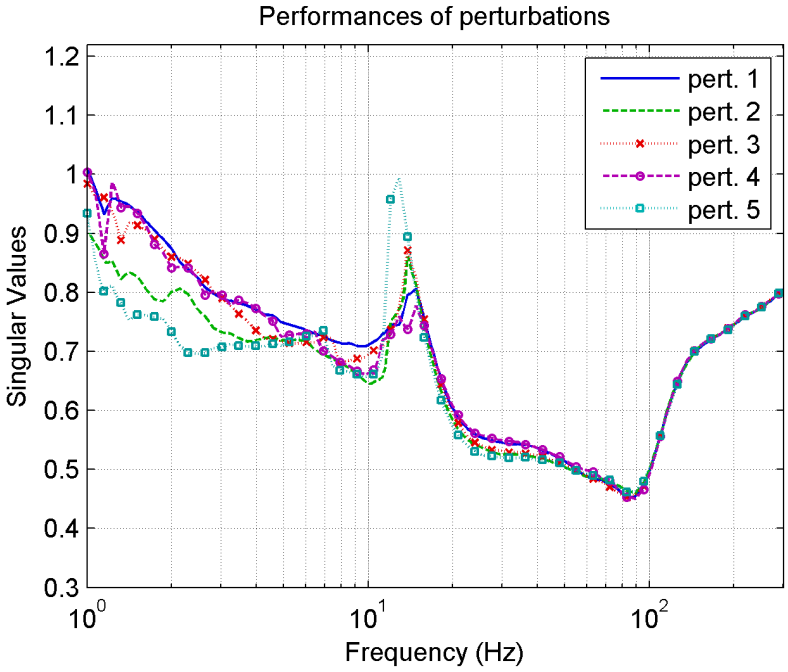

Figure 134: Performances of perturbations with the μ controller (case 2)

8.2.5. Summary of the Experimental Results

Comparison of the theoretical nominal performances was made and the results were shown in Fig. 101 for case 1 previously. Similar observations are made for the experimental case as given in Fig. 135 below. At low frequencies while the $\mathcal{H}_\infty$ controller shows the best performance, the LQG/LTR shows the worst. On the other hand, the worst performance is created by the $\mathcal{H}_\infty$ controller in mid frequencies for case 1. At high frequencies they show similar properties.

The theoretical nominal performances corresponding to case 2 were given in Fig. 103 in previous chapter. The experimental results shown in Fig. 136 possess similar characteristics. At low frequencies, the best and the worst performances are created by the $\mathcal{H}_\infty$ and the LQG/LTR controllers respectively as in case 1. However, due to high gain of the LQG/LTR controller at high frequencies, its performance degrades. Also, at mid frequencies the μ controller is better than the $\mathcal{H}_\infty$ controller. Moreover, at high frequencies the $\mathcal{H}_\infty$ controller is the best one which is expected from the theoretical results.

Note that as frequency increases beyond the loop bandwidth, the disturbances are amplified at control signal. So, usually at this region the current references are high. When the input excitation signal is high, the nonlinear effects remain small which makes the perturbed plants approach to nominal model built in Chapter 5. Therefore, at high frequencies some perturbations could not be seen. Moreover, recall that the swept sine tests in Chapter 6 begin from 3 Hz for azimuth, and 5 Hz for elevation since there are mechanical limits in the structure. For that reason, the uncertainty modeling is valid above these frequencies. On the other hand, the experimental performances are derived above 1 Hz. That is, the results show that around 1 Hz slightly larger model error is available than the error at 3 Hz and 5 Hz for corresponding axes where the data begin. Moreover, high excitation signals lead to performance degradation around the small resonant peak of azimuth around 15 Hz. In other words, the model error at this region is slightly larger than the modeled one in Chapter 6. By looking at the overall picture, it can be said that the modeling, identification and control show successful properties and they are similar to theoretical results.

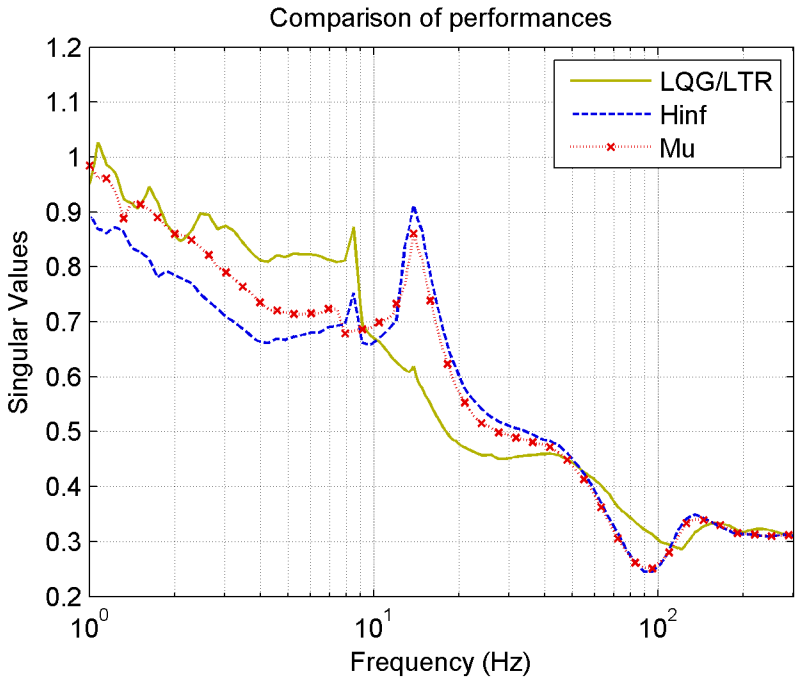

Figure 135: Comparison of performances (case 1)

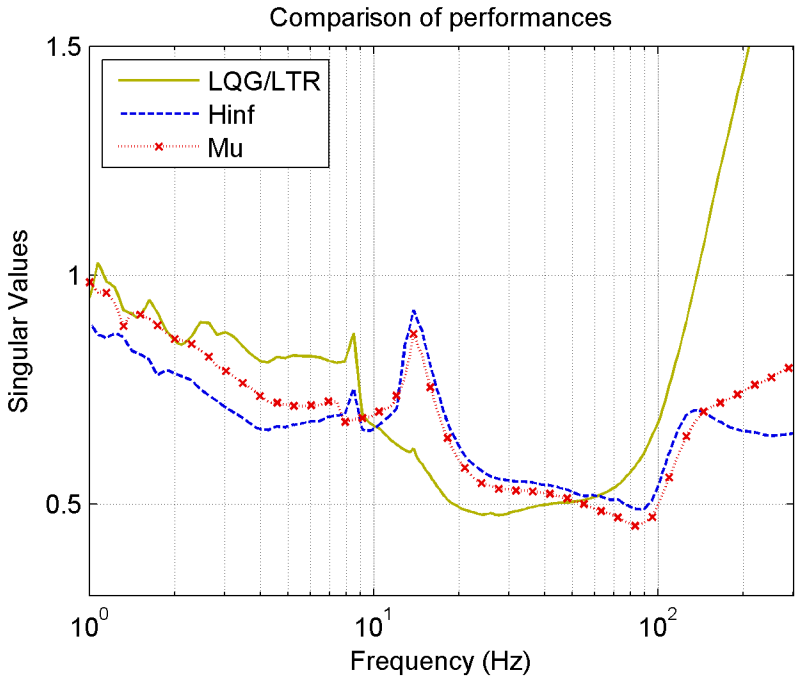

Figure 136: Comparison of performances (case 2)

The chapter is concluded with the transient responses of disturbance rejection for different controllers and for two channels separately. The disturbance signal is a square signal at 4 Hz, and the results are given in Figs. 137 and 138. They show that the three controllers possess good disturbance rejection responses.

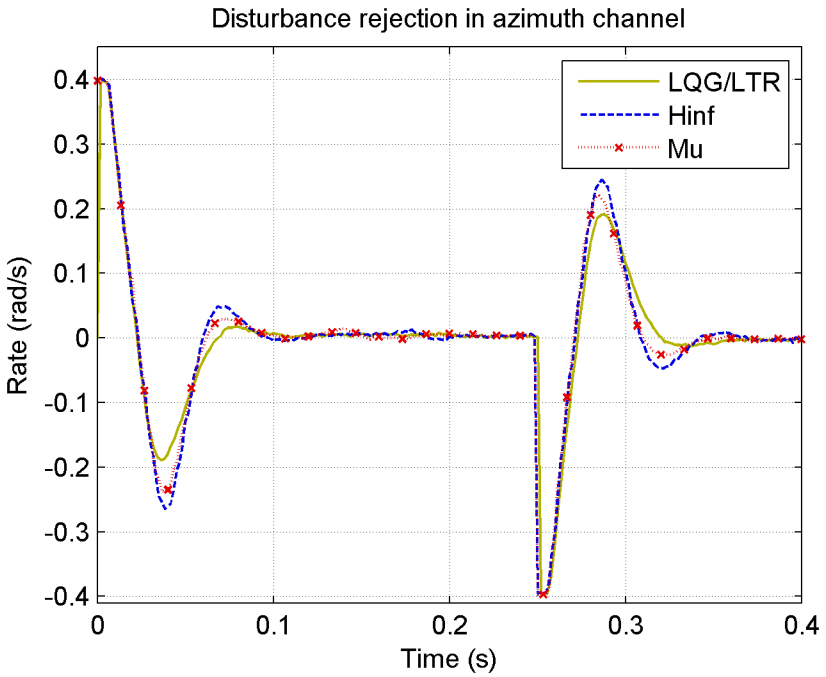

Figure 137: Disturbance rejection in azimuth channel

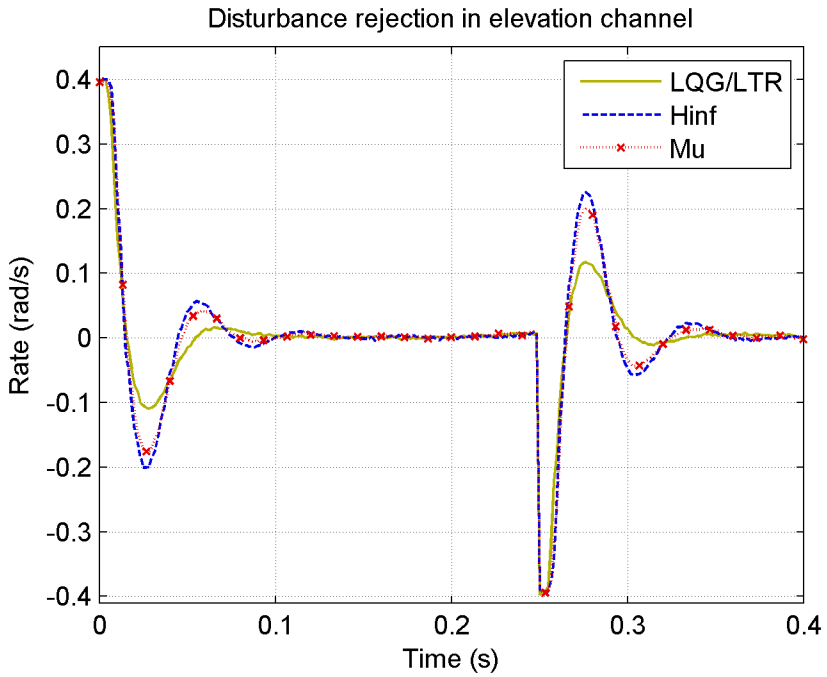

Figure 138: Disturbance rejection in elevation channel

8.3. Summary

In this chapter, the procedures followed for controller implementations are explained. Then the experimental results are depicted. Comparison of the controller is made using the experimental data and the theoretical expectations.

CHAPTER 9

CONCLUSION

9.1. Summary

In this thesis, the LQG/LTR,$\mathcal{H}_\infty$ and μ control methodologies are applied to design a robust line of sight stabilizing controller. First, the robust control theory is briefly discussed. The importance of $\mathcal{H}_2$ and $\mathcal{H}_\infty$ norms for controller design is expressed. The generalized plant construction, performance weight selection and uncertainty modeling are summarized. Nominal stability, nominal performance, robust stability and robust performance are investigated. Then motivations behind μ-analysis and its approximate solution *D-K* iteration are examined.

After introducing the experimental setup, a two-axis gimbal system is modeled and its parameters are identified using CD-EKF. Then the two-input two-output MIMO nominal model is constructed. After that, using swept sine tests the uncertainties are found. Next, the performance requirement in the system is considered. By considering the constraints on the output jitter, control input and the experimental disturbance profile taken from the platform, the required performance weights are derived. By augmenting the nominal model with these performance and uncertainty weights the generalized plant and LFT structure are obtained.

Firstly, the LQG/LTR controller is designed for an augmented plant with weight which is related with the disturbance power spectrum. After that, using the LFT structure built in *S*/*KS*/*T* mixed sensitivity framework the $\mathcal{H}_\infty$ and μ controllers are designed. Next, the theoretical results are shared for closed loops constructed with these three controllers. Then the comparison is made by considering the performance and stability of the corresponding loops. After that, the implementation issues of the controllers are expressed. The Balanced Truncation and discretization methods are introduced. Next, experimental responses of the closed loop transfer functions are illustrated. Using these experimental responses, the closed loop transfer matrix is constructed for MIMO system.

Then the experimental MIMO closed loop properties are investigated. Finally, the experimental performances and their comparisons are expressed.

9.2. Results and Discussions

In this section, the results obtained throughout the thesis are reviewed. Then important points about the control methods are shared.

In low frequency region, the $\mathcal{H}_\infty$ controller has the best performance due to the highest gain. On the other hand, the LQG/LTR shows the worst performance.

In mid frequency region, $\mathcal{H}_\infty$ controller has the worst performance. Around crossover region the μ controller has better performance than $\mathcal{H}_\infty$ controller. At these frequencies, LQG/LTR shows the best performance.

In high frequency region, LQG/LTR possesses the worst performance which results from the high gains there. At this region, $\mathcal{H}_\infty$ controller is the best one owing to the highest roll off rate.

Note that, the control methods discussed in this thesis all try to minimize some cost functions. LQG/LTR controller tries to minimize the total nominal performance over all frequencies. On the other hand, $\mathcal{H}_\infty$ controller tries to minimize the worst case nominal performance over all frequencies. Finally, μ controller attempts to minimize the worst case robust performance. However, there are trade-offs in feedback systems. In other words, it is not possible to obtain good performance in all these aspects at the same time. For example, small robust performance peak comes with reduced nominal performance. In a similar way, better nominal performance may lead to poorer robust stability, and robust performance. In this aspect, following conclusions can be made:

When the performance at low frequencies is important one can use the $\mathcal{H}_\infty$ controller.

On the other hand, the performance over all frequencies is essential the μ controller should be chosen.

If the worst case perturbation is unlikely to occur, one can prefer $\mathcal{H}_\infty$ controller over μ controller. However, if the converse is true, μ controller should be chosen.

When performance is only measured by weighted output sensitivity, the LQG/LTR controller can be used; however, it has the poorest stability at high frequencies. So, LQG/LTR controller must be the third choice.

9.3. Publications

The controller design procedures and results discussed in this thesis are reported, and the following paper is submitted for publication.

Mehmet Baskın and Kemal Leblebicioğlu, "Multivariable robust line of sight stabilizing controllers design in LQG/LTR, $\mathcal{H}_\infty$ and μ-synthesis frameworks", submitted for publication, 2015.

To investigate the differences of classical control and robust control, the theories are applied to SISO dc-dc converter control problem, and the following paper is presented in TOK, in September 2015, Denizli.

Mehmet Baskın and Kemal Leblebicioğlu, "Fotovoltaik uygulamalarda kullanılan yükseltici tip DA-DA çeviricinin μ sentezi ile gürbüz voltaj kontrolü", in *Otomatik Kontrol Türk Milli Komitesi Ulusal Toplantısı* (*TOK*), pp. 262-267, 2015.

9.4. Future Work

The design methodologies introduced in this thesis can be applied to any MIMO system by changing the corresponding performance weights according to problem and system. It is discussed that the LTR procedure for non-minimum phase plants cannot be as successful as for minimum phase counterparts. This phenomenon is actually observed in this thesis while discussing the LQG/LTR controller design. However, the problem is solved by a heuristic method which depends on augmenting the plant with modified weight. In this aspect, the achievable LTR for non-minimum phase plant and corresponding weight selection can be investigated [20, 46]. Moreover, the $\mathcal{H}_\infty$ loop-shaping design procedure introduced in [47] and its differences from mixed sensitivity design can be examined [12, 48, 49]. In addition, if there is a restriction on pole or zero location of the controller the bilinear pole shifting transform discussed in [50] can be used. Also, $\mathcal{H}_2/\mathcal{H}_\infty$ mixed controller can be designed [51, 52]. Finally, by using friction compensator whether the uncertainty reduction is possible can be investigated [28, 53].

REFERENCES

[1] P. Kennedy and R. Kennedy, *Line of sight stabilization primer*. Peter Kennedy, 2008.

[2] J. M. Hilkert, "Precision stabilized pointing & tracking systems", Notes for a Short Course of the SPIE, Ankara, Turkey, 2012.

[3] W. J. Bigley and V. J. Rizzo, "Wideband linear quadratic control of a gyro-stabilized electro-optical sight system", *IEEE Control Syst. Mag.*, vol. 7, no. 4, pp. 20-24, 1987.

[4] W. J. Bigley and S. P. Tsao, "Optimal motion stabilization control of an electro-optical sight system", *SPIE Proceedings Acquisition, Tracking, and Pointing III*, vol. 1111, 1989.

[5] R. Marathe, "Design of the line of sight stabilization using LQG/LTR methodology for mobile land vehicles", M.S. thesis, Indian Institute of Technology, 1997.

[6] R. Xiao, T. Li, P. Zhang, X. Jia, Y. Qin and C. Xian, "The LQG/LTR controller design for miniaturized infrared stabilizing platform", *International Symposium on Photoelectronic Detection and Imaging 2011: Advances in Infrared Imaging and Applications*, 2011.

[7] K. Moorty, R. Marathe and V. Sule, "H∞ control law for line-of-sight stabilization for mobile land vehicles", *Optical Engineering*, vol. 41, no. 11, pp. 2935-2944, 2002.

[8] Z. Liu, Q. Bao, Y. Xia and X. Liu, "H∞ mix sensitivity controller design based on GIMC for electro-optical stabilization and tracking system", *International Symposium on Photoelectronic Detection and Imaging 2013: Laser Communication Technologies and Systems*, 2013.

[9] B. Wenliang, H. Xianlin and B. Xiaojun, “Control system design of multi-gimbal electro-optical platform by the technique of μ-synthesis”, in *Chinese Control Conference*, 2010, pp. 3447-3452.

[10] S. Kim, S. Kim and Y. Kwak, “Robust control for a two-axis gimbaled sensor system with multivariable feedback systems”, *IET Control Theory & Applications*, vol. 4, no. 4, pp. 539-551, 2010.

[11] J. Maciejowski, *Multivariable feedback design*. Wokingham, England: Addison-Wesley, 1989.

[12] K. Zhou and J. Doyle, *Essentials of robust control*. Upper Saddle River, N.J.: Prentice Hall, 1998.

[13] S. Skogestad and I. Postlethwaite, *Multivariable feedback control*. Chichester: Wiley, 1996.

[14] O. Bosgra, H. Kwakernaak and G. Meinsma, “Design methods for control systems”, Notes for a Course of the Dutch Institute of Systems and Control, 2007.

[15] G. Balas, J. Doyle, K. Glover, A. Packard and R. Smith, *μ-analysis and synthesis toolbox*, MUSYN Inc. and The MathWorks, Inc, 1994.

[16] R. Smith and P. Goulart, “Advanced topics in control”, Notes for a Course of the ETH Zurich, 2014.

[17] ESSB-HB-E-003 Working Group, *ESA pointing error engineering handbook*. European Space Agency, 2011.

[18] H. Bode, “Relations between attenuation and phase in feedback amplifier design”, *Bell System Technical Journal*, vol. 19, no. 3, pp. 421-454, 1940.

[19] A. Packard and J. Doyle, “The complex structured singular value”, *Automatica*, vol. 29, no. 1, pp. 71-109, 1993.

[20] G. Stein and M. Athans, “The LQG/LTR procedure for multivariable feedback control design”, *IEEE Transactions on Automatic Control*, vol. 32, no. 2, pp. 105-114, 1987.

[21] R. Kalman and R. Bucy, “New results in linear filtering and prediction theory”, *Journal of Basic Engineering*, vol. 83, no. 1, p. 95, 1961.

[22] B. Anderson and J. Moore, *Optimal control: linear quadratic methods*. Englewood Cliffs, N.J.: Prentice Hall, 1990.

[23] M. Safonov and M. Athans, “Gain and phase margin for multiloop LQG regulators”, *IEEE Transactions on Automatic Control*, vol. 22, no. 2, pp. 173-179, 1977.

[24] J. Doyle, “Guaranteed margins for LQG regulators”, *IEEE Transactions on Automatic Control*, vol. 23, no. 4, pp. 756-757, 1978.

[25] J. Doyle and G. Stein, “Multivariable feedback design: Concepts for a classical/modern synthesis”, *IEEE Transactions on Automatic Control*, vol. 26, no. 1, pp. 4-16, 1981.

[26] J. Doyle, K. Glover, P. Khargonekar and B. Francis, “State-space solutions to standard H 2 and H∞ control problems”, *IEEE Transactions on Automatic Control*, vol. 34, no. 8, pp. 831-847, 1989.

[27] B. Ekstrand, “Equations of motion for a two-axes gimbal system”, *IEEE Trans. Aerosp. Electron. Syst.*, vol. 37, no. 3, pp. 1083-1091, 2001.

[28] H. Olsson, K. Åström, C. Canudas de Wit, M. Gäfvert and P. Lischinsky, “Friction models and friction compensation”, *European Journal of Control*, vol. 4, no. 3, pp. 176-195, 1998.

[29] M. Masten, “Inertially stabilized platforms for optical imaging systems”, *IEEE Control Syst. Mag.*, vol. 28, no. 1, pp. 47-64, 2008.

[30] G. Bontempi and M. Birattari, “From linearization to lazy learning: A survey of divide-and-conquer techniques for nonlinear control”, *International Journal of Computational Cognition*, vol. 3, no. 1, pp. 56-73, 2005.

[31] R. Murray-Smith and T. Johansen, *Multiple model approaches to modeling and control*. London: Taylor & Francis, 1997.

[32] S. Fekri, M. Athans and A. Pascoal, "RMMAC: a novel robust adaptive control scheme. Part I. Architecture", *2004 43rd IEEE Conference on Decision and Control (CDC) (IEEE Cat. No.04CH37601)*, 2004.

[33] J. Shamma and M. Athans, "Analysis of gain scheduled control for nonlinear plants", *IEEE Transactions on Automatic Control*, vol. 35, no. 8, pp. 898-907, 1990.

[34] Sensonor, "Inertial Measurement Unit", STIM300 datasheet, April 2013 [TS1524 rev.8].

[35] G. Chowdhary and R. Jategaonkar, "Aerodynamic parameter estimation from flight data applying extended and unscented Kalman filter", *Aerospace Science and Technology*, vol. 14, no. 2, pp. 106-117, 2010.

[36] F. Lewis, L. Xie, D. Popa and F. Lewis, *Optimal and robust estimation*. Boca Raton: CRC Press, 2008.

[37] J. Crassidis and J. Junkins, *Optimal estimation of dynamic systems*. Boca Raton: Chapman & Hall/CRC, 2004.

[38] M. Verhaegen and V. Verdult, *Filtering and system identification*. Cambridge: Cambridge University Press, 2007.

[39] G. Özdoğan and K. Leblebicioğlu, "Frequency response function measurement and parametric SISO system modelling of a gyro-stabilized infrared electro optic gimbal system", *Transactions of the Institute of Measurement and Control*, 2015.

[40] D. Gu, P. Petkov and M. Konstantinov, *Robust control design with MATLAB*. London: Springer, 2005.

[41] B. Moore, "Principal component analysis in linear systems: Controllability, observability, and model reduction", *IEEE Transactions on Automatic Control*, vol. 26, no. 1, pp. 17-32, 1981.

[42] M. Safonov and R. Chiang, “A Schur method for balanced-truncation model reduction”, *IEEE Transactions on Automatic Control*, vol. 34, no. 7, pp. 729-733, 1989.

[43] A. Laub, M. Heath, C. Paige and R. Ward, “Computation of system balancing transformations and other applications of simultaneous diagonalization algorithms”, *IEEE Transactions on Automatic Control*, vol. 32, no. 2, pp. 115-122, 1987.

[44] D. Enns, “Model reduction with balanced realizations: An error bound and a frequency weighted generalization”, in *The 23rd IEEE Conference on Decision and Control*, 1984.

[45] T. Chen and B. Francis, *Optimal sampled-data control systems*. London: Springer, 1995.

[46] Z. Zhang and J. Freudenberg, “Loop transfer recovery for nonminimum phase plants”, *IEEE Transactions on Automatic Control*, vol. 35, no. 5, pp. 547-553, 1990.

[47] D. McFarlane and K. Glover, “A loop-shaping design procedure using H∞ synthesis”, *IEEE Transactions on Automatic Control*, vol. 37, no. 6, pp. 759-769, 1992.

[48] R. Hyde and K. Glover, “The application of scheduled H∞ controllers to a VSTOL aircraft”, *IEEE Transactions on Automatic Control*, vol. 38, no. 7, pp. 1021-1039, 1993.

[49] C. Qullette, “H2 and H∞ Control of a Twin Lift Helicopter System”, M.S. thesis, MIT, 1996.

[50] Chiang, R.Y and M.G Safonov, “Design of H∞ controller for a lightly damped system using a bilinear pole shifting transform”, Proc.of the 1991 ACC, Boston, MA, 26-28 June, 1991 pp 1927- 1928.

[51] J. Doyle, K. Zhou, K. Glover and B. Bodenheimer, “Mixed H2 and H∞ performance objectives. I. Robust performance analysis”, *IEEE Transactions on Automatic Control*, vol. 39, no. 8, pp. 1575-1587, 1994.

[52] T. Ölçer, “H2/H∞ mixed robust controller synthesis for a fin actuation system”, M.S. thesis, METU, 2013.

[53] C. Canudas, K. Astrom and K. Braun, “Adaptive friction compensation in dc-motor drives”, *IEEE J. Robot. Automat.*, vol. 3, no. 6, pp. 681-685, 1987.

APPENDIX A

DISCRETIZATION OF CONTROLLER WITH BILINEAR TRANSFORM

Assume the continuous-time controller has a state space model in Eq. (A.1). Then it suggests Eq. (A.2).

$$\dot{x} = Ax + Bu,\ y = Cx + Du \tag{A.1}$$

$$x_{k+1} - x_k = \int_{t_k}^{t_{k+1}} \dot{x}\, dt = A\int_{t_k}^{t_{k+1}} x\, dt + B\int_{t_k}^{t_{k+1}} u\, dt \tag{A.2}$$

The integrals on the right-hand side are approximated by trapezoidal rules as given in Eq. (A.3).

$$\int_{t_k}^{t_{k+1}} x\, dt = \frac{T_s}{2}\left(x_{k+1} + x_k\right) \quad , \quad \int_{t_k}^{t_{k+1}} u\, dt = \frac{T_s}{2}\left(u_{k+1} + u_k\right) \tag{A.3}$$

Then

$$x_{k+1} - x_k = A\frac{T_s}{2}\left[x_{k+1} + x_k\right] + B\frac{T_s}{2}\left[u_{k+1} + u_k\right]$$

$$\Rightarrow \left[I - A\frac{T_s}{2}\right]x_{k+1} = \left[I + A\frac{T_s}{2}\right]x_k + B\frac{T_s}{2}\left[u_{k+1} + u_k\right]$$

$$\Rightarrow x_{k+1} = \underbrace{\left[I - A\frac{T_s}{2}\right]^{-1}\left[I + A\frac{T_s}{2}\right]}_{A_{bt}}x_k + \underbrace{\left[I - A\frac{T_s}{2}\right]^{-1}B\frac{T_s}{2}}_{B_{bt}}\left[u_{k+1} + u_k\right]$$

Now consider the Eq. (A.4).

$$\begin{aligned} z_{k+1} &= A_{bt}z_k + B_{bt}u_k \\ z_{k+2} &= A_{bt}z_{k+1} + B_{bt}u_{k+1} \end{aligned} \tag{A.4}$$

Since $x_k = z_k + z_{k+1}$ is satisfied, adding two equations in Eq. (A.4) gives desired x_k.

$$
\begin{aligned}
y_k = C\,x_k + D\,u_k &= C\left(z_k + z_{k+1}\right) + D\,u_k \\
&= C\,z_k + C\left(A_{bt} z_k + B_{bt} u_k\right) + D\,u_k \\
&= \underbrace{C\left(I + A_{bt}\right)}_{C_{bt}} z_k + \underbrace{\left(D + CB_{bt}\right)}_{D_{bt}} u_k
\end{aligned}
$$

Therefore, the discrete approximation of controller in Eq. (A.1) is given in Eq. (A.5) with the matrices defined as above.

$$
\begin{aligned}
z_{k+1} &= A_{bt} z_k + B_{bt} u_k \\
y_k &= C_{bt} z_k + D_{bt} u_k
\end{aligned}
\tag{A.5}
$$